UNIVERSIDAD NACIONAL AUTÓNOMA DE MÉXICO
PROGRAMA DE MAESTRÍA Y DOCTORADO EN INGENIERÍA
INGENIERÍA ELÉCTRICA - PROCESAMIENTO DIGITAL DE SEÑALES

Estimación de Flujo Óptico 3D en Imágenes Cardíacas por medio de la transformada de Hermite

TESIS
QUE PARA OPTAR POR EL GRADO DE:
DOCTOR EN INGENIERÍA

PRESENTA:
M. en I. Carlos Mira González

TUTORES PRINCIPALES
Dr. Boris Escalante Ramírez, Facultad de Ingeniería
Dr. Ernesto Moya Albor, Universidad Panamericana
COMITÉ TUTOR
Dra. María Elena Martínez Pérez, IIMAS
Dr. Pablo Roberto Pérez Alcázar, Facultad de Ingeniería

CIUDAD DE MÉXICO, SEPTIEMBRE 2020

JURADO ASIGNADO:

Presidente:	DR. PABLO ROBERTO PÉREZ ALCÁZAR
Secretario:	DR. ALFONSO GASTÉLUM STROZZI
$1^{er.}$ Vocal:	DR. BORIS ESCALANTE RAMÍREZ
$2^{do.}$ Vocal:	DRA. JIMENA OLVERES MONTIEL
$3^{er.}$ Vocal:	DR. ERNESTO MOYA ALBOR

Lugar donde se realizó la tesis: FACULTAD DE INGENIERÍA, UNAM.

TUTOR DE TESIS:

DR. BORIS ESCALANTE RAMÍREZ, FACULTAD DE INGENIERÍA

_____

FIRMA

Agradecimientos

En particular a mis asesores el Dr. Boris Escalante Ramírez de la UNAM y
al Dr. Ernesto Moya Albor de la Universidad Panamericana
por toda su experiencia, facilidades y apoyo,
a mi comité tutor por todas las observaciones y aportes realizadas,
al jurado asignado por la revisión y comentarios hechos,
y en general al Programa de Posgrado y a la UNAM,
por toda su formación e infraestructura ofrecida.
A mis seres queridos...
Es gracias a todos ustedes que es posible el presente trabajo.
Carlos Mira González.

Reconocimientos

También quisiera reconocer al CONACYT por mi beca doctoral otorgada, al Programa de Apoyo a Proyectos de Investigación e Innovación Tecnológica (UNAM-PAPIIT IN116917 e IA103119) de la UNAM, así como a la Secretaria de Educación, Ciencia, Tecnología e Innovación (SECTEI 202/2019) por el apoyo concedido a este trabajo.

Declaración de autenticidad

Por la presente declaro que, salvo cuando se haga referencia específica al trabajo de otras personas, el contenido de esta tesis es original y no se ha presentado total o parcialmente para su consideración para cualquier otro título o grado en esta o cualquier otra Universidad. Esta tesis es resultado de mi propio trabajo y no incluye nada que sea el resultado de algún trabajo realizado en colaboración, salvo que se indique específicamente en el texto.

M. en I. Carlos Mira González. Ciudad de México, Septiembre 2020

Resumen

A través de los años, el estudio del movimiento cardíaco se ha llevado a cabo principalmente en dos dimensiones, sin embargo, es importante considerar que los cambios de forma debidos al movimiento del corazón ocurren en un espacio tridimensional. Adicionalmente a esto, las enfermedades cardíacas son las principales causas de muerte en el Mundo Occidental. Es entonces importante implementar algoritmos que permitan ayudar a los especialistas a analizar el movimiento del corazón. Proponemos una nueva estrategia para estimar el movimiento cardíaco a través de una técnica diferencial de flujo óptico tridimensional que utiliza la transformada rotada de Hermite (SHT: Steered Hermite Transform). La SHT es una herramienta que permite la descomposición de imágenes con base en un modelo de patrones visuales usados por el sistema de visión humana (HSV: Human System Visión) para procesar la información. El análisis $3D + t$ nos permitiría describir mejor los movimientos del corazón, por ejemplo, el movimiento de torsión que ocurre en cada ciclo cardíaco y esto también nos ayudaría a identificar anormalidades en las paredes del corazón. Nuestra propuesta fue primero probada en $2D + t$, con flujos *ground truth*, posteriormente en $3D + t$ con tres *phantoms* diseñados para ello, así como en secuencias de ciclos cardíacos completos en imágenes CT y por último, en la correspondiente segmentación del ventrículo izquierdo. Evaluamos nuestro método usando un esquema de reconstrucción, para esto, el flujo óptico 3D resultante fue aplicado al volumen en el tiempo t para obtener el volumen estimado al tiempo $t + 1$. Realizamos una optimización de los parámetros involucrados y comparamos nuestra propuesta de flujo óptico 3D con el algoritmo mejorado de Horn y Schunck 3D multirresolución y diferentes niveles de ruido.

Abstract

Over the years, the study of cardiac movement has been carried out mainly in two dimensions, however, it is important to consider that the deformations due to the movement of the heart occur into three-dimensional space. Added to this, heart diseases are the most important causes of death in the Western world. Therefore, is important to implement algorithms to aid the specialist in analyzing the heart motion. We propose a new strategy to estimate the cardiac motion through a 3D optical flow differential technique that uses the steered Hermite transform (SHT). SHT is a tool that performs a decomposition of the images in a base that model the visual patterns used by the human vision system (HVS) for processing the information. The $3D + t$ analysis allows us to describe most of the motions of the heart, for example, the twisting motion that takes place on every beat cycle and to identify abnormalities of the heart walls. Our proposal was tested on three phantoms designed specifically for it and on several sequences of whole cardiac CT images as well as its respective left ventricular segmentation. We evaluate our method using a reconstruction schema, for this, the resulting 3D optical flow was applied over the volume at time t to obtain an estimated volume at time $t + 1$. We compared our 3D optical flow approach to an improved multi-resolution version of Horn and Shunck's 3D method for different levels of noise.

Contents

List of Figures

List of Tables

List of Symbols

(x, y)	two-dimensional space
σ	standard deviation
$L(x, y)$	Image in gray scale
$L(x, y, t)$	A spatio-temporal distribution of the intensity of the image sequence in 2D
$L_{m,n-m}(x, y)$	The Hermite coefficients in 2D
$l_{m,n-m,\theta}(x_0, y_0)$	The steered Hermite coefficients in 2D
γ	Weight parameter
α	Softness parameter

Abbreviations

WHO	World Health Organization
CVDs	Cardiovascular diseases
LV	Left Ventricular
MRI	Magnetic Resonance Imaging
CT	Computed Tomography
PET	Positron Emission Tomography
3D	Three-dimensional space
2D	Two-dimensional space
$2D + t$	Two-dimensional space plus time
$3D + t$	Three-dimensional space plus time
SHT	Steered Hermite transform
HVS	The human vision system
HT	The Hermite transform
HS	Horn and Schunck method
HOF2D	Horn-Hermite optical flow in 2D
HOF3D	Horn-Hermite optical flow in 3D
GT	Ground-truth reference
AE	Angular Error
EE	Endpoint Error
IE	Interpolation Error
NE	Normalized Interpolation Error
ECG	Electrocardiogram
RMS	Root mean-square

Chapter 1

Introduction

According to the World Health Organization (WHO), cardiovascular diseases (CVDs) take the lives of 17.9 million people every year, 31% of all global deaths, this represents the number one cause of death globally, more people die annually from CVDs than from any other cause [1]. Heart diseases as myocardial infarction, ischemia or hypertrophy can be characterized by analyzing the dynamics of the heart. During the cardiac cycle (contraction "systole" and relaxation "diastole" of the heart), the motion wall estimation can be used to recognize those pathologies. The acquisition of cardiac volumes has allowed quantifying relevant left ventricular (LV) parameters such as its volume, strain, twist, and desynchrony [2]. Nowadays, there are diagnostic imaging techniques to characterize cardiac anatomy and function, as such echocardiography, cardiac Magnetic Resonance Imaging (MRI), cardiac Computed Tomography (CT), cardiac Positron Emission Tomography (PET), and coronary angiography [3]. Where the cardiac CT technique has certain advantages with respect other: a higher resolution than ultrasound, it is more accessible than MRI and it is a non-invasive a fast imaging option [4]. Cardiac CT allows acquiring three-dimensional morphological images, with motion artifacts minimizes, and showing the heart chambers and the coronary arteries at different planes [5]. It is then possible to acquire good quality cardiac CT data of the heartbeats. Images are acquired overall cardiac cycles to produce the final volume image. Due to the complexity of the heart motion, it is still hard for the physician to estimate the 3D motion during the exam, thus, it is necessary to develop computational analysis tools to aid in the diagnosis process.

The human heart is a complex organ in terms of anatomy and physiology, the estimation of its movement is an important task to understand its mechanism and to assist in the medical diagnosis. Different image processing techniques can be applied to calculate and to observe the motion of the heart, for example, the optical flow (OF) estimation is a method used in those situations where the correspondence between the pixels, within an image sequence, is required. The optical flow methods compute an approximation to the 2D motion in an image sequence from spatiotemporal patterns of image intensity [6]. Over the years, state-of-the-art algorithms for optical flow can be summarized in Nagel [7] who identified

the common rigorous restrictions [8, 9, 10], as well as smoothing restrictions for the optical flow solution [7, 11, 12]. On the other hand, Barron et al. [6], classified the methods for calculating the optical flow into four groups: differential techniques [7, 8, 9, 11, 13, 14], region-based matching [15, 16], energy-based methods [17, 18] and phase-based techniques [19]. Sun et al. [20] suggested that there have been few changes in the typical formulation given by Horn and Schunck (HS) [11]. Most of the optical flow methods investigated here have been carried out in two dimensions ($2D + t$). Although this trend cannot be firmly stated, it must be taken into account and could be because, in $3D + t$, optical flow estimations increase the need to perform more calculations at the same time, which significantly increases the processing resources, memory, and execution time of the methods involved. It is also necessary to mention that some publications use the term of 3D optical flow calculation to refer to the calculation of optical flow in $2D+t$. Some of them, use 2D projections to obtain a 3D representation, in applications such as tracking traffic [21], in methods used for quantitative motion estimation of biological structures in light microscope [22], estimation of 3D geometry and 3D motion using spatiotemporal gradients [23] or emotion recognition from 3D videos [24]. 2D optical flow estimation has been used in the heart analysis to identify patients with some diseases, recent works using 2D optical flow cover topics such as motion estimation in cardiac fluorescence imaging [25], and as the automatic localization of the heart from cine MRI [26]. Some optical flow methods have used image models inspired by nature, for example Gabor filters [18, 19, 27, 28, 29, 30]. The optical flow is fundamentally different than tracking because a complete set of correspondences between the pixel levels in an image (or volume) is obtained. The optical flow is used to calculate dense trajectories, provides more freedom and information about the data in which the movement is being estimated, a priori models are not needed and even more, it can also be used to develop deformable based-model tracking algorithms.

The Hermite transform (HT) has been an image model used to describe the local constraints of the Horn and Schunck approach. Liu et al. [27] derived a six-parameter non-affine optical flow model, which is solved with high-order Hermite polynomial filtered data. In [28], Silvan et al. showed that through a linear mapping of 3D Hermite coefficients by specific projection functions, we could obtain the Hermite transform coefficients of local projections. Furthermore, Moya et al. [29] used the steered Hermite coefficients like local motion restrictions, found in current methods, to define a differential estimation method.

One disadvantage of the 2D cardiac movement analysis is that it is constrained by geometry-dependent reference directions of deformation (i.e., radial, circumferential, and longitudinal). In this sense, a 3D cardiac movement analysis may overcome such limitations by referencing the intrinsic directions of deformation [31]. Thus, to identify altered ventricular function in patients with CVD, a 3D left ventricular deformation analysis is more suitable since it represents contributions from counter-directional, helically arranged fibers shortening and thickening throughout the cardiac cycle [32]. Research on the measurement of cardiac motion has been commonly made in $2D + t$ [33] but this analysis should be done in $3D + t$ to enable us to describe the true motions of the heart, for example, the twisting motion that takes place on every beat cycle. Compared to the 2D analysis, the 3D analysis

has not received much attention, although there are currently working groups analyzing optical flow in 3D mainly using ultrasound images.

About the estimation of 3D optical flow in general, some works have similarities with at least one of the aspects of this work, thereby, in [34] they use a 3D model of the human body and motion-captured data to synthesize flow fields and train a convolutional neural network (CNN) to estimate human flow fields from pairs of images. In [35] a steerable filter-based algorithm is formulated, in its simplest form, for estimating 3D flow in sequences of volumetric or point-cloud data.

In [36] they present an approach for real-time respiratory motion estimation in image-guided interventions by employing contrast-invariant feature descriptors. Yoon et al. [37] presented a method for motion estimation applied to cone-beam CT, their work uses an energy functional, which includes as terms: a data fidelity, a regularization term, and the optical flow restriction. On the other hands, Jungwon et al. [38] used the optical flow estimation to calculate the local motion, allowing a 3D segmentation extension. Their model includes a shape distortion over time term, allowing segmenting and tracking the lung nodules. In [39], an implementation based on the optical flow algorithm from Farnebäck (2003) is used to create 3D freehand ultrasound but with reconstructions from 2D without external tracking, using deep learning.

Several methods have been used to estimate the optical flow of the endocardial wall motion [40]. In [41], a global anatomically constrained affine optical flow tracking was used to track the end-diastole left ventricle surface throughout the cardiac cycle. For [42], this approach first performs 3D segmentation at the end-diastolic frame and then performs tracking over the cardiac cycle using both global (optical flow) and local (block matching) methods. In [43] they claim to have a method for detecting cardiac flow in echocardiography where the sampling planes representing the mitral inflow tract and the left ventricle outflow tract are traced by fusing information from multiple cues, including optical flow, boundary detection, and motion prior. Duan et al. [44], evaluate a correlation-based optical flow algorithm for tracking endocardial surfaces on three-dimensional ultrasound data, also in [45] they built a truly 3D mathematical phantom of cardiac tissue and blood to validate the optical flow for quantification of myocardial deformations. Leung et al. [46] track left ventricular borders in 3D echocardiographic sequences by combining differential optical flow with statistical modelling. Zhiang et al. [47] developed an optical flow algorithm based on Thirion's diffusing model [48], also known as the "demons" algorithm and also described an atlas-based geometry pipeline for constructing three-dimensional cubic Hermite finite element meshes of the human heart.

In Table 1.1 we summarized some of the most recent optical flow motion methods used to extract the motion estimation, either using a $2D+t$ or $3D+t$ model, and the differences with the proposed method. In some cases, a 2D optical flow is initially estimated to map it onto a 3D optical flow.

Table 1.1: $2D/3D+t$ optical flow estimation approaches.

Paper	**OF model $2D/3D+t$**	**Method**	**Application**	**Evaluation Metric**
Proposed method	3D	Using the 3D Steered Hermite Transform	Left ventricle CT sequences	Interpolation errors in 3D
Ranjan et al. [34]	3D	A 3D model human body and a CNN	Estimate human flow fields	End point error
Alexiadis et al. [35]	2D	Minimizing a cost functional	3D flow estimation	Mean angular error on synthetic images
Queiros et al. [41]	3D	Anatomically affine optical flow	Left ventricle tracking	Distance and Dice metrics
Patil et al. [24]	2D	Farnebäck	Emotion recognition	Accuracy of 6 emotions
Saleh et al. [26]	2D	Lucas-Kanade	Heart Localization	Accuracy on localizing
Baghaie et al. [30]	2D	Gabor, Schmid and steerable filters	2D flow estimation	Angular and interpolation errors
Rodriguez et al. [25]	2D	Horn & Schunck	Cardiac motion estimation	Mean square error

In this work, we propose a differential method for estimating the three-dimensional optical flow, in cardiac CT images, using the 3D steered Hermite transform (SHT). The proposed method uses a three-dimensional ($3D+t$) approach, that is, it uses the data of the cardiac volumes in a three-dimensional space (x, y, z), which change over time during the entire cardiac cycle; and a modified version of Sun [20], which, in contradistinction of Horn and Schunck's approach [11], uses an incremental multi-resolution technique to estimate large displacements, where the optical flow at a coarse level is extrapolated to warp the second image at a finer level, combined with the optical flow based on the Hermite

transform proposed by Moya et al. [29], which uses the several constraints found in the more accurate optical flow methods in 2D [49, 50, 51]. We use local image constraints as mentioned in [11, 51] and assume that the flow is piecewise smooth as in [49, 50]. The proposed optimization function is robust for outliers [52] and a multiple-resolution strategy was implemented to manage large displacements as discussed in [15, 52, 53]. The results obtained were published in the proceedings of the conference in [54], and in the article of journal [55].

1.1 Structure of the thesis

This thesis is structured as follows:

In Chapter 2 we present the general concepts of the Hermite transform, as well as the main mathematical representations and interpretations related to the human vision system (HVS). Subsequently, the development is extended to 3D.

Chapter 3 defines the general concepts of optical flow estimation. We define the main aspects that allow us to calculate the estimation of the movement using this methodology, we review a brief taxonomy of the optical flow and then focus on the differential methods, both in 2D and 3D, which represent the basis of this project.

Chapter 4 describes the proposed model and method for conducting this investigation. The main hypothesis of 3D motion estimation with a modified differential method is presented, using the Hermite steered transform. In Appendix C, we see an example of the step-by-step calculation of one of the 2D differential methods described, to numerically express a simple but specific result.

Chapter 5 shows the main experiments and results obtained with the proposed method. The materials and evaluation metrics used in both 2D and 3D are presented. The results are contrasted with other methodologies and results reported in the literature to confirm the effectiveness of the proposed model. Subsequently, a brief discussion of the results obtained is developed. As additional topics of this chapter, a brief description of the sections of interest regarding the acquisition of images using computed tomography are given in Appendix A. In Appendix B, we increase visualizations to those shown previously, to accommodate different ways of representing the results obtained. In Appendix D, we include the registered article journal that is related to this investigation.

Finally, Chapter 6 provides the conclusions of the development and results of the research carried out.

Chapter 2

The Hermite transform

The Hermite transform, introduced by Martens [56], is a model that represents the basis of the human vision system (HVS). The Hermite transform allows modeling the receptive fields of the human eye in its early stages in a similar manner by the derivative of Gaussian. In the analysis stage, it separates the contained visual information from low and high frequencies, which makes the Hermite transform a good descriptor of the characteristic patterns that can consist of edges and textures.

Various research groups around the world have reported papers where they use the Hermite transform mainly for image processing. The LIRIS (Laboratoire d'InfoRmatique en Image et Systèmes d'information) Group of Lyon Francia, reported a writer identification model [57], a texture feature extraction [58], and the evaluation of handwriting similarities [59]. The Institute of Mathematics and Computing Science of the University of Groningen in the Netherlands and Universita' degli Studi of Roma, Italy have published a closed form of the steered elongated Hermite-Gauss wavelets [60]. Members of the Faculty of Computational Mathematics Cybernetics at Moscow State University reported a texture parameterization [61]. The department of Electronics Engineering Madras Institute of Technology in India, have analyzed of schizophrenia disorder in magnetic resonance brain images [62]. The University "Campus Bio-medico" of Rome, Italy described a local orientation estimation by tomographic slices [63]. The department of Mathematical Analysis, Ghent University at Belgium published a paper about the higher dimensional Hermite transform [64]. The Mathematics department of the University of California at San Diego, USA reported an accurate image rotation algorithm [65]. All of them using the Hermite transform as a mathematical tool for their researches.

2.1 The Hermite transform as a model of image representation

The Hermite transform is an image description model [56, 66] and a special case of polynomial transform.

An interesting special case of 2-D polynomial transforms arises when we have a window function which is separable i.e., $v(x, y) = v(x)v(y)$

For a perceptual standpoint and according to the scale-space theory [67, 68, 69], we would use a Gaussian window (Fig. 2.1):

$$v(x, y) = \frac{1}{\sigma\sqrt{\pi}} \exp\left(-\frac{(x^2 + y^2)}{2\sigma^2}\right) \tag{2.1}$$

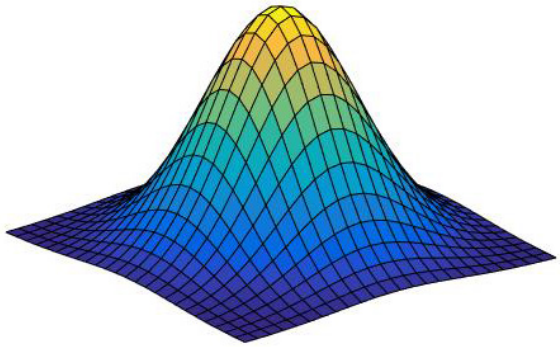

Figure 2.1: Gaussian window $v(x, y)$.

Gaussian windows in two dimensions have the property of being rotationally symmetric and spatially separable. Gaussian windows separated by twice the standard deviation, are a good model found for the receptive fields of perception found in psychological experiments [69]. According to the psychophysical model of HVS [70, 71], through Gaussian windows, we can decompose an image into several orthogonal polynomials. In the human eye, the retina (Fig. 2.2) is made up of several layers of different kinds of cells. The sensitive rods and cones are found in the back of the retina, in the opposite direction to the light. The light must first travel through blood vessels, nerve bers, and then several layers of retinal nerve cells in order to reach them.

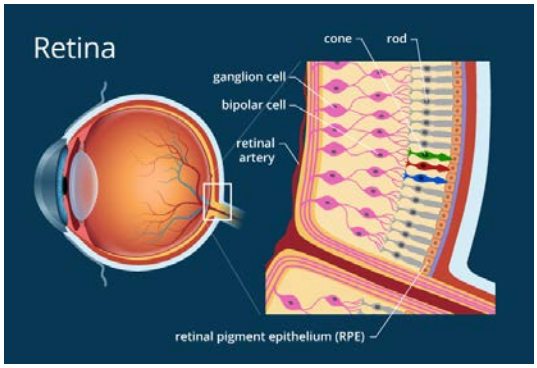

Figure 2.2: Chambers of the Eye [72].

If we look at the retina carefully (Fig. 2.3(a)), we can see the rods and cones. Three kinds of nerve cells are in front of them: bipolar cells, horizontal cells, and amacrine cells. Bipolar cells receive input from the cones and feed many into the cells of the retinal ganglion. Horizontal cells, in turn, connect bipolar cells and bipolar cells with amacrine cells. The eye has approximately 1 million ganglion cells [73].

Ganglion cells' aim is not completely understood, but color vision involves them. Ganglion cells from the receptive field (Fig. 2.3(b)), compare signals from many distinct cones. They seem to perceive the second local Gaussian derivative discovered in the HVS psychophysical modeling (Fig. 2.4).

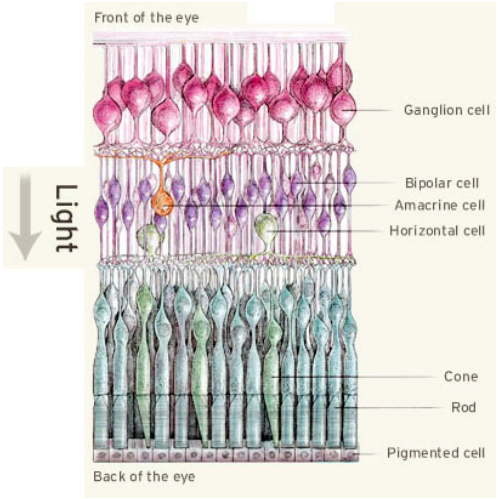

(a) ***Rodes and cones***

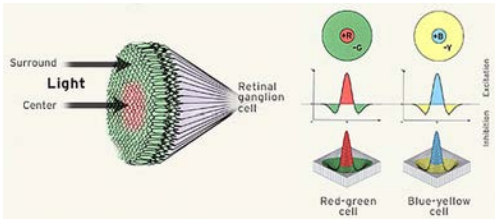

(b) ***Receptive field***

Figure 2.3: Detail of the retina [73].

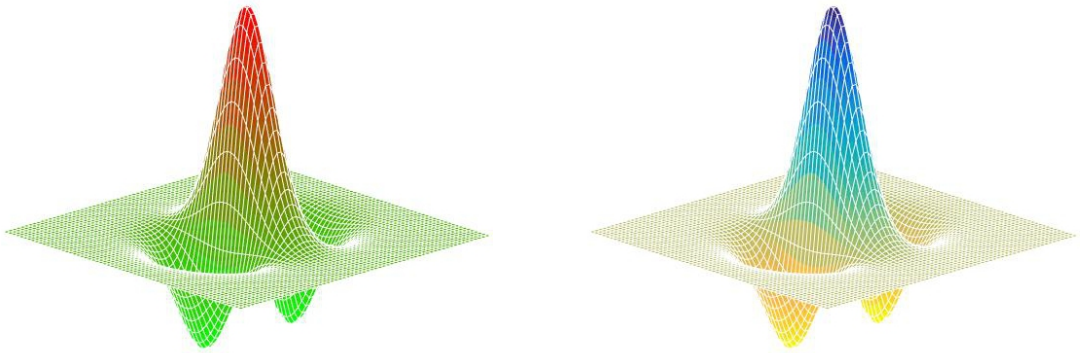

(a) ***Red-green receptive field*** **(b)** ***Blue-yellow receptive field***

Figure 2.4: The second Gaussian derivative in the HVS model.

2.2 The Hermite Transform in 2D

The polynomial coefficients of the Hermite transform are obtained by performing a convolution of the image $L(x, y)$ with the filter functions $D_{m,n-m}(x, y)$, followed by a subsampling (T) at position (x_0, y_0) of the sampling laticce S:

$$L_{m,n-m}(x_0, y_0) = L(x, y) \otimes D_{m,n-m}(x, y) \tag{2.2}$$

where $L_{m,n-m}(x, y)$ are the Hermite coefficients, m and $(n - m)$ denote the analysis order in x and y direction respectively with $n = 0, 1, \ldots, \infty$, $m = 0, 1, \cdots, n$ and $D_{m,n-m}(x, y)$ are the Hermite filters which are determined by an analysis window $v^2(x, y)$ that expands the local information in terms of a family of polynomials $G_{m,n-m}(x, y)$. In Figure 2.5 we can see the block diagram of the direct polynomial Hermite transform, and in the Figure 2.6 we can see the typical graphical distribution of the Hermite coeffcients.

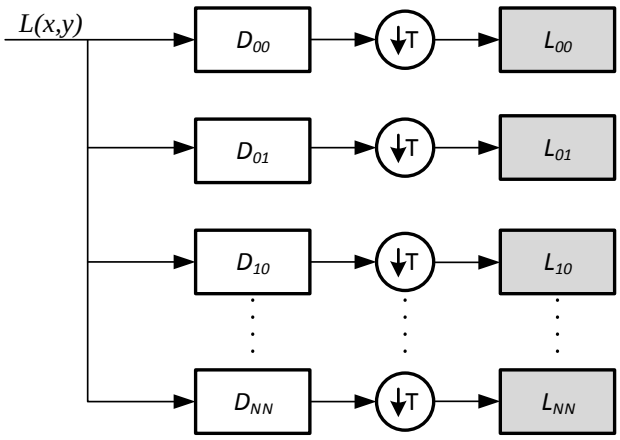

Figure 2.5: Block diagram of the direct polynomial transform.

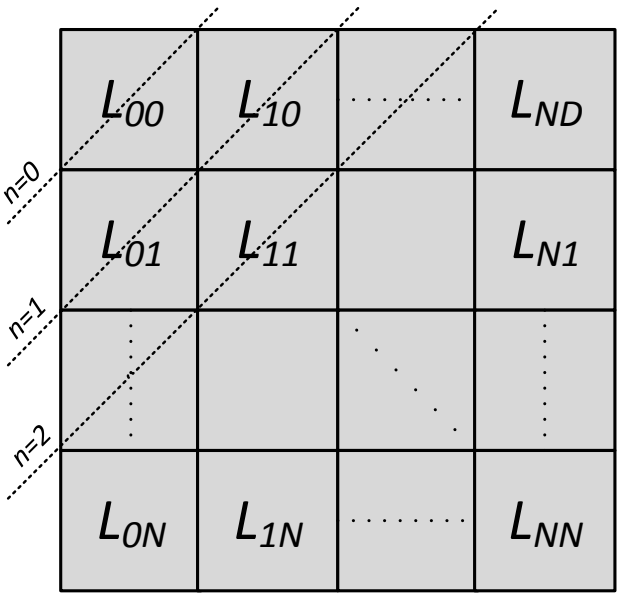

Figure 2.6: Graphical distribution of the Hermite coeffcients.

In order to calculate the Hermite transform, the original image $L(x, y)$ is located at various positions multiplying it by the window function $v^2(x - x_0, y - y_0)$ at positions (x_0, y_0) within the sampling lattice S

Physiological experiments suggest using overlapping Gaussian windows separated by

twice the standard deviation σ, in agreement with the overlapping receptive fields of the human visual system [69].The polynomials that are orthogonal with respect to the Gaussian window function are defined by:

$$G_{m,n-m}(x,y) = \frac{1}{\sqrt{2^n m!(n-m)!}} H_m\left(\frac{x}{\sigma}\right) H_{n-m}\left(\frac{y}{\sigma}\right) \tag{2.3}$$

where H_n represents the generalized Hermite polynomials given by Rodrigues's formula [74]

$$H_n(x) = (-1)^n \exp(x^2) \frac{d^n}{dx^n} \exp\left(-x^2\right) \tag{2.4}$$

The polynomials $G_{m,n-m}(x,y)$ used to approximate the information within the window are determined by the analysis window and satisfy the orthogonality condition:

$$\int_{-\infty}^{\infty}\int_{-\infty}^{\infty} v^2(x,y)\, G_{m,n-m}(x,y)\, G_{l,k-l}(x,y)\, dxdy = C_{nk}\delta_{nk}\delta_{ml} \tag{2.5}$$

for $n,k = 0,...,\infty$, $m = 0,...,n$ and $l = 0,...,k$; where δ_{nk} denotes the Kronecker function ($\delta_{nk} = 1$ for $n = k$ and $\delta_{nk} = 0$ for $n \neq k$). When polynomials are orthonormal, we have that $C_{nk} = 1$.

The analysis functions (the Hermite filters) determine what information is made explicit in the coefficients of the Hermite transform, so the main properties of this transform are determined by these functions.

The bidimensionals Hermite filters can be represented by:

$$D_{m,n-m}(x,y) = G_{m,n-m}(-x,-y)\, v^2(-x,-y) \tag{2.6}$$

The Hermite filters are separable because the Gaussian window is rotationally symmetric:

$$D_{m,n-m}(x,y) = D_m(x) D_{n-m}(y) \tag{2.7}$$

and those can be computed by:

$$D_m(x) = \frac{(-1)^m}{\sqrt{2^m m!}} \frac{1}{\sigma\sqrt{\pi}} H_m\left(\frac{x}{\sigma}\right) \exp\left(-\frac{x^2}{\sigma^2}\right) \tag{2.8}$$

Figure 2.7 shows a test image (a house) and Figure 2.8 presents its respective cartesian Hermite coefficients for $N = 3$ ($n = 0,1,2,3$).

Figure 2.7: Test image for evaluating the cartesian Hermite coefficients.

In the same way, in figure 2.10, we can see the Cartesian Hermite coefficients for figure 2.9, which is a reformatted short-axis CT image corresponding to the left ventricle in this test.

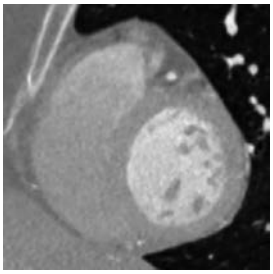

Figure 2.9: Reformatted short-axis image corresponding to the left ventricle.

The recovery process of the original image (inverse Hermite transform - IHT) consists of interpolating the Hermite coefficients through the proper synthesis filters:

$$\hat{L}(x,y) = \sum_{n=0}^{\infty} \sum_{m=0}^{n} \sum_{x_0,y_0 \in S} L_{m,n-m}(x_0,y_0) P_{m,n-m}(x-x_0, y-y_0) \tag{2.9}$$

where $P_{m,n-m}(x,y)$ can be determined by:

$$P_{m,n-m}(x,y) = \frac{G_{m,n-m}(x,y)v^2(x,y)}{\sum_{(x_0,y_0)\in S} v^2(x-x_0, y-y_0)} \tag{2.10}$$

for $m = 0, ..., n$ and $n = 0, ..., \infty$.

In Figure 2.11 we show the synthesis process of the Hermite transform.

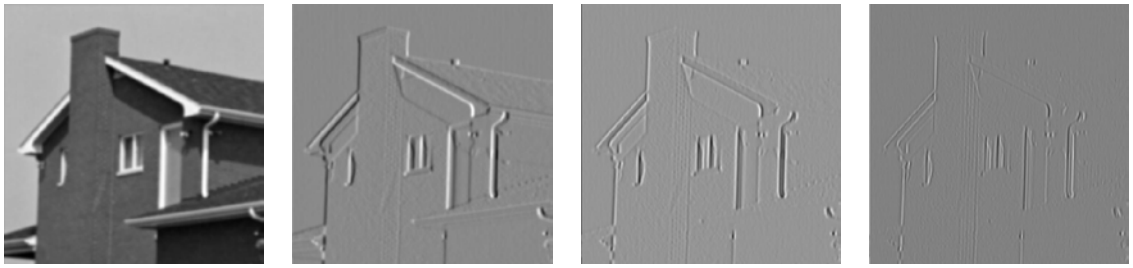

(a) $L_{0,0}(x, y)$ **(b)** $L_{1,0}(x, y)$ **(c)** $L_{2,0}(x, y)$ **(d)** $L_{3,0}(x, y)$

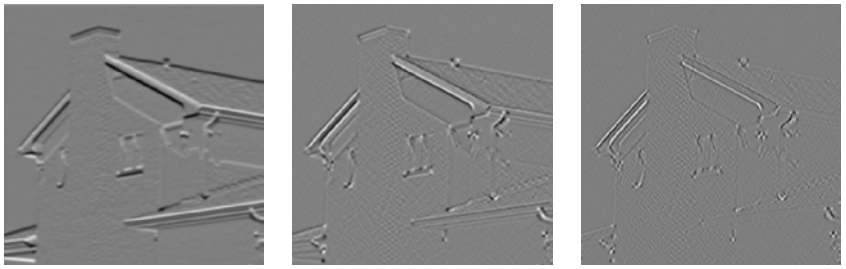

(e) $L_{0,1}(x, y)$ **(f)** $L_{1,1}(x, y)$ **(g)** $L_{2,1}(x, y)$

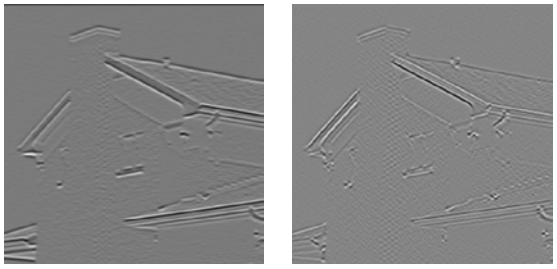

(h) $L_{0,2}(x, y)$ **(i)** $L_{1,2}(x, y)$

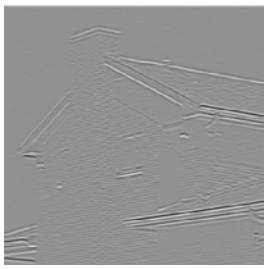

(j) $L_{0,3}(x, y)$

Figure 2.8: Cartesian Hermite coefficients of a house image.

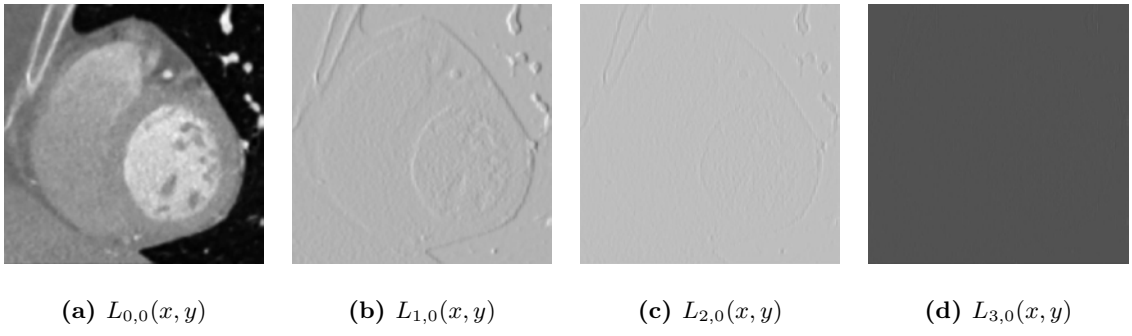

(a) $L_{0,0}(x, y)$ **(b)** $L_{1,0}(x, y)$ **(c)** $L_{2,0}(x, y)$ **(d)** $L_{3,0}(x, y)$

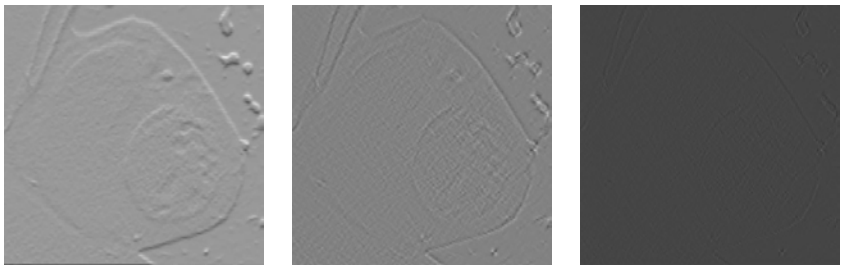

(e) $L_{0,1}(x, y)$ **(f)** $L_{1,1}(x, y)$ **(g)** $L_{2,1}(x, y)$

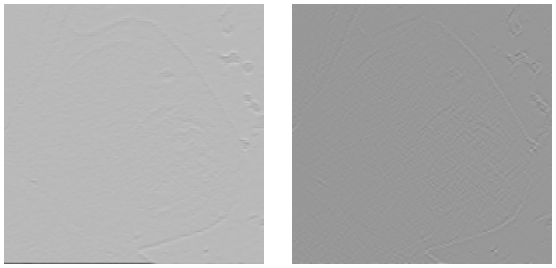

(h) $L_{0,2}(x, y)$ **(i)** $L_{1,2}(x, y)$

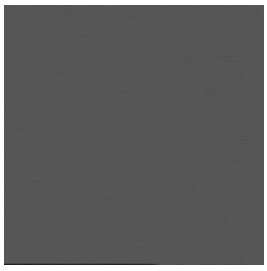

(j) $L_{0,3}(x, y)$

Figure 2.10: Cartesian Hermite coefficients of a reformatted short-axis CT image of a left ventricle.

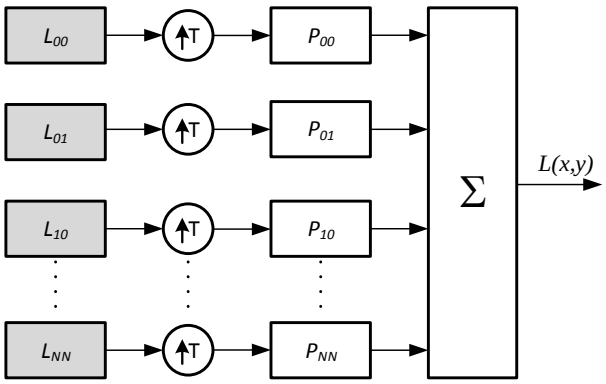

Figure 2.11: Synthesis process of the Hermite transform.

2.2.1 Steered Hermite Transform

Steered Hermite filters belong to a class of filters that are rotated copies of each filter, constructed as a linear combination of a set of basis filters [75]. Hermite filters, being the result of polynomials of a Gaussian function, radially symmetrical, have an orientation characteristic. So that from Hermite filters, they can be adapted to local content [76], which results in filters that can be seen as the directional derivatives of a Gaussian function. Thus, the $N+1$ Hermite filters of order n, form a steerable base of each filter of order n.

A steered version of the Hermite transform is obtained by projecting the Hermite coefficients towards an orientation angle θ. The Hermite filters at each position in the image are projected to an angle given by the orientation of the local image feature [76]:

$$l_{m,n-m,\theta}(x_0, y_0) = \sum_{k=0}^{n} L_{k,n-k}(x_0, y_0) g_{k,n-k}(\theta) \tag{2.11}$$

where

$$g_{k,n-k}(\theta) = \sqrt{\binom{n}{k}} \left(\cos^k(\theta)\right) \left(\sin^{n-k}(\theta)\right) \tag{2.12}$$

are the cartesian angular functions of order n that express the directional selectivity of the filter and $l_{m,n-m,\theta}(x_0, y_0)$ are the steered Hermite coefficients.

To obtain the steered Hermite coefficients, the cartesian Hermite coefficients are rotated toward the estimated local orientation, according to the maximum oriented energy criterion for each window position. For local 1D patterns, the steered Hermite transform is an efficient way to compactly describe image features into a smaller number of coefficients ($l_{0,n,\theta}(x, y) = l_{n,\theta}(x, y)$) that represent the profile of the pattern perpendicular to its orientation (θ) [76].

The two-dimensional polynomial coefficients are projected in coefficients of one dimension on an axis that makes an angle theta with the x-axis. The first-order polynomial coefficients resemble an optimal edge detector.

According to the Hermite coefficients, the energy content can be expressed through Parseval's theorem as:

$$E_N = \sum_{n=0}^{N} \sum_{m=0}^{n} \left[L_{m,n-m}\left(x,y\right)\right]^2 \tag{2.13}$$

The steered Hermite transform allows us to describe 1D patterns and for that, it is useful to find 1D energy in terms of 2D energy in the case of images. So for each local signal:

$$E_N^{1D} = \sum_{n=1}^{N} \left[l_{0,n,\theta}\left(x,y\right)\right]^2 \tag{2.14}$$

$$E_N^{2D} = \sum_{n=0}^{N} \sum_{m=0}^{n} \left[l_{m,n-m,\theta}\left(x,y\right)\right]^2 \tag{2.15}$$

So another way to calculate the energy content represented by Eq. (2.13), is:

$$E_N = \left[L_{0,0}\left(x,y\right)\right]^2 + E_N^{1D} + E_N^{2D} \tag{2.16}$$

The angle that represents the maximum energy direction is estimated according to:

$$\theta\left(x,y\right) = \arctan \frac{L_{01}\left(x,y\right)}{L_{10}\left(x,y\right)} \tag{2.17}$$

which is a good indicator of the direction of the edges, being L_{01} and L_{10} the cartesian coefficients in the horizontal and vertical directions respectively.

In Figure 2.12 we show the steered Hermite coefficients corresponding to the Figure 2.7 and its cartesian Hermite coefficients, presented in Figure 2.8

In Figure 2.13 we show the steered Hermite coefficients corresponding to the Figure 2.9, a reformatted short-axis CT image of a left ventricle.

2.2.2 The 3D Hermite Transform

The direct Hermite transform in 3D (HT3D), is a particular case of the proposal of Martens [56, 66], where a signal is localized by an analysis window and this information is expanded using polynomials orthogonal to the window. Polynomials that are orthogonal with respect to the Gaussian window function are defined by [77], so we would use the window:

$$v(x,y,z) = \frac{1}{\sqrt{\sigma\sqrt{\pi}}} \exp\left(-\frac{\left(x^2+y^2+z^2\right)}{2\sigma^2}\right) \tag{2.18}$$

(a) $L_{0,0}(x, y)$

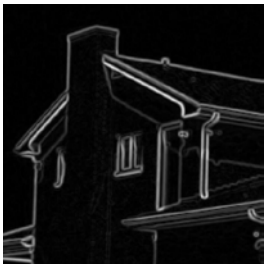

(b) $l_{1,0}(x, y, \theta)$

(c) $l_{2,0}(x, y, \theta)$

(d) $l_{3,0}(x, y, \theta)$

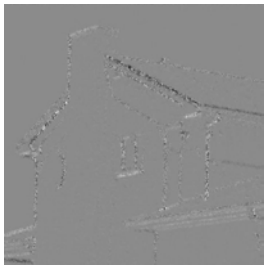

(e) $l_{0,1}(x, y, \theta)$

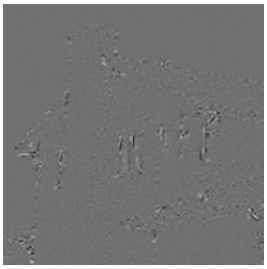

(f) $l_{1,1}(x, y, \theta)$

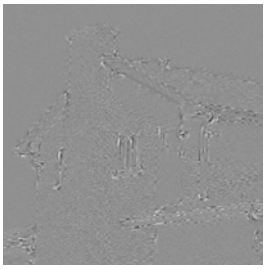

(g) $l_{2,1}(x, y, \theta)$

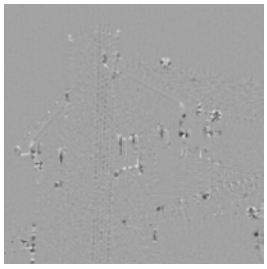

(h) $l_{0,2}(x, y, \theta)$

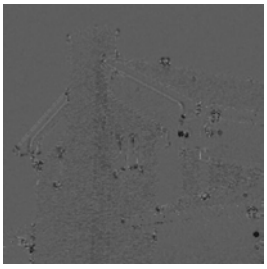

(i) $l_{1,2}(x, y, \theta)$

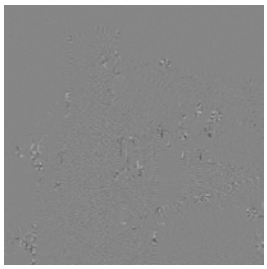

(j) $l_{0,3}(x, y, \theta)$

Figure 2.12: Steered Hermite coefficients of a test image.

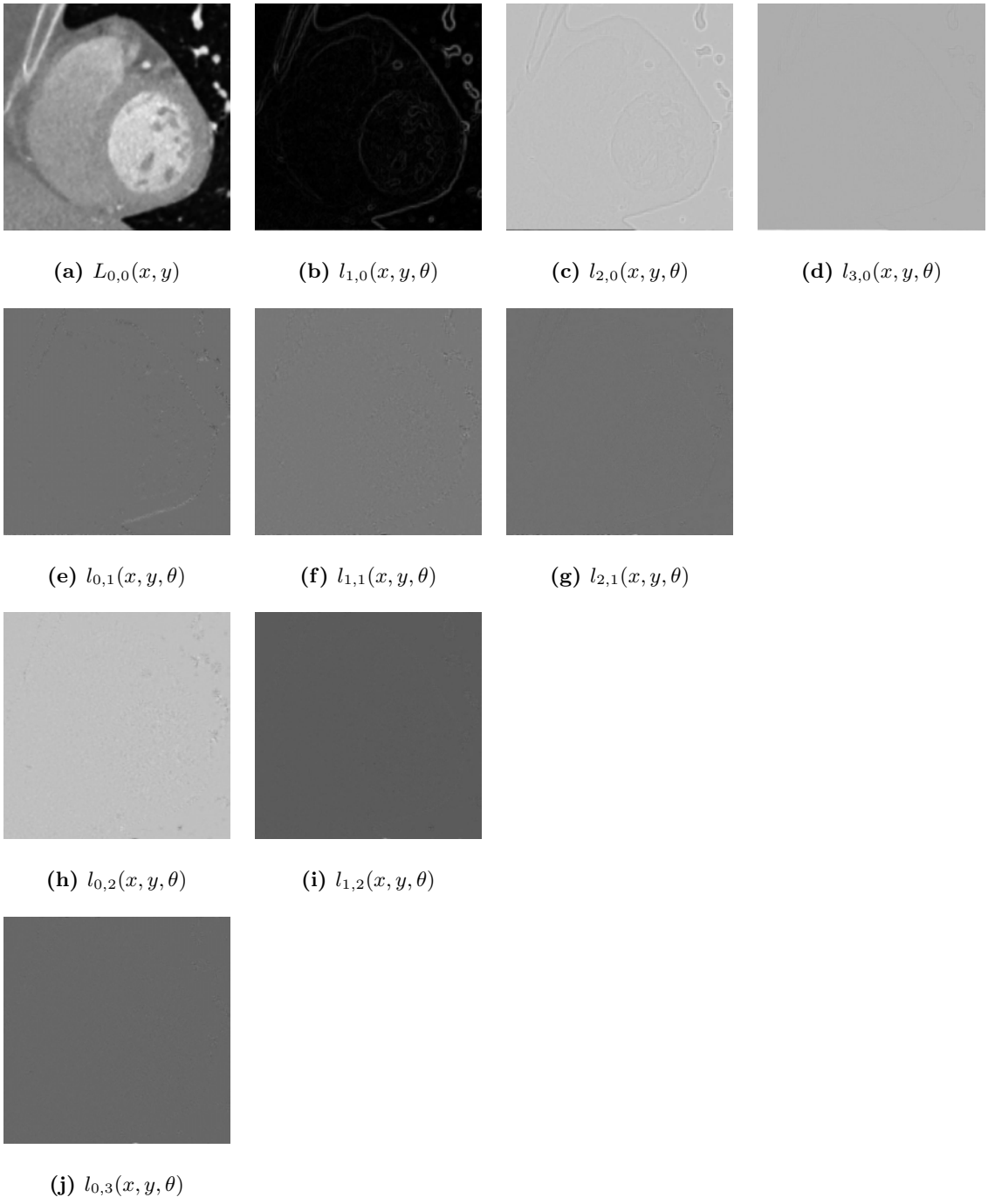

(a) $L_{0,0}(x, y)$ **(b)** $l_{1,0}(x, y, \theta)$ **(c)** $l_{2,0}(x, y, \theta)$ **(d)** $l_{3,0}(x, y, \theta)$

(e) $l_{0,1}(x, y, \theta)$ **(f)** $l_{1,1}(x, y, \theta)$ **(g)** $l_{2,1}(x, y, \theta)$

(h) $l_{0,2}(x, y, \theta)$ **(i)** $l_{1,2}(x, y, \theta)$

(j) $l_{0,3}(x, y, \theta)$

Figure 2.13: Steered Hermite coefficients of a reformatted short-axis CT image of a left ventricle.

Physiological experiments consider using overlapping Gaussian windows separated by twice the standard deviation σ which are isotropic and that's why we can establish that $\sigma = \sigma_x = \sigma_y = \sigma_z$ following the overlapping receptive fields of the human visual system [69].

The Hermite cartesian coefficients, $L_{l,m-l,n-m}$, are obtained by convolution of the original signal $L(x, y, z)$ with the analysis filters $D_{l,m-l,n-m}(x, y, z)$ followed by subsampling on a three-dimensional mesh S using Equation (2.19):

$$L_{l,m-l,n-m}(x_0, y_0, z_0) = L(x, y, z) \otimes D_{l,m-l,n-m}(x, y, z), \tag{2.19}$$

where l, $(m-l)$ and $(n-m)$ denote the analysis order in x, y and z directions, respectively; $l = 0, 1, \ldots, m$; $m = 0, 1, \ldots, n$; $n = 0, 1, \ldots, N$; N is the maximum order of the expansion that is related to the size of a cubic window of $\mathcal{M} \times \mathcal{M} \times \mathcal{M}$, where $N \leq 2*(\mathcal{M}-1)$. For large values of $\mathcal{M}$ the discrete cubic kernel reduces to the 3D Gaussian window.

The three-dimensional Hermite filters can be represented by:

$$D_{l,m-l,n-m}(x, y, z) = G_{l.m-l,n-m}\left(-x, -y, -z\right) v^2\left(-x, -y, -z\right) \tag{2.20}$$

wich are separable because the Gaussian window is rotationally symmetric

$$D_{l,m-l,n-m}(x, y, z) = D_l(x) D_{m-l}(y) D_{n-m}(z) \tag{2.21}$$

and those can be computed by:

$$D_l(x) = \frac{(-1)^l}{\sqrt{2^l l!}} \frac{1}{\sigma\sqrt{\pi}} H_l\left(\frac{x}{\sigma}\right) \exp\left(-\frac{x^2}{\sigma^2}\right) \tag{2.22}$$

$G_{l,m-l,n-m}(x, y, z)$ are a family of polynomials defined as:

$$G_{l,m-l,n-m}(x, y, z) = \frac{1}{\sqrt{2^n l!(m-l)!(n-m)!}} H_l\left(\frac{x}{\sigma}\right) H_{m-l}\left(\frac{y}{\sigma}\right) H_{n-m}\left(\frac{z}{\sigma}\right) \tag{2.23}$$

where H_l represents the generalized Hermite polynomials given by Rodrigues' formula [74]

$$H_l(x) = (-1)^l \exp(x^2) \frac{d^l}{dx^l} \exp\left(-x^2\right) \tag{2.24}$$

The recovery process of the original image (inverse Hermite transform in 3D - IHT3D) consists of interpolating the Hermite coefficients through the proper synthesis filters:

$$\hat{L}(x, y, z) = \sum_{n=0}^{N} \sum_{m=0}^{n} \sum_{l=0}^{m} \sum_{(x_0, y_0, z_0) \in S} L_{l,m-l,n-m}\left(x_0, y_0, z_0\right) P_{l,m-l,n-m}(x - x_0, y - y_0, z - z_0) \tag{2.25}$$

where $P_{l,m-l,n-m}(x, y, z)$ can be determined by:

$$P_{l,m-l,n-m}(x, y, z) = \frac{G_{l,m-l,n-m}(x, y, z) v^2(x, y, z)}{\sum\limits_{(x_0, y_0, z_0) \in S} v^2(x - x_0, y - y_0, z - z_0)} \tag{2.26}$$

for $l = 0, ..., m$; $m = 0, ..., n$ and $n = 0, ..., N$.

From Equation (2.25), instead of to recover the original volume we obtain an approximation of the original signal $\hat{L}(x, y, z)$, where the quality of this reconstruction improves by increasing the maximum order of the expansion N, i.e., the size of the cubic window $\mathcal{M}$ [66]. In terms of the artifacts in the approximated volume $\hat{L}(x, y, z)$, small values of the cubic windows causes "speckles", while high values result in Gibbs-phenomenon-like artifacts such as ringing and blur [76].

Thus, to determined the maximum order or the expansion N and in consequence the size of the cubic window $\mathcal{M}$, in [76] van Dijk and Martens determined that using an expansion of the Hermite transform equal to 3, the reconstructed 2D image will contain the most quantity of AC energy (84%) according to Parseval's theorem. In general, with $N \geq 3$ we can obtain a good reconstruction and with much greater values we will obtain a perfect reconstruction of the image.

3D Steered Hermite Transform

The Steered Hermite transform (SHT) is a variant of the HT that adapts to the local orientation of the image [76], it uses rotated filters which are represented as a linear combination of basis filters [75]. The orientation property of these steered Hermite filters is due to the symmetric-radial form of the Gaussian window, thus they can saw as the response of directional derivatives of the Gaussian function.

On the other hand, the SHT describes local 1D patterns in images into a smaller number of coefficients that represent the profile of the pattern perpendicular to its orientation [76].

By projecting the 3D Cartesian Hermite coefficients towards the local orientation angles θ and ϕ (Figure 2.14), we obtain the Steered Hermite transform in 3D (SHT3D) as shown in Equation (2.27):

$$l_{l,m-l,n-m,\theta,\phi}(x_0, y_0, z_0) = \sum_{m=0}^{n} \sum_{l=0}^{m} \left(L_{l,m-l,n-m}\left(x_0, y_0, z_0\right) \cdot g_{l,m-l}\left(\theta\right) \cdot g_{m,n-m}\left(\phi\right) \right) \quad (2.27)$$

where $l_{l,m-l,n-m,\theta,\phi}(x_0, y_0, z_0)$ are the 3D steered Hermite coefficients. And

$$g_{j,k-j}(\varphi) = \sqrt{\binom{k}{j}} \left(\cos^{j}\left(\varphi\right) \sin^{k-j}\left(\varphi\right) \right) \quad (2.28)$$

is the cartesian angular function that expresses the directional selectivity of the filter.

To calculate the direction of maximum energy we used the coefficients from Equation (2.19) and the phase of the gradient given by Equations (2.29) and (2.30):

$$\theta = \arctan\left(\frac{L_{010}}{L_{100}}\right) \quad (2.29)$$

$$\phi = \arctan\left(\frac{\sqrt{(L_{100})^2 + (L_{010})^2}}{L_{001}}\right) \tag{2.30}$$

where $[L_{1,0,0}, L_{0,1,0}, L_{0,0,1}]\,(x, y, z)^\top$ are a good approximation of the 3D gradient through the Cartesian Hermite coefficients.

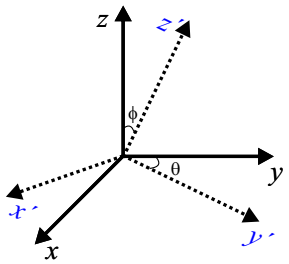

Figure 2.14: Cartesian coordinates (continuous line), steered coordinates (dotted line), and the angles θ and ϕ.

To graphically represent the indexes of the 3D Cartesian Hermite coefficients, Figure 2.15 shows the distribution of order two ($N = 2$) in each direction, in this case 27 coefficients are obtained for each voxel of a volume.

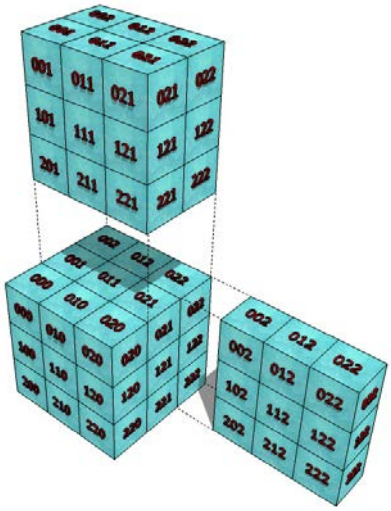

Figure 2.15: Distribution of the index of Cartesian Hermite coefficients of a second-order voxel.

Figure 2.16 shows an example of some 3D Steered Hermite coefficients for the left ventricle of a cardiac CT volume, according to Equation (2.27) , where we can see the steered coefficients l_{000}, l_{100}, l_{010} and l_{001}.

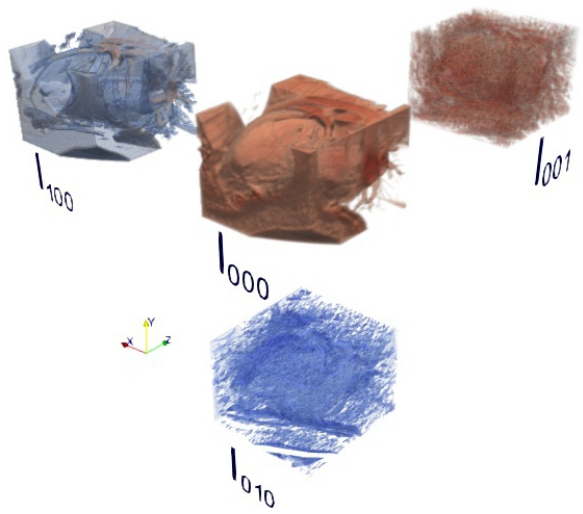

Figure 2.16: Ensemble of some Steered Hermite coefficients of a cardiac CT volume.

Chapter 3

Optical Flow Estimation

One of the fundamental issues in the processing of a sequence of images is the estimation of the optical flow, which is a useful and convenient representation of the movement observable in the sequence of the images to be considered.

Motion estimation can be used, for example, to evaluate the properties in a 3D scene, obtain the parameters of movement of a visual sensor, carry out the segmentation of some object within the images, warn about the movement dynamics (i.e., collisions or distance) between objects, calculate the disparity in the stereo images, apply it to video compression, measure the blood flow or estimate the movement of the heart walls, among other applications.

Optical flow is the pattern of the apparent movement of objects, surfaces, and edges in a scene, caused by the relative movement between an observer (an eye or a camera) and the scene. The concept of optical flow was first studied in the 1940s and, finally, was published by the American psychologist James J. Gibson [78] as part of his theory of affordance (an action that an individual can potentially perform in your environment).

The detection of the optical flow between two images taken at different times may be due to the movement of an object within the scene, the relative movement between the observer, and the scene or variations of brightness in the scene.

A problem encountered in the detection of optical flow is the so-called aperture effect. It is related to the problem of finding the same point in two consecutive images of a sequence. This problem can be found in objects that deform over time, objects with a periodic shape or simply in an image that has several identical objects that can not be distinguished, and therefore, it is impossible to know the correspondence of objects between different images of a sequence.

The analysis of the movement from a sequence of images involves the estimation of the relative movement between the objects of the scene and the images. One of the most important methods for estimating movement is based on the gradient. That is, in observing the change of intensity levels into the image. The optical flow reflects the changes in the image due to the movement during a time interval of dt. Thus, the optical flow field (velocity

field) represents the three-dimensional movement of points of the objects through the two-dimensional movement that represents the image. In the case of medical images, it represents the three-dimensional movement in the volume.

Observing a temporal change in the intensity of the image in a local area δS, a constraint equation can be obtained, analogous to the continuity equation [79]:

$$\frac{\partial}{\partial t}\int_{\delta S} L(x,y,t)dS = \oint L(x,y,t)\mathbf{w}\cdot\mathbf{n}dC + \int_{\delta S}\phi dS \tag{3.1}$$

where $L(x,y,t)$ is a spatio-temporal distribution of the intensity of the image sequence, δC is the contour enveloping δS, $\mathbf{w} = (u,v)$ is a velocity vector to be determined, $\mathbf{n}$ is a unit vector normal pointing to out of the δC contour, and ϕ is the ratio of intensity generation over a pixel in dS (Fig. 3.1). The intensity generation means a decrease or increase in the intensity of an image under non-uniform illumination. In Eq. (3.1), the calculation of the integral along the contour δC is transformed into the integral calculation on δS by the Gaussian divergence theorem, therefore the differential formula of Eq. (3.1) is as follows:

$$\frac{\partial L(x,y,t)}{\partial t} = -L(x,y,t)\mathrm{div}(\mathbf{w}) - \mathbf{w}\cdot\mathrm{grad}(L(x,y,t)) + \phi \tag{3.2}$$

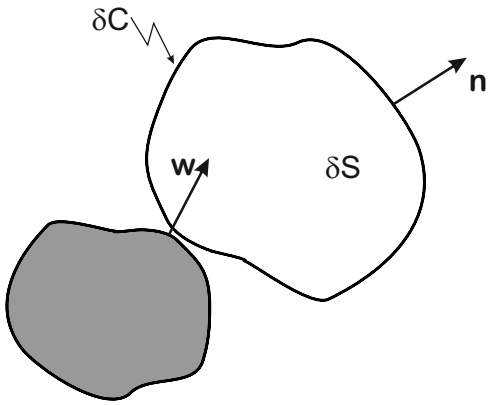

Figure 3.1: Optical flow constraint.

To solve the Eq. (3.2), the following constraints are usually formulated:

a) The divergence of $\mathbf{w}$ is zero ($\mathrm{div}(\mathbf{w}) = 0$) [79].

b) The intensity observed for any point of an object is constant in time under the specific conditions of movement of the cameras (if so), or movement of the objects in the scene, which means that the ratio of intensity generation of a pixel ϕ is null [80].

The constraint b) is perhaps somewhat demanding and would only be valid for example, for Lambertian surfaces, which move under homogeneous illumination invariant in time, for example, without light sources moving in the environment.

With these constraints, Eq. (3.2) becomes:

$$\frac{\partial L(x,y,t)}{\partial t} + \mathbf{w} \cdot \text{grad}(L(x,y,t)) = 0 \tag{3.3}$$

where *grad* refers to the spatial gradient of a two-dimensional image at the location (x, y) and is a fundamental equation for optical flow calculations. It is important to note that, although this equation is accurate under the previous assumptions when the derivatives are implemented as finite differences between the intensities of adjacent pixels, the equation can be expressed as a first-order Taylor series development for the temporal space variation of the intensity of the image [80]. Let's look at this statement in a little more detail. Suppose we have a continuous image; $L(x, y, t)$ refers to the intensity level of the pixel (x, y) at time t. Representing a dynamic image as a function of position and time, it is possible to express it as a Taylor series development:

$$\begin{aligned} L(x+dx, y+dy, t+dt) =& L(x,y,t) + \frac{\partial L}{\partial x}dx + \frac{\partial L}{\partial y}dy + \frac{\partial L}{\partial t}dt + O(\partial^2) \\ =& L(x,y,t) + L_x dx + L_y dy + L_t dt + O(\partial^2) \end{aligned} \tag{3.4}$$

where $O(\partial^2)$ are the higher order terms in Taylor's development that are neglected. It can be assumed that the immediate neighborhood of (x, y) moves some small distance (dx, dy) during the interval dt, that is, we can find dx, dy, dt such that:

$$L(x+dx, y+dy, t+dt) = L(x,y,t) \tag{3.5}$$

If dx, dy, dt are very small. The higher order terms in Eq. (3.4) can be neglected and therefore:

$$-L_t = L_x \frac{dx}{dt} + L_y \frac{dy}{dt} \tag{3.6}$$

The objective is to obtain the velocity $\mathbf{w} = \left(\frac{dx}{dy}, \frac{dy}{dt}\right) = (u, v)$ knowing that L_x,L_y and L_t are all measurable quantities or at least an approximate measure can be obtained from $L(x, y, t)$.

It can be observed that Eq. (3.6) is identical to Eq. (3.3), where the difference of the identity L_t in the same location (x, y) of the image, in the instants t and $t + dt$, is the result of the difference in the level of spatial intensity and the velocity in said location according to the observer.

In Eq. (3.6) it is conjectured that during the movement the intensity of the image remains constant along the trajectory S of the movement, resulting $\frac{dL}{dS} = 0$. This implies the following assumptions: any change in the intensity of the image is due to movement,

the illumination of the scene remains constant or the surfaces of the objects are opaque (Lambertian surfaces). Sometimes the assumption that the intensity remains constant is not true, particularly if the lighting changes, to avoid this possibility the constant gradient constraint is applied along the path of the movement, therefore, it is considered that and although the constant intensity constraint can be violated, what will remain constant along said trajectory is the gradient, that is $\frac{d\nabla L}{dS} = 0$.

3.1 Optical Flow Constraint

If we rewrite Eq. (3.6), we obtain the optical flow constraint as follows:

$$(L_x, L_y) \cdot (u, v) = -L_t \tag{3.7}$$

or

$$\nabla \mathbf{L} \cdot \mathbf{w} = -L_t \tag{3.8}$$

where $\nabla \mathbf{L} = (L_x, L_y)$ is the spatial intensity gradient and $\mathbf{w} = \left(\frac{dx}{dt}, \frac{dy}{dt}\right) = (u, v)$ is the velocity of the image or the optical flow in the pixel (x, y) at time t.

3.2 Aperture Effect

Due to the optical flow constraint (Eq. 3.8), where we have two unknowns and only one equation, the aperture problem holds that there is usually insufficient local intensity structure to measure the full velocity of the image, but sufficient to measure the normal component to the local intensity structure. Figure 3.2 shows an example of the aperture problem, where a line moving up and to the right is seen through a circular aperture. In this case, it is impossible to recover the full velocity of the image correctly, but only the normal velocity to the line. The problem of calculating the full velocity of the image becomes finding an additional constraint that gives us a second equation for the same number of unknowns.

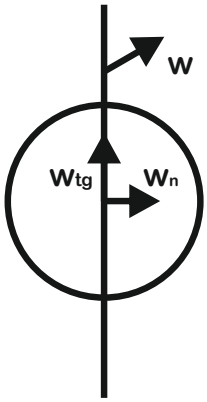

Figure 3.2: The aperture problem, we can only recover the normal velocity, the tangential does not.

Normal flow is a phenomenon that occurs when there is not enough local information of the local intensity structure to allow recovery of the full flow of the image. In this case, only the component of the normal flow to the local intensity structure (for example, an edge), $\mathbf{w}_n$, can be recovered. The tangential component of the flow ($\mathbf{w}_{tg}$) can not be recovered.

3.2.1 Aperture Effect in 3D

The problem of the aperture effect has to do with two types of normal velocity: normal velocity to the plane (the normal velocity to a local flat structure) and the normal velocity to a line (the normal velocity to a line caused by the intersection of two blueprints). The normal velocities to the plane and a line are shown in Figure 3.3 and can be briefly explained as follows:

- If the space-time derivative fits better to a simple plane, we have the normal velocity to the plane. The point in the plane closest to the origin $(0, 0, 0)$ is its magnitude and the normal of the surface of the plane is its direction.
- If the spatio-temporal derivative is better adjusted to the point of intersection of two separate planes, we have a normal velocity to the line.

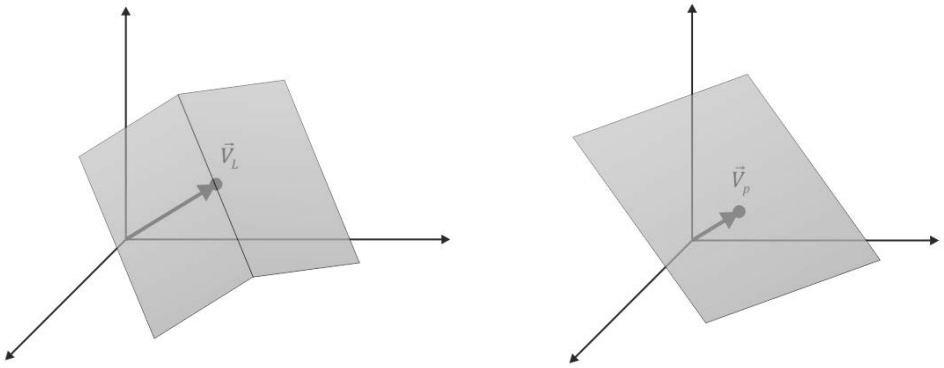

(a) ***Normal Velocity to Line*** **(b)** ***Normal Velocity to Plane***

Figure 3.3: Illustration of normal velocities to a line and a plane.

3.3 Optical Flow Estimation Methods

Despite the great variety of approaches, the algorithms for calculating optical flow can be divided into three categories [6]:

- Differential techniques. They are also known as "gradient" techniques, which estimate the optical flow vectors from those derives from the intensity of the image in space and time. These are usually obtained directly by considering the total temporal derivative of a "conserved" quantity, such as brightness.
- Correspondence techniques. These techniques operate by matching small regions of image intensity or specific "features" from one frame to the next. The match criterion is generally the least-squares or standardized correlation measures.
- Filter-based or frequency-based techniques. They rely on space-time oriented filters (that is, speed-sensitive), and are usually analyzed considering the motion problem in the Fourier domain. They are divided into two categories, phase-based, and energy-based.

Each previous technique has its advantages and disadvantages. Numerical differentiation is sometimes impractical due to the small temporary support or poor signal-to-noise ratio. In these cases, it is natural to consider correlation techniques. Among the advantages

provided by frequency-based methods, it is found that motion-sensitive mechanisms operating in space-time oriented energy in the Fourier domain can estimate the movement in image signals for which the correspondence techniques they would fail. An example is the movement of random dot patterns.

Beyond the differences between the different techniques, three common transformation phases can be determined:

1. Pre-filtered or smoothed with low pass filters, to extract the structure of the signal of interest and to improve the signal-to-noise ratio.

2. The extraction of some basic measurements, such as spatio-temporal derivatives (to measure the normal components of velocity) or local correlation surfaces.

3. The integration of these measurements to produce a flow field, which often involves assumptions about the smoothness of the underlying flow field.

Differential techniques calculate the speed from spatio-temporal derivatives of the intensity of the image or of filtered versions of the image (using low pass or bandpass filters). Their point in common is the hypothesis of the consistent intensity of a point during its movement, where it can be assumed that the intensity of a point remains constant throughout its trajectory. The hypothesis is known as the constraint of optical flow. The displacements can be considered small in which the changes of the light sources are small.

3.4 Classification of Constraints for the Estimation of the Optical Flow

Most of the constraints of the methods that estimate the optical flow can be derived from the continuity equation. Based on [81], Figure 3.4 shows the assumptions and tools used to derive constraints and their direct or indirect linkage with the continuity equation (Eq. 3.3), which establishes the conservation of $\mathbf{L}$ an amount under the flow $\mathbf{w}$. Thus, we define:

L.-	gray-value function
ϕ.-	local image phase
h.-	scalar function
α, β.-	indices
$\mathbf{u} = (u, v)$;	$\nabla_{xy} = (\partial_x, \partial_y)^t$
$\mathbf{v} = (u, v, 1)$;	$\nabla_{xyt} = (\partial_x, \partial_y, \partial_t)^t$
$\mathbf{w} = (u, v, w)$;	$H_L = \begin{pmatrix} \partial_{xx}L & \partial_{xy}L \\ \partial_{yx}L & \partial_{yy}L \end{pmatrix}$

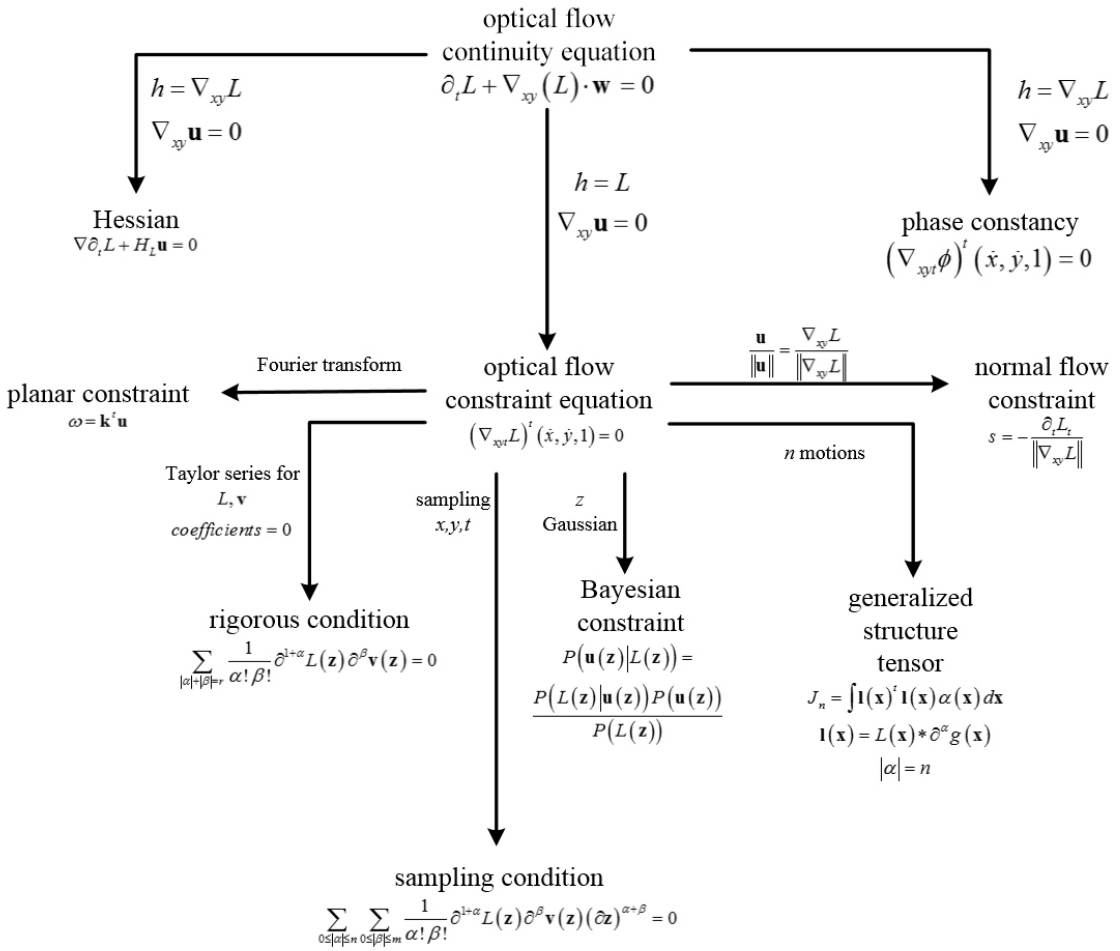

Figure 3.4: Classification of constraints for the estimation of optical flow

Here h it is supposed to be the grayscale version of L and the flow $\mathbf{w} = (u, v, w)$ is the optical flow for which $\nabla_{xy}\mathbf{w} = \mathbf{0}$. It can be seen that $\nabla_{xy} = (\partial_x, \partial_y)^t$ denotes the divergence operator applied to the two spatial dimensions x, y, while $\mathbf{v} = (u, v, 1)$, and $\nabla_{xyt} = (\partial_x, \partial_y, \partial_t)^t$ denotes the divergence operator applied to the two spatial dimensions x, y to the temporal dimension. The superscript t denotes the transpose. The constraint $\nabla_{xy}\mathbf{w} = \mathbf{0}$ means that in the regions of constant gray values there is no change in the flow, in other words, said gray values do not "accumulate flow", as for example, the mass does in a fluid. Then, the optical flow constraint equation is transformed into the optical flow constraint equation:

$$(\nabla_{xyt}L)^t(\dot{x}, \dot{y}, 1) = 0 \tag{3.9}$$

If the same continuity constraint applies to motions, this brings us to the generalized structure tensor:

$$J_n = \int \mathbf{l}(\mathbf{x})^t \mathbf{l}(\mathbf{x})\, \alpha(\mathbf{x})\, d\mathbf{x} \tag{3.10}$$

The components of motions are calculated through those minors J_n [82]. This tensor is calculated by means of the n^{th} space-time derivatives of the image $\mathbf{l}(\mathbf{x}) = L(\mathbf{x}) * \partial^{\alpha} g(\mathbf{x})$, where g is a kernel function, α denotes a multi-index and $\alpha(\mathbf{x})$ is a weight.

The optical flow constrain equation has a single equation for two unknowns, which is an undetermined system [68]. This is what the aperture problem is about. For a limited aperture size and an edge structure, movement along the normal of an edge can only be estimated, which is denoted here by $\nabla_{xy} L / \|\nabla_{xy} L\|$. The normal flow is defined by $\mathbf{u} / \|\mathbf{u}\| = \nabla_{xy} L / \|\nabla_{xy} L\|$. If we use the optical flow constrain equation, the speed of this normal flow is:

$$s = -\frac{L_t}{\|\nabla_{xy} L\|} \tag{3.11}$$

The other constrains are intended to provide alternatives to the descriptions of the optical flow constrain equation. Most of them also aim to overcome the ambiguity of that equation and make additional assumptions. The Bayesian constraint uses a movement before resolving ambiguity. The sampling conditions assume a constant optical flow within the neighborhoods from which the samples are taken. In this way, these conditions provide additional constraint equations to solve and obtain a velocity vector. The rigorous condition assumes that all terms of Taylor's series expansion of L and $\mathbf{w}$ are evaluated to zero independently.

The Fourier transform of the entire sequence of an image results in energy in a plane whose orientation is determined by movement. If the entire image is composed of a moving edge, the energy is concentrated around a single line, which in turn results in an ambiguous 2D motion vector. If the image sequence contains several moving objects, then the energy exists in multiple planes. Another constraint calculates the spatial partial derivatives of the optical flow equation, which produces two equations due to the two spatial dimensions. This also resolves the ambiguity. Another option is to determine the Hessian matrix and thus obtain the partial second-order derivatives of the multi-dimensional function.

There are methods where the optical flow equation is involved from a probabilistic point of view [83]. These methods, known as Bayesian constraint, assume that the deviations from the optical flow equation lead us to a normal distribution:

$$P(f(\mathbf{z}) | \mathbf{u}(\mathbf{z})) = \frac{1}{\sqrt{2\pi\sigma^2}} \exp\left(-\frac{1}{2\sigma^2} \int_{\Omega_{\mathbf{z}}} \left(\nabla_{xyt} L(\mathbf{z}') \begin{pmatrix} \mathbf{u} \\ 1 \end{pmatrix} \right)^2 d\mathbf{z}' \right) \tag{3.12}$$

Using the posterior probability $P(\mathbf{u}(\mathbf{z}))$ for the movement and the probability for a certain gray-value:

$$P\left(\mathbf{u}\left(\mathbf{z}\right)|L\left(\mathbf{z}\right)\right)=\frac{P\left(L\left(\mathbf{z}\right)|\mathbf{u}\left(\mathbf{z}\right)\right)P\left(\mathbf{u}\left(\mathbf{z}\right)\right)}{P\left(L\left(\mathbf{z}\right)\right)} \tag{3.13}$$

Another scheme to solve the aperture problem is to integrate over a large region within the image, hoping that it could contain corners in addition to the edges. If a Taylor series expansion of L is used, of order m and for the movement vector $\mathbf{v}=(u,v,1)$ of order n in the argument of $\mathbf{z}=(x,y,t)^t$ and this is placed in the optical flow equation, the polynomial equation is obtained:

$$\sum_{0\leq|\alpha|\leq n}\sum_{0\leq|\beta|\leq m}\frac{1}{\alpha!\beta!}\partial^{1+\alpha}L\left(\mathbf{z}\right)\partial^{\beta}\mathbf{v}\left(\mathbf{z}\right)(\partial\mathbf{z})^{\alpha+\beta}=0 \tag{3.14}$$

where α and β are the so-called multi-indexes. A simplification of the polynomial equation in (3.14), gives us another way to solve the optical flow:

$$\sum_{|\alpha|+|\beta|=r}\frac{1}{\alpha!\beta!}\partial^{1+\alpha}L\left(\mathbf{z}\right)\partial^{\beta}\mathbf{v}\left(\mathbf{z}\right)=0 \tag{3.15}$$

Another way to use the optical flow equation is to transform it to the Fourier domain:

$$\omega=\mathbf{k}^t\mathbf{u} \tag{3.16}$$

The movement, observed in the Fourier domain, constraints the spectral power to the plane given by Eq. (3.16), where $k=(k_xk_y)^t$ denotes the angular frequencies, which correspond to spatial coordinates (x,y) and ω denotes the angular frequency associated with time t [18, 84].

To deal with the indeterminate system of the optical flow equation we can use another input for the equation. In [14], the authors assume that a quantity g of the continuity equation can be expressed by the spatial derivatives of the gray-scale function determined by the image, that is, $g=\nabla_{xy}L$. Additionally, assuming, $\nabla_{xy}\mathbf{u}=0$, the "Hessian" constraint can be derived:

$$\nabla\partial_tL+H_L\mathbf{u}=0 \tag{3.17}$$

Its name is because of H_L is the Hessian matrix of the function that represents the gray-scale image concerning spatial components (x,y).

Another way of using the input of the optical flow equation is through the local phase ϕ, which can be calculated, for example, by means of Gabor filters [85]. Therefore $h=\phi$. Given the above, we obtain the constraint:

$$\left(\nabla_{xyt}\phi\right)^t\left(\dot{x},\dot{y},1\right)=0 \tag{3.18}$$

3.5 Regularization for Optical Flow Estimation

Another methodology to solve the aperture problem is to add regularization constraints. This can be done by minimizing a functional given by:

$$\min_{x,y} \int_{\Omega} \Big(\psi_1 \left(\partial_x L \cdot u + \partial_y L \cdot v + \partial_t L \right) + \psi_2 \left(L, u, v \right) \Big) d\mathbf{x} \tag{3.19}$$

where the solution is restricted to the second regularization term of Eq. (3.19), which penalizes the variations of the optical flow. The functions ψ_1 and ψ_2 are robust estimators for the term of the data and the term of the regularization respectively and Ω denotes an area of 2D integration usually given by the plane of the same image.

To solve the Eq. (3.19), the generalized method is to calculate the equation of Euler-Lagrange and then discretize the partial differential equation to be able to find a numerical solution. The functions ψ_1 will characterize the smoothness of the solutions [86, 87]. The term ψ_2 is general and is related to grayscale function information and optical flow. Some of them are described below:

Homogeneous regularizer. This regularizer is defined by:

$$\min_{u,v} \int_{\Omega} \left(\|\nabla u\|^2 + \|\nabla v\|^2 \right) d\mathbf{x} \tag{3.20}$$

which was introduced by [11]. The partial derivatives of each flow component must be small. In [87], called this homogeneous restriction because the smoothing is global and equally spaced. Combining with the optical flow equation, a solution can be obtained using variational calculation.

Isotropic regulator through the image. This regulator uses the square of the magnitude of the image gradient to control smoothing [88]:

$$\min_{u,v} \int_{\Omega} \left(\psi \left(\|\nabla_{xy} L\|^2 \right) \cdot \left(\|\nabla u\|^2 + \|\nabla v\|^2 \right) \right) d\mathbf{x} \tag{3.21}$$

$$\text{with: } \psi \left(s^2 \right) = \frac{1}{\sqrt{1 + \frac{s^2}{\eta^2}}}$$

where η denotes a parameter that controls the smoothness. For a large gradient of the image, such as a border, the smoothing of the flow is reduced. In Eq. (3.21) it is impossible to smooth the edges, for homogeneous surfaces, where the gradients of the image are small, the smoothness is carried out in a better way.

Anisotropic regulator through the image. This regulator integrates the direction and the magnitude provided by the information of the grayscale image [87]. Smoothing

only appears along the edge and not through it. Also, it is attenuated in the presence of an edge and unattended into homogeneous regions. With this in mind [7] proposed:

$$\min_{u,v} \int_{\Omega} \Big((\nabla u)\, S_{NE} (\nabla u)^t + (\nabla v)\, S_{NE} (\nabla v)^t \Big) d\mathbf{x} \tag{3.22}$$

with

$$S_{NE} = \frac{1}{\|\nabla_{xy}\|^2 + k^2} \begin{bmatrix} (\partial_y L)^2 + k^2 & -(\partial_x L)(\partial_y L) \\ -(\partial_x L)(\partial_y L) & (\partial_x L)^2 + k^2 \end{bmatrix} \tag{3.23}$$

where k is a parameter that controls the smoothness.

Isotropic regulator through flow. This approximation uses a robust estimator for the square of the magnitudes of each derivative and the flow components as an argument.

$$\min_{u,v} \int_{\Omega} \psi_S \left(\|\nabla u\|^2 + \|\nabla v\|^2 \right) d\mathbf{x} \tag{3.24}$$

$$\text{with } \psi\left(s^2\right) = \sqrt{s^2 + \lambda^2}$$

λ is a parameter that controls smoothing. The function is used in [87], however many other similar functions have been proposed in [89, 90, 91, 92].

Anisotropic regulator through flow. Unlike the anisotropic case through image, which includes information about the magnitude of the flow only. This regulator includes information about the flow direction. In [86], the following restriction was proposed:

$$\min_{u,v} \int_{\Omega} \mathrm{tr} \Big\{ \psi_s \left((\nabla u)^t (\nabla u) + (\nabla v)^t (\nabla v) \right) \Big\} d\mathbf{x} \tag{3.25}$$

$$\text{with } \psi_s\left(s^2\right) = \sqrt{s^2 + \lambda^2}$$

Here λ also controls the smoothing. ψ_s it is the robustness function that is applied to each input, the operator $\mathrm{tr}\{\}$ is the trace of the matrix. Several authors propose using the divergence and rotational of the vector field $\mathbf{u} = (u, v)$ as a regularizer:

$$\min_{u,v} \int_{\Omega} \psi_{DC} \Big(\mathrm{div}\left(\mathbf{u}\right), \mathrm{rot}\left(\mathbf{u}\right) \Big) d\mathbf{x} \tag{3.26}$$

with ψ_{DC} as a generic robust function.

Most contours are formed by rigid objects in the scene, which move locally consistently. This observation can be used to define a contour-based smoothing:

$$\int_C \left\| \frac{\partial \mathbf{u}_n(s)}{\partial s} \right\| ds = 0 \tag{3.27}$$

with $\mathbf{u}_n(s)$ as a normal flow along the contour C [12], where s is a parameter of the curve. This integral calculates the curvature of each flow component along the curve, which is minimized in combination with the input data to determine the normal flow.

3.6 Differential Methods

It is convenient to describe the two most important methods that exist in the literature because our proposal is based on differential methods.

Differential techniques calculate the speed of the image from time-space derivatives of the intensities of the images. Therefore, the assumption is made that the image is continuous or differentiable in space and time. There are global and local methods of first and second-order, all based on the optical flow constraint (Eq. 3.8). The global methods use that equation and some additional global constraint, usually a smoothing regularization term to calculate the optical flow density over large regions of the image. Local methods usually use the normal velocity information in local neighborhoods to perform a least-squares approximation to find the best fit for $\mathbf{w}$. The size of the neighborhoods to obtain an estimate of the flow is determined by each technique, either local or global [6].

3.7 Lucas-Kanade in 2D

In 1981, Lucas and Kanade [13] proposed a local differential method defined by:

$$\begin{bmatrix} \frac{\partial^2 L}{\partial x^2} & \frac{\partial^2 L}{\partial x \partial y} \\ \frac{\partial^2 L}{\partial x \partial y} & \frac{\partial^2 L}{\partial y^2} \end{bmatrix} \begin{bmatrix} u \\ v \end{bmatrix} = -\frac{\partial \left(\vec{\nabla} \mathrm{L}\right)}{\partial \mathrm{t}} \tag{3.28}$$

Considering a neighborhood environment Ω around each point on which the summation extends, Eq. (3.28) can be expressed as follows:

$$\begin{bmatrix} \sum_\Omega L_x^2 & \sum_\Omega L_x L_y \\ \sum_\Omega L_x L_y & \sum_\Omega L_y^2 \end{bmatrix} \begin{bmatrix} u \\ v \end{bmatrix} = -\begin{bmatrix} \sum_\Omega L_t L_x \\ \sum_\Omega L_t L_y \end{bmatrix} \equiv \mathbf{A}\mathbf{w} = \mathbf{b} \tag{3.29}$$

Whose solution can be established like this:

$$\mathbf{w} = (\mathbf{A}^T \mathbf{A})^{-1} \mathbf{A}^T \mathbf{b} \tag{3.30}$$

Following the algorithm implemented with least-squares adjustment to first-order constraints (Eq. 3.8), for a constant model of $\mathbf{w}$ in each spatial neighborhood (Ω), and minimizing we get:

$$\sum_{x,y \in \Omega} W^2(x,y) \left[\nabla L(x,y,t) \cdot \mathbf{w} + L_t(x,y,t)\right]^2 \tag{3.31}$$

where $W(x,y)$ denotes a window function that gives more influence to the constraints in the center of the neighborhood than in the periphery. They are typically Gaussian coefficients. The solution of Eq. (3.31) is given by:

$$\mathbf{w} = (\mathbf{A}^T \mathbf{W}^\mathbf{2} \mathbf{A})^{-\mathbf{1}} \mathbf{A}^T \mathbf{W}^\mathbf{2} \mathbf{b} \tag{3.32}$$

Where, for N pixels (for $n \times n$ neighbors $N = n^2$), $(x_i, y_i) \in \Omega$ at each time t:

$$\begin{aligned} \mathbf{A} &= \left[\nabla L\left(x_1, y_1\right), \ldots, \nabla L\left(x_N, y_N\right)\right], \\ W &= \operatorname{diag}\left[W\left(x_1, y_1\right), \ldots, W\left(x_N, y_N\right)\right], \\ \mathbf{b} &= -\left(L_t\left(x_1, y_1\right), \ldots, L_t\left(x_N, y_N\right)\right) \end{aligned} \tag{3.33}$$

In Appendix C, we can see a step-by-step example of this method for two synthetic forms, whose results is shown in the Figure 3.5:

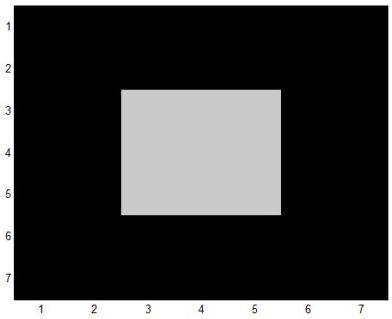

(a) ***Synthetic rectangle 1***

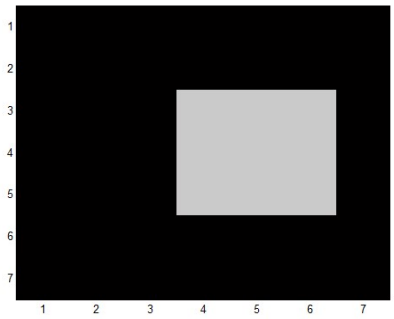

(b) ***Synthetic rectangle 2***

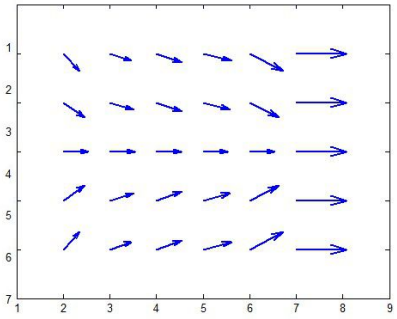

(c) ***Optical Flow***

Figure 3.5: Synthetic forms and Optical Flow for the Lucas and Kanade algorithm in 2D.

3.8 Lucas-Kanade in 3D

Using the equation of movement in 3D:

$$L_x u + L_y v + L_z w = -L_t \tag{3.34}$$

where L_x, L_y and L_z are the derivatives of intensity in 3D, in a neighborhood of $n \times n \times n$, centered on the voxel (x, y, z), we assume a constant velocity u, v and w in the region and minimizing:

$$\sum_{x,y,z \in \Omega} W^2(x,y,z) \left[\nabla L(x,y,z,t) \cdot \mathbf{w} + L_t(x,y,z,t)\right]^2 \tag{3.35}$$

where $W(x,y,z)$ denotes a Gaussian windowing function. Eq. (3.35) can be solved by means of the same expression than in Eq. (3.32) and the following system of equations:

$$\begin{aligned} \mathbf{A} &= \left[\nabla L(x_1,y_1,z_1), \ldots, \nabla L(x_N,y_N,z_N)\right], \\ \mathbf{W} &= \operatorname{diag}\left[W(x_1,y_1,z_1), \ldots, W(x_N,y_N,z_N)\right], \\ \mathbf{b} &= -\left(L_t(x_1,y_1,z_1), \ldots, L_t(x_N,y_N,z_N)\right) \end{aligned} \tag{3.36}$$

$\mathbf{A}^T\mathbf{W}^2\mathbf{A}$ it is calculated like this:

$$\mathbf{A}^{\mathrm{T}}\mathbf{W}^2\mathbf{A} = \begin{bmatrix} \sum W^2(x,y,z) L_x^2(x,y,z) & \sum W^2(x,y,z) L_x(x,y,z) L_y(x,y,z) & \sum W^2(x,y,z) L_x(x,y,z) L_z(x,y,z) \\ \sum W^2(x,y,z) L_y(x,y,z) L_x(x,y,z) & \sum W^2(x,y,z) L_y^2(x,y,z) & \sum W^2(x,y,z) L_y(x,y,z) L_z(x,y,z) \\ \sum W^2(x,y,z) L_z(x,y,z) L_x(x,y,z) & \sum W^2(x,y,z) L_z(x,y,z) L_y(x,y,z) & \sum W^2(x,y,z) L_z^2(x,y,z) \end{bmatrix} \tag{3.37}$$

3.9 Horn and Schunck in 2D

Following, we show the Horn and Schunck method [11], which combined the optical flow constraint (Eq. 3.8), with a global smoothing term to restrict the estimated velocity field. Thus, the energy functional to be minimized is given by:

$$\int_D \left\{ (\nabla \mathbf{L} \cdot \mathbf{w} + L_t)^2 + \alpha^2 \left[\left(\frac{\partial u}{\partial x}\right)^2 + \left(\frac{\partial u}{\partial y}\right)^2 + \left(\frac{\partial v}{\partial x}\right)^2 + \left(\frac{\partial v}{\partial y}\right)^2 \right] \right\} dxdy \tag{3.38}$$

it is defined on a domain D (the image), where the magnitude of α, reflects the relative influence of the smoothing term. A value of $\alpha = 10$ is recommended [11], but the value depends on the application in question. The iterative equations are used to minimize the Eq. (3.38) and the velocity of the image can be obtained from the Gauss-Seidel equations that appropriately solve the Euler-Lagrange equations:

$$\begin{aligned} u^{k+1} &= \overline{u}^k - \frac{L_x\left[L_x\overline{u}^k + L_y\overline{v}^k + L_t\right]}{\alpha^2 + L_x^2 + L_y^2}, \\ v^{k+1} &= \overline{v}^k - \frac{L_y\left[L_x\overline{u}^k + L_y\overline{v}^k + L_t\right]}{\alpha^2 + L_x^2 + L_y^2}, \end{aligned} \tag{3.39}$$

where k denotes the iteration number, u^0 and v^0 denote the initial velocity that is typically selected to zero but may come from an earlier iteration even from some other algorithm. $\overline{u}^k$

and $\overline{v}^k$ denote the averages of the neighbors of u^k and v^k. A typical number of iterations is set to 100, but we can determine some criteria to automatically stop the iterations. For example, let $\mathbf{w}_{2DOF}$ be a vector of $N \times M \times 2$ constructed from the vectors calculated for the optical flow of size $N \times M$ for an image of size $N \times M$, whose components are the consecutive components of the velocity in 2D. A test to stop iterations is when the optical flow field converge [93], i.e. when:

$$\left\| \mathbf{w}_{2DOF}^{k} - \mathbf{w}_{2DOF}^{k-1} \right\|^2 \leq TOL \tag{3.40}$$

for k iterations, where TOL is some tolerance level previously selected. On the other hand, if the size of the consecutive flows increases, it means that the procedure diverges.

3.10 Horn and Schunck in 3D

If we extend the Horn and Schunck energy functional (Eq. 3.38) to 3D, we should minimize:

$$\begin{aligned} &\sum_R \left(L_x u + L_y v + L_z w + L_t\right) + \alpha^2 \left[\left(\tfrac{\partial u}{\partial x}\right)^2 + \left(\tfrac{\partial u}{\partial y}\right)^2 + \left(\tfrac{\partial u}{\partial z}\right)^2 + \right. \\ &\left. + \left(\tfrac{\partial v}{\partial x}\right)^2 + \left(\tfrac{\partial v}{\partial y}\right)^2 + \left(\tfrac{\partial v}{\partial z}\right)^2 + \left(\tfrac{\partial w}{\partial x}\right)^2 + \left(\tfrac{\partial w}{\partial y}\right)^2 + \left(\tfrac{\partial w}{\partial z}\right)^2 \right] \end{aligned} \tag{3.41}$$

Thus, the Gauss-Seidel equations that minimize the expression are given by:

$$\begin{aligned} u^{k+1} &= \overline{u}^k - \tfrac{L_x\left[L_x\overline{u}^k + L_y\overline{v}^k + L_z\overline{w}^k + L_t\right]}{\alpha^2 + L_x^2 + L_y^2 + L_z^2}, \\ v^{k+1} &= \overline{v}^k - \tfrac{L_y\left[L_x\overline{u}^k + L_y\overline{v}^k + L_z\overline{w}^k + L_t\right]}{\alpha^2 + L_x^2 + L_y^2 + L_z^2}, \\ w^{k+1} &= \overline{w}^k - \tfrac{L_z\left[L_x\overline{u}^k + L_y\overline{v}^k + L_z\overline{w}^k + L_t\right]}{\alpha^2 + L_x^2 + L_y^2 + L_z^2} \end{aligned} \tag{3.42}$$

where $\overline{u}^k$, $\overline{v}^k$ and $\overline{w}^k$ are vicinity velocities of size $n \times n \times n$ in the iteration k.

Chapter 4

3D Optical Flow Using The Hermite Transform

4.1 Optical Flow using the Hermite Transform

In this chapter, we present a modified version of the Horn and Schunck method [11]. It uses the Hermite transform as a biological visual model to avoid the main disadvantage of the Horn and Schunck proposal, i.e, its low accuracy. In this sense, the local constraints found in the Horn and Schunck approach are defined using the zero-order and steered Hermite coefficients and as local descriptors of visual features of the volumes.

4.1.1 Model

The modified and multiresolution version of Horn and Schunck approach that allows increasing the accuracy of the optical flow is based on the work of Sun et al. [20]. It uses the Hermite transform, that involves an expansion of the Constant Intensity Constraint, with the incorporation of the Steered Hermite Coefficient Constraint of the Hermite Transform, is defined as follows:

$$\left[L_0\left(\mathbf{x}+\mathbf{w}\right)-L_0\left(\mathbf{x}\right)\right]+\gamma\left[\sum_{n=1}^{N} l_{n,\theta,\phi}\left(\mathbf{x}+\mathbf{w}\right)-\sum_{n=1}^{N} l_{n,\theta,\phi}\left(\mathbf{x}\right)\right]=0 \tag{4.1}$$

where $L\left(\mathbf{x}\right)$ is a volume sequence, with $\mathbf{x}=\left(x,y,z,t\right)^T$ representing the voxel location within a cubic volume domain V; $\mathbf{w}:=\left(u,v,w,1\right)^T$ is a vector that defines the displacement u, v and w of each a voxel at position (x,y,z) within the sequence of volumes at a time t to a time $(t+1)$ in the directions x, y and z respectively; and γ is a weight parameter.

Therefore, the energy functional using the Hermite transform can be expressed as:

$$\mathrm{E} = \int_V \left(\left[L_0(\mathbf{x})_0 - L_0(\mathbf{x}+\mathbf{w}+d\mathbf{w})_1 \right]^2 + \gamma \left[\sum_{n=1}^{N} \left\{ l_{n,\theta,\phi}(\mathbf{x})_0 - l_{n,\theta,\phi}(\mathbf{x}+\mathbf{w}+d\mathbf{w})_1 \right\} \right]^2 + \alpha |\nabla(\mathbf{w}+d\mathbf{w})|^2 \right) d\mathbf{x} \tag{4.2}$$

To simplify the notation $L_{000}(\mathbf{x}) = L_0(\mathbf{x})$, $L_*(\mathbf{x})_*$ is the Cartesian Hermite coefficient $*$ at time t, and $L_*(\mathbf{x})_1$ is the Cartesian Hermite coefficient $*$ at time $t+1$.

Considering linear displacements in Eq. (4.1) and performing an expansion by Taylor series we obtain:

$$L_0(\mathbf{x})_0 - L_0(\mathbf{x}+\mathbf{w}+d\mathbf{w})_1 \approx L_0(\mathbf{x})_0 - L_0(\mathbf{x}+\mathbf{w})_1 - du\frac{\partial L_0(\mathbf{x}+\mathbf{w})_1}{\partial x} - dv\frac{\partial L_0(\mathbf{x}+\mathbf{w})_1}{\partial y} - dw\frac{\partial L_0(\mathbf{x}+\mathbf{w})_1}{\partial z} \tag{4.3}$$

In the 1D case, the Hermite coefficients are achieved by the inner product between the signal located by the Gaussian window and the Hermite polynomials, so the one-dimensional spatial derivatives can be reduced:

$$L_k = \left\langle L(x), H_k\left(\frac{x}{\sigma}\right) \right\rangle \tag{4.4}$$

In [29] was demonstrated, that the spatial derivatives of the Hermite coefficients, can be expressed as:

$$L_k = \frac{\partial^k L(x)}{\partial^k x} \tag{4.5}$$

Thereby, an expression with a partial derivative of the Hermite coefficients, in the spatial coordinates, can be reduced using a higher-order Hermite coefficient of the corresponding variable. For example, we can replace the following derivatives of x of the Hermite coefficients with themselves, but increasing its corresponding order index:

$$L_{100}(\mathbf{x}+\mathbf{w}) = L_{100}(\mathbf{x})_{\mathbf{w}} = \frac{\partial L_{000}(\mathbf{x}+\mathbf{w})_1}{\partial x} \tag{4.6}$$

$$l_{n,\theta,\phi,(m+1)}(\mathbf{x})_{\mathbf{w}} = \frac{\partial l_{n,\theta,\phi}(\mathbf{x}+\mathbf{w})_1}{\partial x} \tag{4.7}$$

On the other hand, the temporal derivatives can be approximated using the following relations:

$$L_0(\mathbf{x})_t = L_0(\mathbf{x}+\mathbf{w})_1 - L_0(\mathbf{x})_0 \tag{4.8}$$

$$l_{n,\theta,\phi}(\mathbf{x})_t = l_{n,\theta,\phi}(\mathbf{x})_1 - l_{n,\theta,\phi}(\mathbf{x}+\mathbf{w})_0 \tag{4.9}$$

Thus, using Eq. (4.5) and the temporal-derivative approximation shown in Eq. (4.8) and Eq. (4.9), we can rewrite Eq. (4.3) as follows:

$$L_0(\mathbf{x})_0 - L_0(\mathbf{x}+\mathbf{w}+d\mathbf{w})_1 \approx -\left[L_0(\mathbf{x})_t + du L_{100}(\mathbf{x})_{\mathbf{w}} + dv L_{010}(\mathbf{x})_{\mathbf{w}} + dw L_{001}(\mathbf{x})_{\mathbf{w}} \right] \tag{4.10}$$

Replacing Eq. 4.10 in Eq. 4.2 we can define the Horn-Hermite optical flow in 3D (HOF3D), obtaining:

$$\begin{aligned} E(\mathbf{w}) = \int_V \Big(& -[L_0(\mathbf{x})_t + du L_{100}(\mathbf{x})_{\mathbf{w}} + dv L_{010}(\mathbf{x})_{\mathbf{w}} + dw L_{001}(\mathbf{x})_{\mathbf{w}}]^2 \\ & - \gamma \sum_{n=1}^{N} \left[l_{n,\theta,\phi}(\mathbf{x})_t + du\, l_{n,\theta,\phi,(m+1)}(\mathbf{x})_{\mathbf{w}} + dv\, l_{n,\theta,\phi,(n+1)}(\mathbf{x})_{\mathbf{w}} + dw\, l_{n,\theta,\phi,(l+1)}(\mathbf{x})_{\mathbf{w}} \right]^2 \\ & + \alpha |\nabla(\mathbf{w} + d\mathbf{w})|^2 \Big)\, d\mathbf{x} \end{aligned} \tag{4.11}$$

Next, we can minimize Eq. (4.11) for u, v and w obtaining the following system of equations:

$$\begin{aligned} \frac{\partial E(\mathbf{w})}{\partial du} = & -2 \left(L_0(\mathbf{x})_t + du L_{100}(\mathbf{x})_{\mathbf{w}} + dv L_{010}(\mathbf{x})_{\mathbf{w}} + dw L_{001}(\mathbf{x})_{\mathbf{w}} \right) L_{100}(\mathbf{x})_{\mathbf{w}} \\ & - 2\gamma \sum_{n=1}^{N} \left(l_{n,\theta,\phi}(\mathbf{x})_t + du\, l_{n,\theta,\phi,(m+1)}(\mathbf{x})_{\mathbf{w}} + dv\, l_{n,\theta,\phi,(n+1)}(\mathbf{x})_{\mathbf{w}} + dw\, l_{n,\theta,\phi,(l+1)}(\mathbf{x})_{\mathbf{w}} \right) l_{n,\theta,\phi,(m+1)}(\mathbf{x})_{\mathbf{w}} \\ & + 2\alpha |\nabla(u + du)| \end{aligned} \tag{4.12}$$

$$\begin{aligned} \frac{\partial E(\mathbf{w})}{\partial dv} = & -2 \left(L_0(\mathbf{x})_t + du L_{100}(\mathbf{x})_{\mathbf{w}} + dv L_{010}(\mathbf{x})_{\mathbf{w}} + dw L_{001}(\mathbf{x})_{\mathbf{w}} \right) L_{010}(\mathbf{x})_{\mathbf{w}} \\ & - 2\gamma \sum_{n=1}^{N} \left(l_{n,\theta,\phi}(\mathbf{x})_t + du\, l_{n,\theta,\phi,(m+1)}(\mathbf{x})_{\mathbf{w}} + dv\, l_{n,\theta,\phi,(n+1)}(\mathbf{x})_{\mathbf{w}} + dw\, l_{n,\theta,\phi,(l+1)}(\mathbf{x})_{\mathbf{w}} \right) l_{n,\theta,\phi,(n+1)}(\mathbf{x})_{\mathbf{w}} \\ & + 2\alpha |\nabla(v + dv)| \end{aligned} \tag{4.13}$$

$$\begin{aligned} \frac{\partial E(\mathbf{w})}{\partial dw} = & -2 \left(L_0(\mathbf{x})_t + du L_{100}(\mathbf{x})_{\mathbf{w}} + dv L_{010}(\mathbf{x})_{\mathbf{w}} + dw L_{001}(\mathbf{x})_{\mathbf{w}} \right) L_{001}(\mathbf{x})_{\mathbf{w}} \\ & - 2\gamma \sum_{n=1}^{N} \left(l_{n,\theta,\phi}(\mathbf{x})_t + du\, l_{n,\theta,\phi,(m+1)}(\mathbf{x})_{\mathbf{w}} + dv\, l_{n,\theta,\phi,(n+1)}(\mathbf{x})_{\mathbf{w}} + dw\, l_{n,\theta,\phi,(l+1)}(\mathbf{x})_{\mathbf{w}} \right) l_{n,\theta,\phi,(l+1)}(\mathbf{x})_{\mathbf{w}} \\ & + 2\alpha |\nabla(w + dw)| \end{aligned} \tag{4.14}$$

Rewriting the equation system of Equations (4.12, 4.13, 4.14) in matrix form:

$$\begin{bmatrix} A_1 & A_2 & A_3 \\ A_4 & A_5 & A_6 \\ A_7 & A_8 & A_9 \end{bmatrix} \begin{bmatrix} du \\ dv \\ dw \end{bmatrix} = \begin{bmatrix} b_1 \\ b_2 \\ b_3 \end{bmatrix} \tag{4.15}$$

where from Eq. (4.12):

$$A_1 = L^2_{100}(\mathbf{x})_{\mathbf{w}} + \gamma \sum_{n=1}^{N} l^2_{n,\theta,\phi,(m+1)}(\mathbf{x})_{\mathbf{w}}$$

$$A_2 = L_{100}(\mathbf{x})_{\mathbf{w}} L_{010}(\mathbf{x})_{\mathbf{w}} + \gamma \sum_{n=1}^{N} l_{n,\theta,\phi,(m+1)}(\mathbf{x})_{\mathbf{w}} \cdot l_{n,\theta,\phi,(n+1)}(\mathbf{x})_{\mathbf{w}}$$

$$A_3 = L_{100}(\mathbf{x})_{\mathbf{w}} L_{001}(\mathbf{x})_{\mathbf{w}} + \gamma \sum_{n=1}^{N} l_{n,\theta,\phi,(n+1)}(\mathbf{x})_{\mathbf{w}} \cdot l_{n,\theta,\phi,(l+1)}(\mathbf{x})_{\mathbf{w}}$$

$$b_1 = L_0(\mathbf{x})_t L_{100}(\mathbf{x})_{\mathbf{w}} + \gamma \sum_{n=1}^{N} l_{n,\theta,\phi}(\mathbf{x})_t \cdot l_{n,\theta,\phi,(m+1)}(\mathbf{x})_{\mathbf{w}} - \alpha \left|\nabla (u + du)\right|$$

and from Eq.(4.13):

$$A_4 = L_{010}(\mathbf{x})_{\mathbf{w}} L_{100}(\mathbf{x})_{\mathbf{w}} + \gamma \sum_{n=1}^{N} l_{n,\theta,\phi,(n+1)}(\mathbf{x})_{\mathbf{w}} \cdot l_{n,\theta,\phi,(m+1)}(\mathbf{x})_{\mathbf{w}}$$

$$A_5 = L^2_{010}(\mathbf{x})_{\mathbf{w}} + \gamma \sum_{n=1}^{N} l^2_{n,\theta,\phi,(n+1)}(\mathbf{x})_{\mathbf{w}}$$

$$A_6 = L_{010}(\mathbf{x})_{\mathbf{w}} L_{001}(\mathbf{x})_{\mathbf{w}} + \gamma \sum_{n=1}^{N} l_{n,\theta,\phi,(m+1)}(\mathbf{x})_{\mathbf{w}} \cdot l_{n,\theta,\phi,(l+1)}(\mathbf{x})_{\mathbf{w}}$$

$$b_2 = L_0(\mathbf{x})_t L_{010}(\mathbf{x})_{\mathbf{w}} + \gamma \sum_{n=1}^{N} l_{n,\theta,\phi}(\mathbf{x})_t \cdot l_{n,\theta,\phi,(n+1)}(\mathbf{x})_{\mathbf{w}} - \alpha \left|\nabla (v + dv)\right|$$

and from Eq.(4.14):

$$A_7 = L_{001}(\mathbf{x})_{\mathbf{w}} L_{100}(\mathbf{x})_{\mathbf{w}} + \gamma \sum_{n=1}^{N} l_{n,\theta,\phi,(l+1)}(\mathbf{x})_{\mathbf{w}} \cdot l_{n,\theta,\phi,(m+1)}(\mathbf{x})_{\mathbf{w}}$$

$$A_8 = L_{001}(\mathbf{x})_{\mathbf{w}} L_{010}(\mathbf{x})_{\mathbf{w}} + \gamma \sum_{n=1}^{N} l_{n,\theta,\phi,(l+1)}(\mathbf{x})_{\mathbf{w}} \cdot l_{n,\theta,\phi,(n+1)}(\mathbf{x})_{\mathbf{w}}$$

$$A_9 = L^2_{001}(\mathbf{x})_{\mathbf{w}} + \gamma \sum_{n=1}^{N} l^2_{n,\theta,\phi,(l+1)}(\mathbf{x})_{\mathbf{w}}$$

$$b_3 = L_0(\mathbf{x})_t L_{001}(\mathbf{x})_{\mathbf{w}} + \gamma \sum_{n=1}^{N} l_{n,\theta,\phi}(\mathbf{x})_t \cdot l_{n,\theta,\phi,(l+1)}(\mathbf{x})_{\mathbf{w}} - \alpha \left|\nabla (w + dw)\right|$$

Finally, the functional of Eq. (4.11) was implemented within a multiresolution approach to calculate the small displacements du, dv, dw and to update $\mathbf{w}$, then the solution is propagated to higher resolution levels. For each resolution level, an iterative method for solving linear equations was carried out.

Chapter 5

Experiments and Results

In this chapter, we present the results of the estimation of the optical flow with the proposed method. Dozens of cardiac volumes corresponding to medical CT images were used for this purpose. In general, the Chapter is divided into three stages, a validation stage for two-dimensional images, a validation stage for three-dimensional volumes, and a stage of 3D optical flow results of the cardiac volumes and their left ventricle. In the first stage, the optical flow results, using the 2D implementation of our proposal, were compared with a set of images ground-truth and a pair of algorithms of optical flow. In the second stage, we performed a validation of our approach in 3D, where the optimal parameters both in the Hermite transform and the 3D optical flow proposal were determined. The optical flow results in 3D were compared with the modified and multiresolution method of Horn and Schunck [20]. Next, an analysis of robustness to noise was performed. In the third stage, the 3D optical flow results of our method in the left ventricle, which was previously segmented, are shown and the corresponding errors of interpolation are evaluated.

The results obtained on a PC Intel(R) Core(TM) i7-4710HQ CPU running at 2.50 GHz with 16 GB of RAM have an algorithm time-consuming of 4.8 h on 4 cores, nevertheless, this can be reduced to an average of 4.5 min with parallel computing and additional cores. The optical flow in our method has good scalability, close to linear speedup, which allows us to significantly reduce processing time. The results concerning processing time are consistent with those reported in [94]. They tested two differential algorithms, Lucas-Kanade and Horn-Schunck in $3D + t$, as we have also done.

5.1 Description of the Proposed Method

The present work is an extension of our previous papers published in [54] and [55] (Appendix D). In [54], we proposed the three-dimensional optical flow estimation using the 3D steered Hermite transform and we compared our approach with the 3D Horn-Schunck method. In [55], we compared our proposal with a multiresolution Horn and Schunck approach reported

by Sun et al. [20], moreover, we perform a depth analysis about the optimal parameters of the method proposed and we focused the Section 5.8 to analyzed the 3D optical flow estimation of the left ventricle. First, we show its 3D segmentation and the advantages of our approach compared with the 3D version of the method of Sun et al. [20]. Then, we show the 3D motion of the left ventricle in the different cardiac cycle and a whole cardiac cycle, highlighting the corresponding contraction and relaxation movements present in each phase of the cardiac cycle. It should be mentioned that similar 2D algorithms using the Hermite transform have already been presented in [29, 33] but with the main disadvantage of consuming a lot of computing time.

Figure 5.1 shows an overview of the proposed method according to the method explained in Chapter 4 and the next sections.

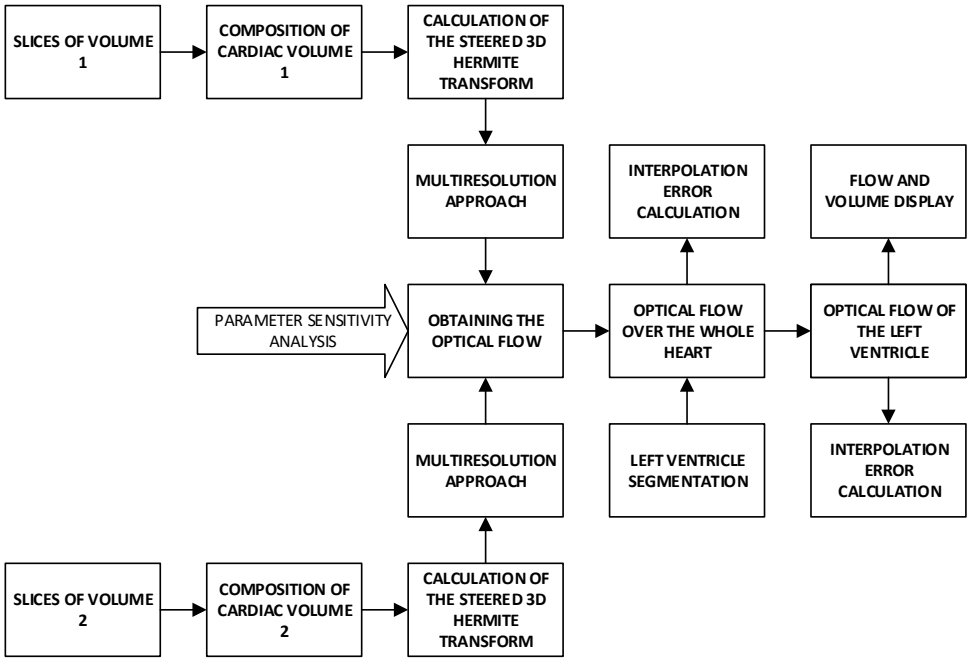

Figure 5.1: Overview of the proposed method.

5.2 2D Optical Flow Validation

In this section, we present the performance of our multiresolution 2D Horn-Hermite optical flow approach (HOF2D) to have common comparison elements with similar algorithms, through metrics and a known workbench [95].

5.2.1 2D Angular Errors

Because we do not have a set of 3D optical flow to compare our results, we evaluate the performance of our 2D proposal, through a collection of well-known images. These images and their respective ground-truth optical flows can be found through [95], which still have great use and relevance today. They defined sequences with non-rigid movements where the optical flow was determined following a hidden fluorescent texture.

As a performance measure, we calculate the angular error (AE) proposed in [6]. The angular error between a flow vector (u, v) and a ground-truth reference flow (u_{GT}, v_{GT}) can be calculated by taking the scalar product of the vectors, dividing by the product of their magnitudes and then taking the inverse of cosine:

$$AE = \cos^{-1}\left(\frac{1.0 + u \times u_{GT} + v \times v_{GT}}{\sqrt{1.0 + u^2 + v^2}\sqrt{1.0 + u_{GT}^2 + v_{GT}^2}}\right) \tag{5.1}$$

In Table 5.1, the angular error calculation is shown for five reference 2D flows (ground truth flows), obtained by means of Eq. (5.1). We choose a set of five data. HOF2D is our multiresolution 2D Horn-Hermite optical flow approach. We compare our HOF2D algorithm, along with the 2D Horn and Schunck and Farneback implementations found in [96] and the ground-truth flows provided in [95]. The parameters used for HOF2D are the same as those described in Sections 5.4.1 and 5.4.2, $N = 4$, 5 levels of multiresolution decomposition for the SHT in 2D, $\alpha \geq 10$ and $\gamma \geq 100$, except that the necessary iterations, which can range from 20, to provide the best results. The best results are highlighted in bold and, although our approach is not always the best, it is close to the best results in each case.

Table 5.1: 2D Angular Error Calculation.

Ground Truth Images	**Horn-Schunck [96]**	**Farneback [96]**	**HOF2D**
groove2	71.400	**12.254**	14.733
groove3	67.939	15.316	**11.577**
urban2	70.839	26.425	**18.283**
urban3	79.299	39.963	**17.299**
venus	70.727	28.385	**8.929**

5.2.2 2D Endpoint Error

Another of the most common performance measure for optical flow is the Endpoint Error (EE) proposed in [97]. The error between a flow vector (u, v) and a ground-truth reference flow (u_{GT}, v_{GT}) can be useful in this case:

$$EE = \sqrt{(u - u_{GT})^2 + (v - v_{GT})^2} \tag{5.2}$$

Table 5.2 shows the absolute error 2D or error of the endpoint flow (error in flow endpoint, EE), used by [97], defined in Eq. (5.2).

Table 5.2: 2D Endpoint Error Calculation.

Ground Truth Images	**Horn-Schunck [96]**	**Farneback [96]**	**HOF2D**
groove2	3.053	0.900	**0.718**
groove3	3.537	1.305	**1.122**
urban2	8.414	6.692	**5.139**
urban3	7.440	4.924	**3.807**
venus	3.607	1.836	**0.694**

In Fig. 5.2 we can observe a comparison between the flows obtained with the 2D implementations of the Horn and Schunck algorithm [96] and our method (HOF2D).

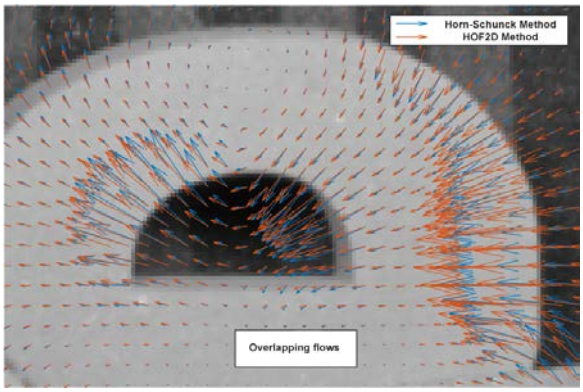

Figure 5.2: Comparison between the flow of Horn and Schunck method obtained with [96] and our HOF2D method

5.2.3 2D Interpolation Error

Another useful performance measure is the interpolation error (IE). It is defined as the mean square value of the difference between the ground-truth image and the estimated

interpolated image [98]:

$$IE = \left[\frac{1}{N} \sum_{(x,y)} \left(L(x,y) - L_{GT}\left(x,y\right) \right)^2 \right]^{\frac{1}{2}} \tag{5.3}$$

where N is the number of pixels.

Table 5.3 shows the calculation of the interpolation error (Eq. 5.3), for the set of data and algorithms already indicated. The best results are highlighted in bold and, although our approach is not always the best, it is close to the best results in each case.

Table 5.3: 2D Interpolation Error Calculation.

Ground Truth Images	**Ground Truth Flow**	**Horn-Schunck [96]**	**Farnebäck [96]**	**HOF2D**
dimetrodon	2.641	8.589	3.127	**2.865**
groove2	10.439	23.492	8.831	**10.353**
groove3	19.401	32.351	**15.703**	17.460
urban3	9.870	17.727	9.489	**8.122**
venus	8.813	20.659	**5.847**	8.835

5.2.4 2D Normalized Interpolation Error

Another interpolation error can be calculated, the mean square value of a normalized gradient inspired by [98]. The normalized interpolation error (NE) between an interpolated image $L\left(x,y\right)$ and a ground-truth image $L_{GT}\left(x,y\right)$ is given by:

$$NE = \left[\frac{1}{N} \sum_{(x,y)} \frac{\left(L(x,y) - L_{GT}\left(x,y\right) \right)^2}{\left\| \nabla L_{GT}\left(x,y\right) \right\|^2 + \varepsilon} \right]^{\frac{1}{2}} \tag{5.4}$$

where the scaling constant is selected at one ($\varepsilon = 1.0$).

With the same set of data and algorithms as Table 5.3, Table 5.4 presents the calculation of the normalized interpolation error in 2D based on (Eq. 5.4) . The best performances are highlighted in bold and most of them are in the HOF2D column. We must say that the normalized interpolation error is a weighted RMS average of the pixels, which use the image gradient as a weight factor. The normalized interpolation error compensates for the difference between the interpolation errors and the flow obtained because it gives less weight to the discontinuous regions and more weight to the regions without texture.

Table 5.4: 2D Normal Interpolation Error Calculation.

Ground Truth Images	Ground Truth Flow	Horn-Schunck [96]	Farnebäck [96]	HOF2D
dimetrodon	0.207	0.546	0.382	**0.270**
groove2	0.418	0.860	0.385	**0.329**
groove3	0.990	1.622	0.626	**0.532**
urban3	2.325	2.452	1.342	**0.700**
venus	0.801	1.376	0.434	**0.348**

In Fig. 5.3 we can see one of the images ground truth compared with the interpolated image and the error between both

(a) ***Ground Truth Image*** **(b)** ***Interpolated Image*** **(c)** ***Difference between both Images***

Figure 5.3: Comparisson between a Ground Truth Image and the Interpolated Image

5.3 Materials and Overview of the 3D Method

In this section, we present a series of materials related to the development and tuned of our multiresolution 3D Horn-Hermite optical flow approach (HOF3D) and to the data corresponding to the cardiac images of which we wish to estimate its movement. Likewise, we present an overview of the implementation of the HOF3D method.

5.3.1 Dataset Description

To conduct the experiments, two types of data sets were used in this project, the first one consists of three synthetic volumes generated. A hexahedron (Fig. 5.4) with a lateral

displacement, another one, a sphere with a deformation (5.5(b)) and the last of them, a simulation of a tornado (Fig. 5.6)[1]. In these synthetic volumes, we have the certainty of the direction, magnitude, and direction of the displacements of the voxels. In such a way that when evaluating the optical flow this helped to better calibrate the algorithms in terms of the number of iterations, smoothing factors, and weighting of the Hermite coefficients used. The sizing of such parameters was also carried out for the CT volumes used, which is described in a subsequent subsection. In all the subsequent images, the flow vectors are magnified to be better observed.

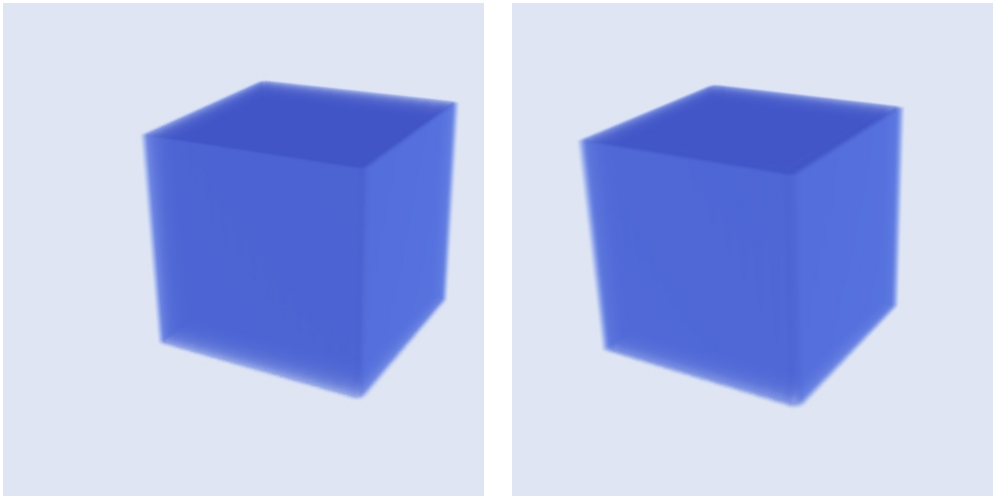

(a) ***Hexahedron*** **(b)** ***New position of the hexahedron***

Figure 5.4: A hexahedron displaced.

[1]The technique used to create these data is as-yet unpublished but was first described in an informal presentation by Roger Crawfis of Ohio State University at a talk held in Salt Lake City in May, 1999

(a) ***Sphere*** **(b)** ***Flattened Sphere***

Figure 5.5: A synthetic sphere with a posterior deformation.

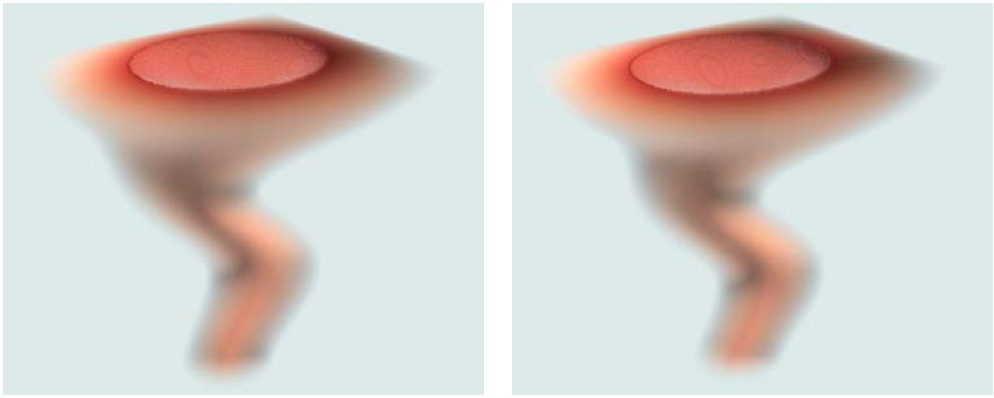

(a) ***Tornado - step1*** **(b)** ***Tornado - step2***

Figure 5.6: A synthetic tornado with a posterior twisting.

The second dataset used in this project, consists of two cardiac computed tomography studies ($3D + t$). The CT volumes were obtained in a 16-slice tomograph (at 120 kVp @ 900 mA) built with 128 detectors. The dimensions of each volume are $512 \times 512 \times 10$ at 12 bits per pixel. The clinical protocol starts by injected a contrast agent to the patient and the study is carried out in synchrony with the electrocardiogram (ECG) signal. A cardiac CT volume used is shown in Figure 5.7.

It should be noted that the acquisition of cardiac images are performed in connection with the electrocardiogram and are acquired with the patient in respiratory apnea to avoid artifice by movement. In Appendix A, a brief description of the most important characteristics of CT cardiac images related to this project is presented.

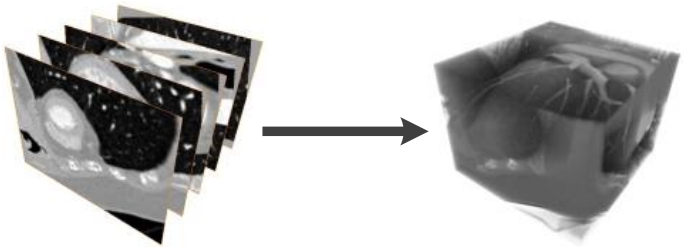

Figure 5.7: Cardiac CT images, slices and volume.

5.3.2 Overview of the Method in 3D

In Figure 5.8 we show an overview of our proposal. First, we have the cardiac volume slices, belonging to two consecutive steps of the cardiac cycle considered, which make up volume 1 and volume 2 respectively; for each volume, we obtain a multiresolution expansion related to the coefficients of the steered Hermite transform. Such coefficients are used to carry out the calculation of the optical flow within the mentioned HOF3D approach. Once the vector field belonging to the optical flow over the whole cardiac volume was obtained, we used the portion of the volume related to the segmented left ventricle to finally obtain only the masked vectors with this part of the cardiac volume.

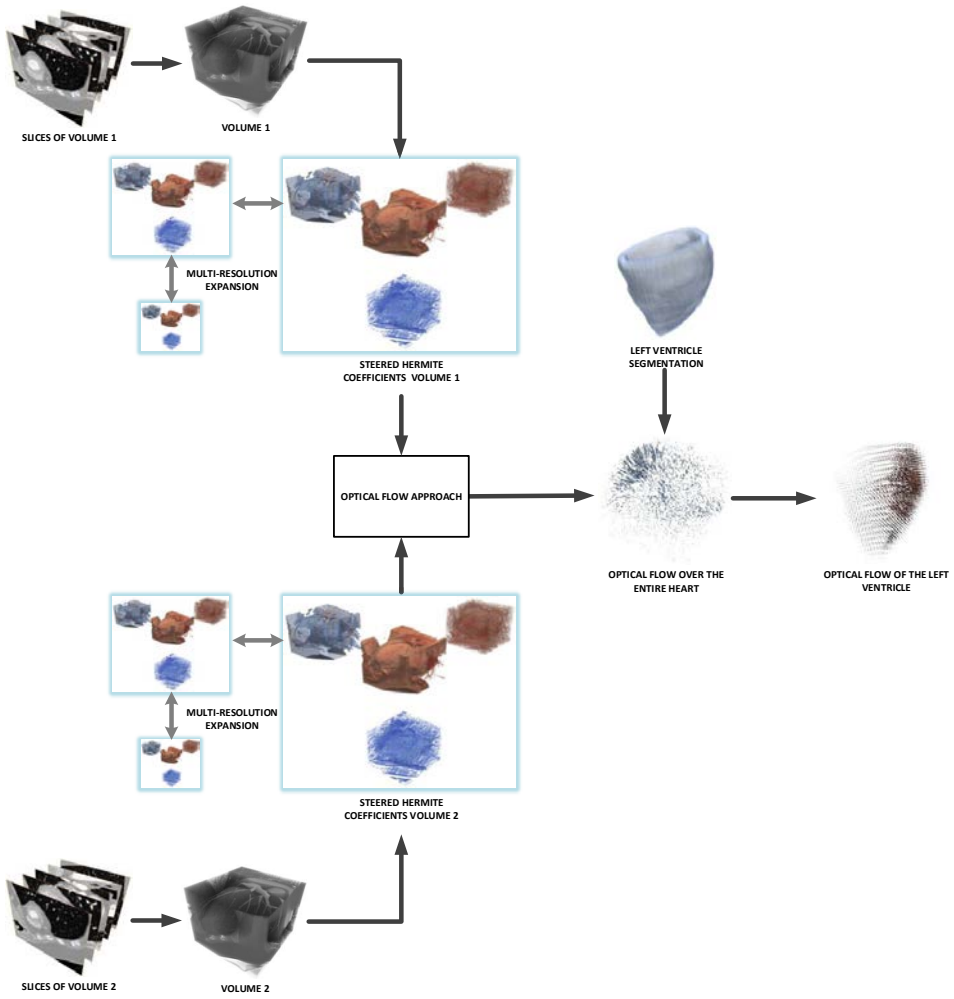

Figure 5.8: Procedure to implement the HOF3D approach.

In absence of a 3D motion ground-truth in CT images, which is used to evaluate the accuracy of the optical flow estimation, we validate our proposal by calculating the interpolation error, which is defined as the root mean-square (RMS) difference between the known volume $L(\mathbf{x}, t+1)$ at time $t+1$ and the reconstructed volume $L_{GT}(\mathbf{x}, t+1)$, is calculated [6, 19] as we showed in the Equation (5.5):

$$IE_{3D} = \left[\frac{1}{M} \sum_{\mathbf{x}} \Big(L(\mathbf{x}, t+1) - L_{GT}(\mathbf{x}, t+1) \Big)^2 \right]^{\frac{1}{2}} \tag{5.5}$$

where M is the number of voxels.

We also computed a second measure of interpolation performance, the normalized interpolation error between an interpolated volume $L(\mathbf{x}, t+1)$ and a ground-truth volume $L_{GT}(\mathbf{x}, t+1)$, which is given as in [97]:

$$NE_{3D} = \left[\frac{1}{M} \sum_{\mathbf{x}} \frac{\Big(L(\mathbf{x}, t+1) - L_{GT}(\mathbf{x}, t+1) \Big)^2}{\Big\| \nabla L_{GT}(\mathbf{x}, t+1) \Big\|^2 + \varepsilon} \right]^{\frac{1}{2}} \tag{5.6}$$

that represents a gradient-normalized RMS error, where ε is a scaling constant (e.g., $\varepsilon = 1$).

The interpolation errors are useful to know how good the calculation of the optical flow is when there is no available ground truth flow, the normalized interpolation error has the additional advantage of being normalized concerning the magnitudes of the intensity changes that the volume of the reference.

5.4 Parameter Tuning and Sensitivity Analysis

In this section, we present first, the parameter tuning of the Hermite transform: cubic window size, maximum order of decomposition, and multiresolution levels. Then, we perform a sensitivity analysis of the parameters used in the optical flow proposal: smoothing term and weight parameter.

5.4.1 3D Hermite Transform Parameter Tuning

Although the constants, values and weight parameters are difficult to select, in Section 2.2.2, we present which are the suitable values to the cubic window and in consequence, the maximum expansion order N of the Hermite transform, thus, experimentally found that we achieved a good estimation of optical flow results ($NE_{3D} < 0.1$) and avoiding blur artifacts for our dataset with: a cubic window of $5 \times 5 \times 5$ pixels, i.e., a maximum expansion order of $N = 4$ for the SHT and 5 levels of multiresolution decomposition for the SHT. Below these values, we would obtain errors 2.5 to 3 times larger than those reported. It should be noted that this strategy allows us to handle large displacements, which occur from one step to another in a cardiac cycle.

5.4.2 Optical Flow Parameter Sensitivity Analysis

We performed a parameter sensitivity analysis to find the best values. Weight parameter γ of the HOF3D functional Equation (4.2) is used to weigh the contribution of the high order Hermite coefficients in those regions where the intensity does not remain constant from one volume to another. On the other hand, the softness parameter α can help recover the motion information from their neighbors in those regions where the gradient is zero,

e.g., intensity homogeneous regions. It is carried out through averages from structures with high frequencies, e.g., edges and textures. Large values of α give us a smoother flow but this is relatively less important at locations with high image gradients than elsewhere.

For determining the values of the smoothness weight α and the weight parameter γ , first, we compute the 3D optical flow over the cardiac CT sequences and then we analyze the behavior of the Interpolation Error (IE) and Normalized Interpolation Error (NE) metrics.

From Figure 5.9, the curves show that the best results for IE and NE are for $\alpha \geq 10$ and $\gamma \geq 100$ (bottom of the mesh).

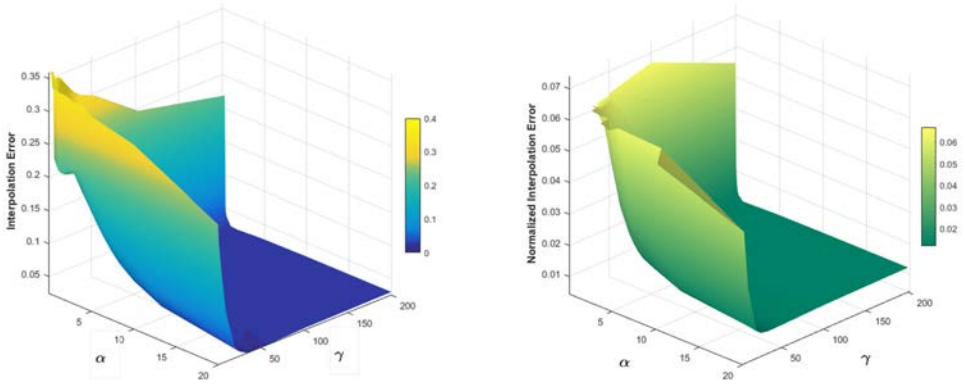

(a) **(b)**

Figure 5.9: Interpolation Error (**a**) and Normalized Interpolation Error (**b**), for parameter sensitivity analysis.

Concerning the number of iterations of the method, it was set to 50 because a number greater than 50 was the one that gives us the required numerical convergence according to our tests.

5.5 3D Interpolation Errors

5.5.1 Interpolation Errors in Synthetic Volumes

In Table 5.5 we can see the results of the Calculation of 3D Interpolation Errors for the synthetic volumes. The best results are highlighted with bold.

Table 5.5: 3D Interpolation Errors for the synthetic volumes

Volumes	3D Horn-Schunck[20]	HOF3D Method
Deformed hexahedron	0.32430	**0.15441**
Tornado	0.34580	**0.04982**
Flattened sphere	0.36807	**0.02007**

In Table 5.6 we can see the results of the Calculation of 3D Normalized Interpolation Errors.

Table 5.6: 3D Normalized Interpolation Errors for the synthetic volumes

Volumes	3D Horn-Schunck[20]	HOF3D Method
Deformed hexahedron	0.26167	**0.05751**
Tornado	0.30274	**0.00755**
Flattened sphere	0.21575	**0.00695**

5.5.2 Interpolation Errors in Cardiac Volumes

To evaluate the accuracy of the HOF3D method, we compared it with the 3D variant of the method of Sun et al. [20] We calculated the corresponding interpolation errors (IE and NE) using both proposals. Figure 5.10 presents a diagram of the steps to calculate the interpolation errors.

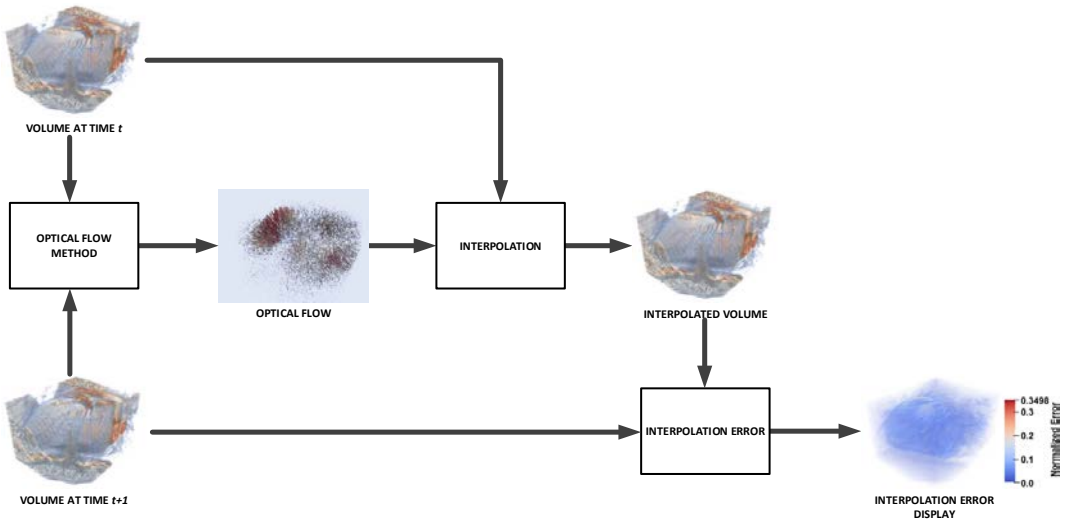

Figure 5.10: Steps to calculate and visualize the Interpolation Error.

Figure 5.11 shows a cardiac CT volume where we can observe the original volume (Figure 5.11a), the interpolated volume (Figure 5.11b), the difference between the original volume and its interpolated result (Figure 5.11c) using the 3D variant of the method of Sun et al. [20]. The results were compared with a modified version of the Sun method in 3D and for different noise levels. Both algorithms used were optimized and the evaluation of the results was carried out through a forward reconstruction, from the volume at time t to time $t + 1$, through the 3D optical flow obtained. The interpolation error display is a visualization of the terms within the summation in Equation (5.6).

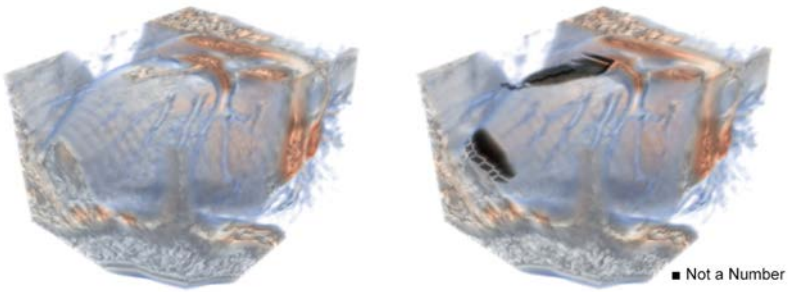

(a) *Original Volume*

(b) *Volume Interpolated using the Horn and Schunck method*

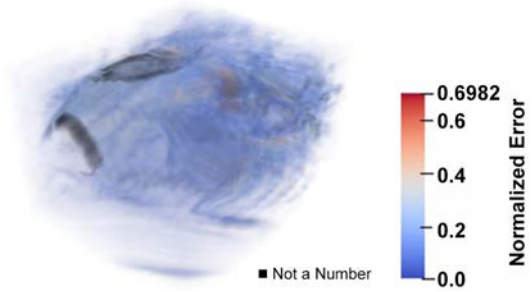

(c) *Error between Original and Interpolated Volumes using the Horn and Schunck method*

Figure 5.11: A cardiac CT volume showing the original volume, the interpolated volume using the 3D variant of the method of Sun et al. [20] and the error between the original volume and its interpolated result.

On the other hand, in order to compare our method, in Figure 5.12 we show the same cardiac CT volume as in Figure 5.11 where, again, we can observe the original volume (Figure 5.12a), the interpolated volume (Figure 5.12b), the difference between the original volume and its interpolated result (Figure 5.12c) using our HOF3D method.

In Figure 5.13, we show the interpolation errors obtained using the Sun et al. [20] and the HOF3D methods through the whole cardiac cycle (0% to 90%) for two CT sequences. In both sequences, we can observe the beginning of the increase in the interpolation error from 20% to 30%, when the contraction movement occurs and from 50% to 60% of the cardiac cycle, in full dilation movement. This is where we have a couple of cardiac movements of greater magnitude.

We can observe in the plots of Figure 5.13, both for the interpolation error and the normalized interpolation error, that even in each of the stages of the complete cardiac cycle,

the HOF3D method gives better results and lower errors are obtained.

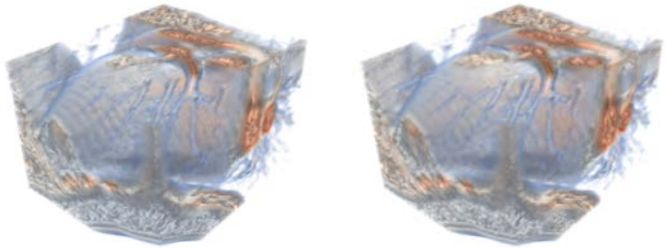

(a) ***Original Volume*** **(b)** ***Volume Interpolated using the HOF3D method***

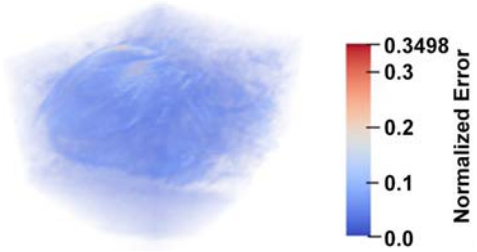

(c) ***Error between Original and Interpolated Volumes using HOF3D method***

Figure 5.12: A cardiac CT volume showing the original volume, the Interpolated Volume using the HOF3D method and the error between the original volume and its interpolated result.

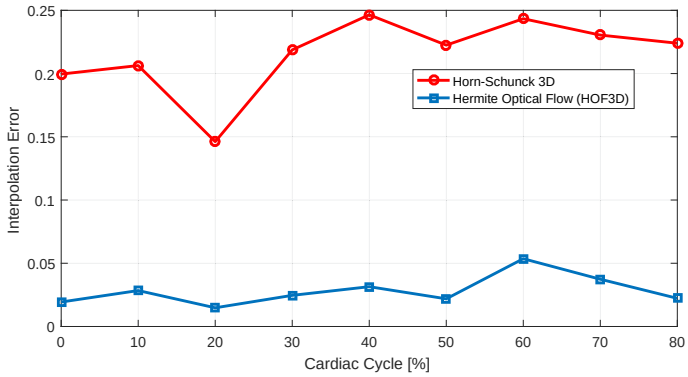

(a) ***Interpolation Error***

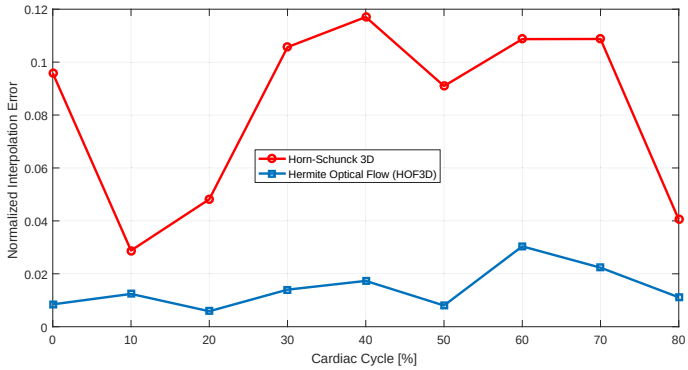

(b) ***Normalized Interpolation Error***

Figure 5.13: Interpolation Error and Normalized Interpolation Error. For the 3D Horn-Schunck (red dashed line) and Hermite Optical Flow in 3D (blue solid line) methods. From sequences of cardiac CT volumes.

5.6 Robustness to Noise

In another experiment, we carried out an analysis of robustness to noise of the proposed method. For this, we added Gaussian noise, with different standard deviations ($\sigma_n = 0, 5, 10, 15, 20, 30$) and zero mean, to the cardiac volumes. In Figure 5.14 we can see one of the volumes used for the test, with three different values of σ_n.

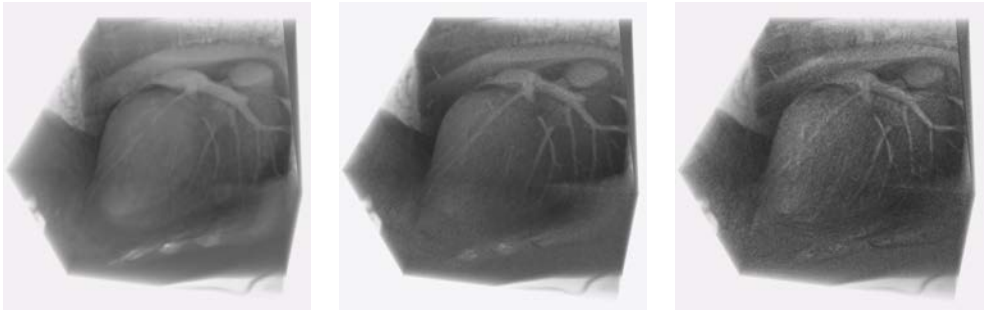

(a) ***Volume without noise*** **(b)** ***Volume with noise,*** $(\sigma_n = 10)$ **(c)** ***Volume with noise,*** $(\sigma_n = 30)$

Figure 5.14: Volume with pseudo-random noise.

Table 5.7 shows the interpolation error and the normalized interpolation error for the noise levels given for the HOF3D method, using optimized parameters $\alpha = 10$, $\gamma = 100$ and $N = 4$. We can observe that although the standard deviation of the introduced noise grows, the interpolation error and the normalized interpolation error remain small, this is because the coefficient of order 0 of the Hermite transform $L_{000}(\mathbf{x})$ (Equations 2.19, 2.27 and 4.2), contains a smoothed version of the original volume and this DC coefficient allows to reduce any component of high-frequency noise, additionally, in our approach, the steered Hermite coefficients use Gaussian derivatives, which incorporate information from neighboring voxels in the structure of cardiac volumes, which makes the proposed algorithm more robust to this type of noise [13, 99]. By the another hand, it should be noted that although the errors are low, the addition of noise represents an increase in the interpolation error of 71.4% and for the normalized interpolation error of 80%, comparing one test without noise and the other test with noise of $\sigma_n = 30$.

Table 5.7: Interpolation Error and Normalized Interpolation Error computed for a cardiac volume with several standard deviations σ_n of Gaussian noise.

Gaussian Noise (σ_n)	**Interpolation Error**	**Normalized Interpolation Error**
0	0.03190	0.01696
5	0.03499	0.01954
10	0.03778	0.02168
15	0.04295	0.02563
20	0.04597	0.02779
30	0.05468	0.03387

5.7 3D Optical Flow Results

5.7.1 Three-dimensional Optical Flow Results in Synthetic Volumes

To test our method in a controlled manner, we used three synthetic volumes that were subjected to displacement in the case of a hexahedron, a deformation, in the case of a sphere, and twisting in the case of a tornado. Later we tested our method with the whole cardiac volumes.

Fig. 5.15 shows a synthetic hexahedron which it's being displaced laterally and upwards. In Fig. 5.15(a) the hexahedron is set in the first position and Fig. 5.15(b) the hexahedron is displaced laterally and upwards, in Fig. 5.15(c) the resulting flow is shown as well as the displaced hexahedron which coincides with the hexahedron extrapolated from the first volume and flow obtained. Fig. 5.15(d) displays only the resulting vector field of movement. In Fig. 5.15(e) and Fig. 5.15(f) we can visualize the 3D vector field using streamlines. This technique was first presented on [100] by computing a large number of field lines, integrating the vector field starting from random seed points. The lines are displayed to give a much better spatial understanding of the field's structure.

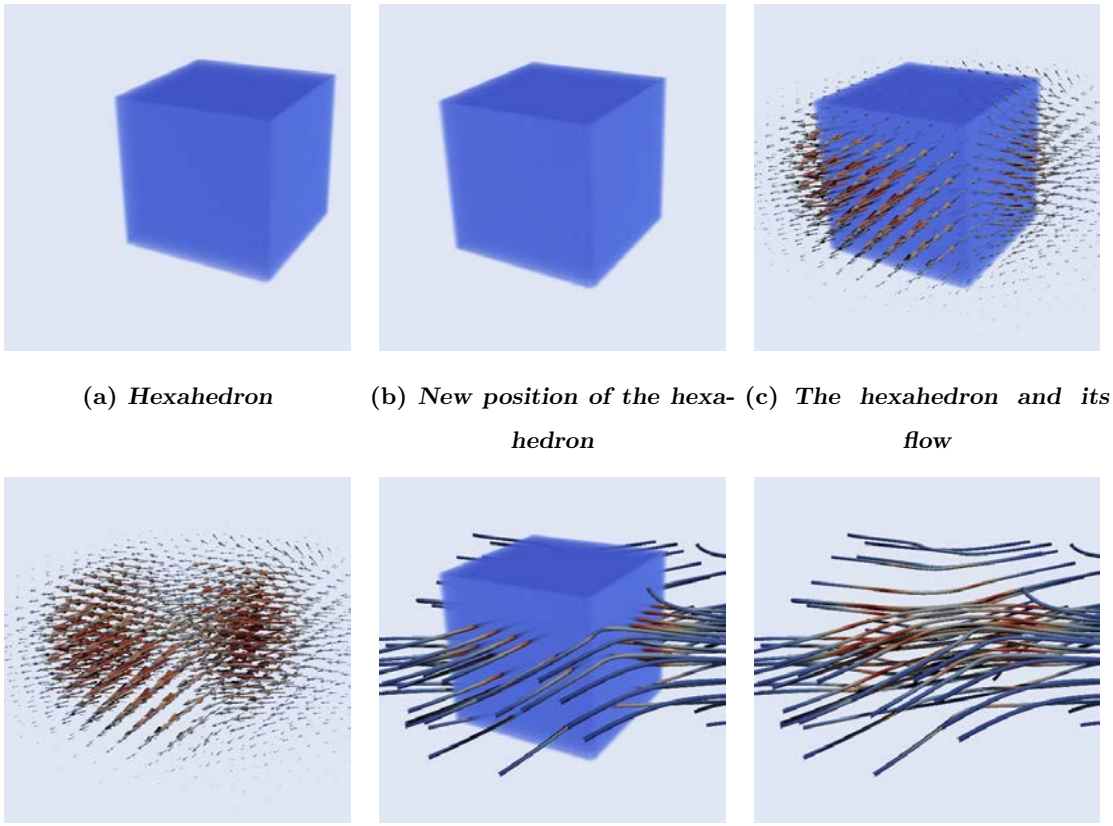

(a) *Hexahedron* (b) *New position of the hexahedron* (c) *The hexahedron and its flow*

(d) *Only flow* (e) *The hexahedron and its streamlines* (f) *Only streamlines*

Figure 5.15: A hexahedron displaced, its flow and streamlines

In Fig. 5.16 we have a synthetic sphere. For Fig. 5.16(a) the sphere is in its first stage, Fig. 5.16(b) represents the sphere being expanded and in Fig. 5.16(c), the resulting flow is shown along with the interpolated sphere through the flow. Fig. 5.16(d) displays only the resulting vector field of movement. Fig. 5.16(e) and Fig. 5.16(f) we can visualize the 3D vector field using stream lines.

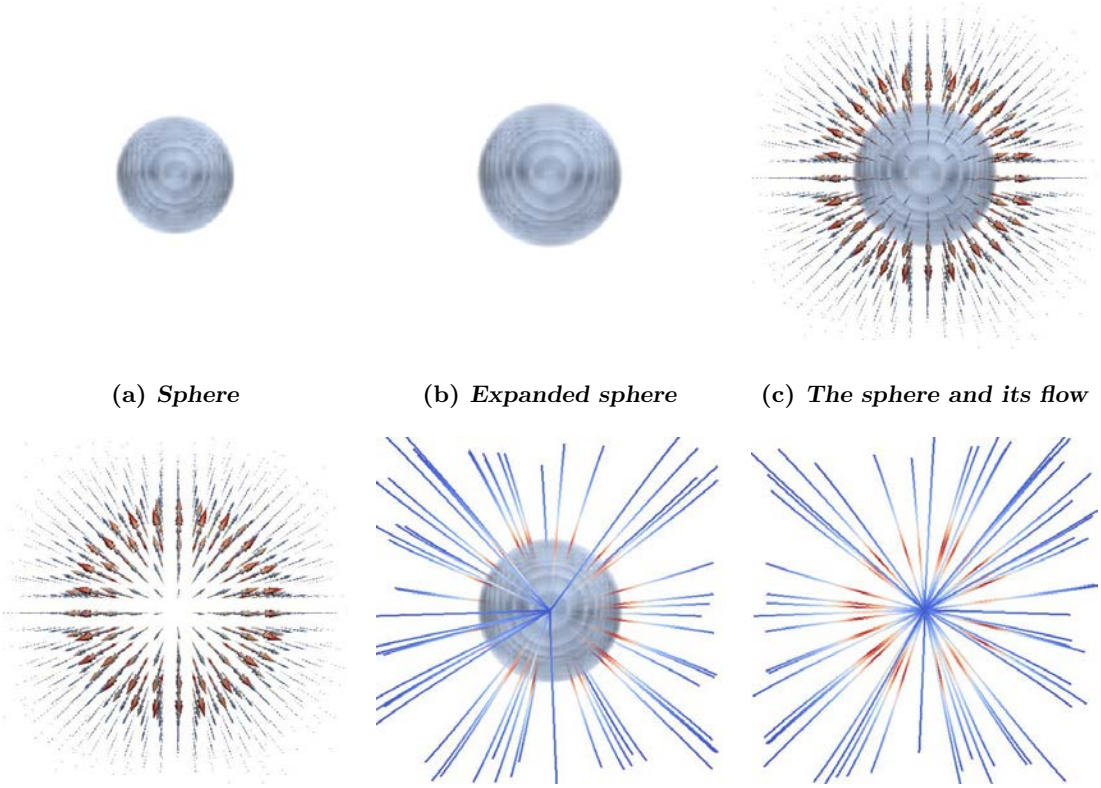

(a) ***Sphere*** **(b)** ***Expanded sphere*** **(c)** ***The sphere and its flow***

(d) ***Only flow*** **(e)** ***The sphere and its streamlines*** **(f)** ***Only streamlines***

Figure 5.16: An expanded sphere, its flow and streamlines

Fig. 5.17 shows a synthetic tornado. For Fig. 5.17(a) the tornado is in its first stage, Fig. 5.17(b) represents the tornado twisting and in Fig. 5.17(c), the resulting flow is shown along with the interpolated tornado through the flow. Fig. 5.17(d) displays only the resulting vector field of movement. Fig. 5.17(e) and Fig. 5.17(f) we can visualize the 3D vector field using stream lines.

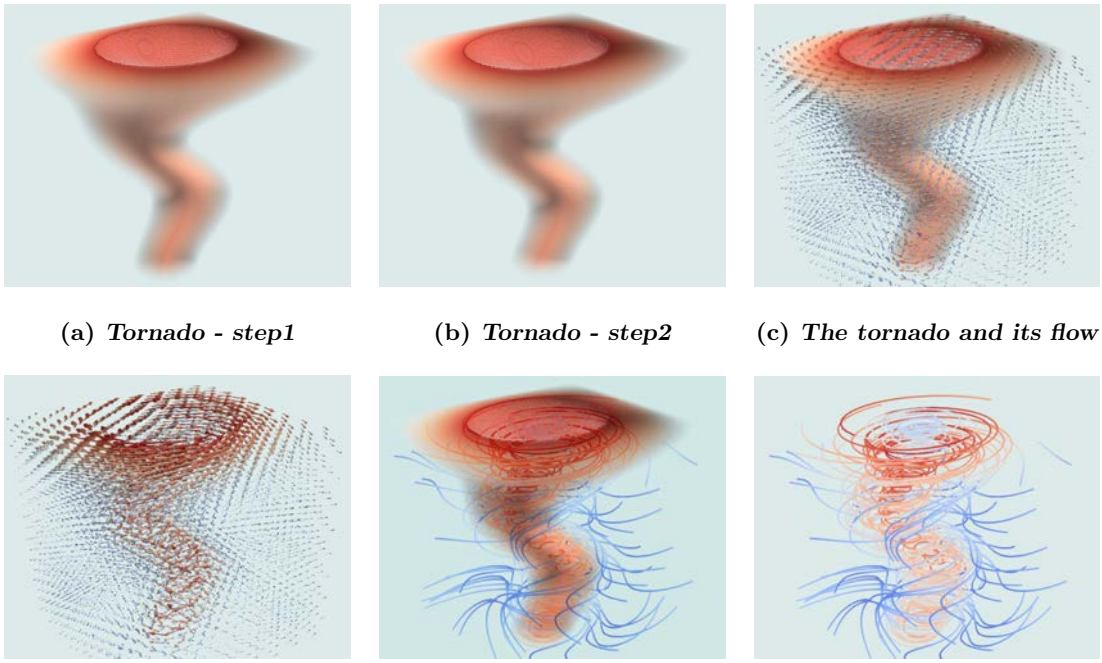

(a) *Tornado - step1* (b) *Tornado - step2* (c) *The tornado and its flow*

(d) *Only flow* (e) *The tornado and its streamlines* (f) *Only streamlines*

Figure 5.17: A tornado twisting, its flow and streamlines

5.7.2 Three-dimensional Optical Flow Results in Cardiac Volumes

In this section, we show the 3D optical flow estimation computed on CT volumes for a whole cardiac cycle. For descriptive purposes, only some representative parts of such a cardiac cycle are shown. In most cases, the display of the magnitudes of the optical flows was exaggerated to observe the qualitative characteristics of the movements.

Figure 5.18 shows the results of a 3D Optical flow of two cardiac CT volumes computed at phases 20-30% (when a contraction movement occurs) using the HOF3D method. Figure 5.18(a,b) show two phases of the cardiac cycle of volume (for better viewing a cut of that volume was made). Figure 5.18(c,d) show the same phases of volume along with the three-dimensional optical flow field. Finally, Figure 5.18(e,f) illustrate only the optical flow.

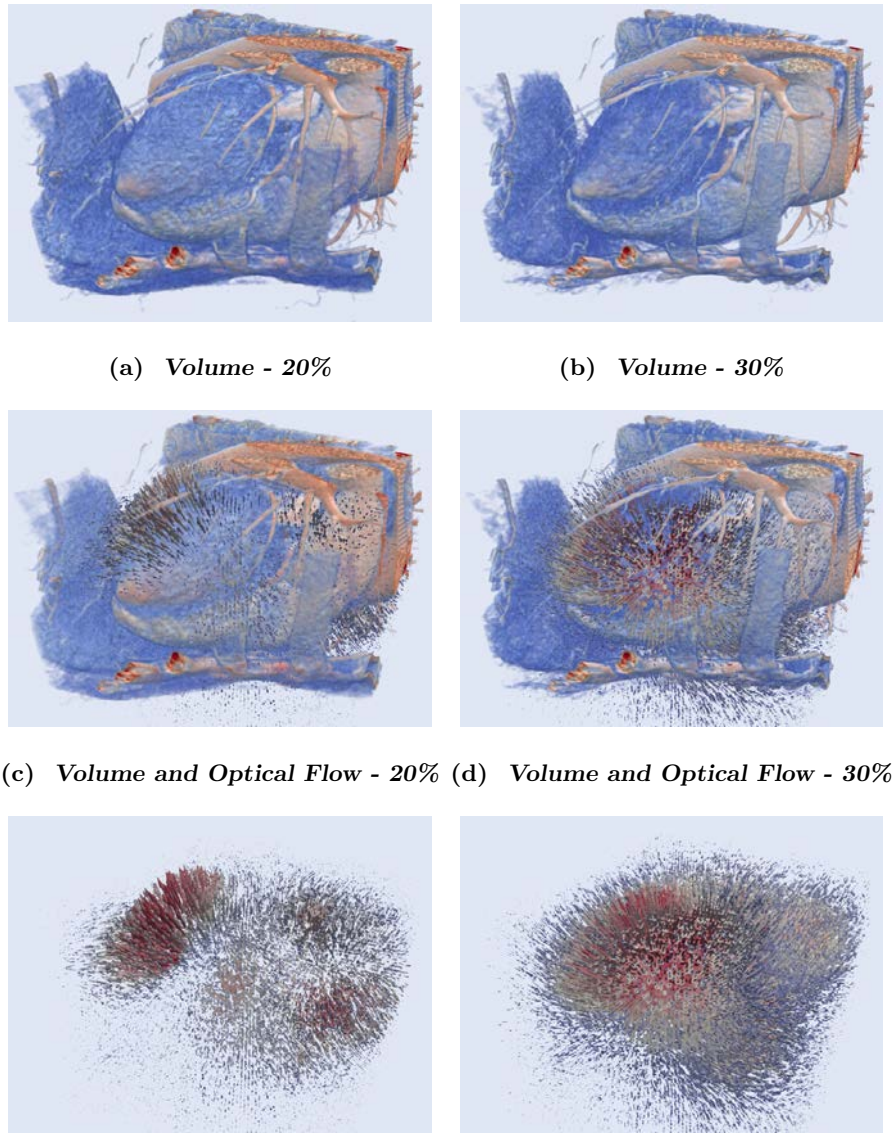

(a) *Volume - 20%* (b) *Volume - 30%*

(c) *Volume and Optical Flow - 20%* (d) *Volume and Optical Flow - 30%*

(e) *Only Optical Flow - 20%* (f) *Only Optical Flow - 30%*

Figure 5.18: Results of 3D Optical Flow of a segmented cardiac CT volume computed at phases 20–30%.

Figure 5.19 presents the results of a 3D Optical flow of two cardiac CT volumes computed at phases 50–60% (when a dilation movement occurs) using the HOF3D method. Figure 5.19(a,b) show two phases of the cardiac cycle of volume (for better viewing a cut that volume was made). Figure 5.19(c,d) show the same phases of volume along with the

three-dimensional optical flow field. Also, Figure 5.19(e,f) present only the optical flow.

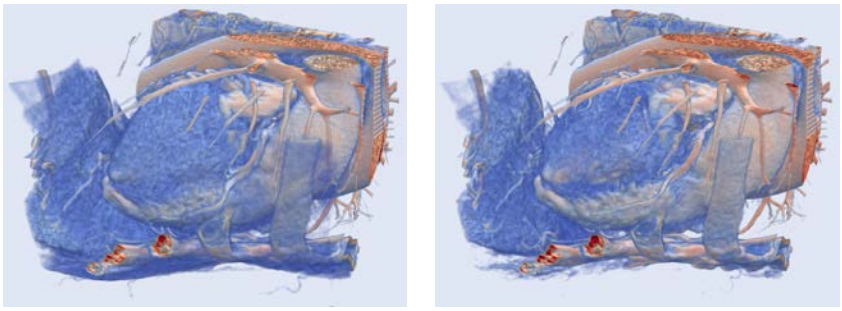

(a) ***Volume - 50%*** (b) ***Volume - 60%***

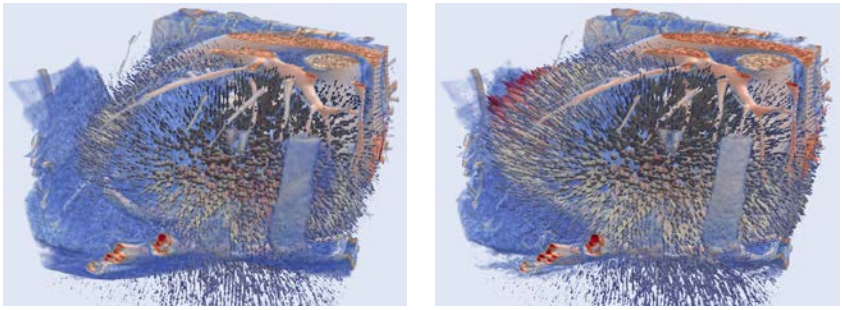

(c) ***Volume and Optical Flow - 50%*** (d) ***Volume and Optical Flow - 60%***

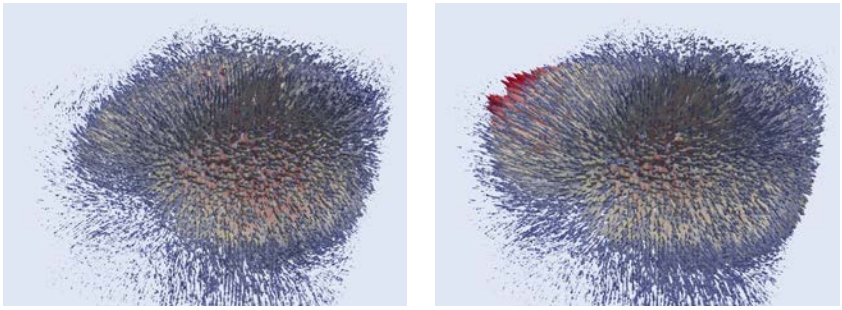

(e) ***Only Optical Flow - 50%*** (f) ***Only Optical Flow - 60%***

Figure 5.19: Results of 3D Optical Flow of a segmented cardiac CT volume computed at phases 50–60%.

5.8 3D Optical Flow Estimation of the Left Ventricle

The importance of the study of the left ventricle has been established extensively. The left ventricle adapts, for example, to arterial hypertension, and this leads to the development of different geometric patterns [101]. For a better understanding of some diseases, the movement of the left ventricle has been studied during the cardiac cycle in normal subjects and patients with coronary arterial disease, mitral stenosis or atrial septal defect [102]. Works describing the global and local movement have been presented, focusing mainly on the left ventricle [103]. To present the optical flow estimation of the left ventricle, first, a segmentation of it is required. We use the level sets method of Osher and Sethian [104]. This method is a powerful, suitable, and flexible approach to the segmentation of CT volumes where there aren't well-defined boundaries. The level sets method was applied to the CT volumes using the Seg3D tool [105]. For this tool, a seed volume is used to find similar regions to the original one. Then, the segmented region will be expanded to surrounding pixels that match the statistics of the original seeded area. The spread may also be retracted in some instances if the seeded areas do not match certain criteria (edge weight and threshold range). Until the convergence, the algorithm will be expanded (or contracted) to the segmented region.

Figure 5.20 shows an example of the segmentations obtained (colored region) in the context of their location within the whole cardiac volume.

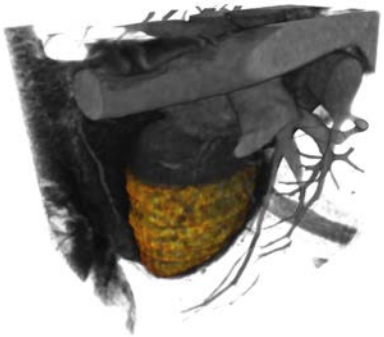

Figure 5.20: A whole cardiac volume and its left ventricle segmented.

Similarly to the work done in Section 5.5, and if we focus on the phase where a contraction movement occurs for the left ventricle, we can observe the interpolation error for a left ventricle segmented showing the original volume in Figure 5.21(a), the interpolated volume using the 3D variant of the method of Sun et al. [20] is shown in Figure 5.21(b), the error between the original volume and this interpolated result, in Figure 5.21(d). Also, the optical flow is calculated by the HOF3D method. Then, the interpolation of the left ventricle is obtained, which is shown in Figure 5.21(c). The difference between the original volume and that interpolated volume can be observed in Figure 5.21(e).

(a) ***Original LV- 30%***

(b) ***LV Interpolated using the 3D method of Sun et al. [20]***

(c) ***LV Interpolated using the HOF3D method***

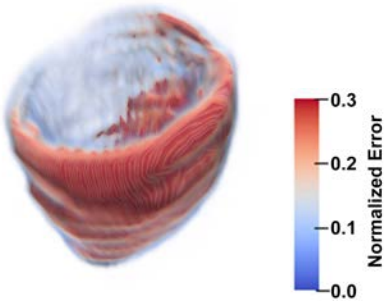

(d) ***Error using the 3D method of Sun et al. [20]***

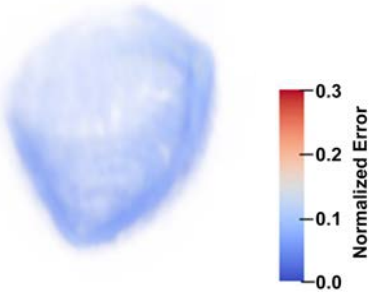

(e) ***Error using the HOF3D method***

Figure 5.21: Interpolation Errors for the left ventricle at 30%.

Another example of interest, where there is more interpolation error, is the 60% of cardiac phase, it is also when a dilatation movement occurs for the left ventricle. We can observe the interpolation error for a left ventricle segmented for the original volume in Figure 5.22(a), the interpolated volume using the 3D method of Sun et al. [20] in Figure 5.22(b), the error

between the original volume and this interpolated result in Figure 5.22(d). Also, the optical flow is calculated by the HOF3D method. Then, the interpolation of the left ventricle is obtained and shown in Figure 5.22(c). The difference between the original volume and that interpolated volume can be observed in Figure 5.22(e).

(a) ***Original LV- 60%***

(b) ***LV Interpolated using the 3D method of Sun et al. [20]***

(c) ***LV Interpolated using the HOF3D method***

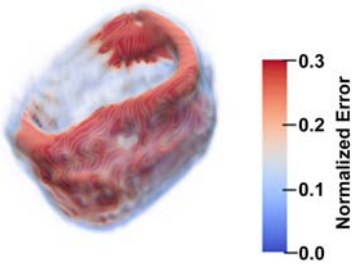

(d) ***Error using the 3D method of Sun et al. [20]***

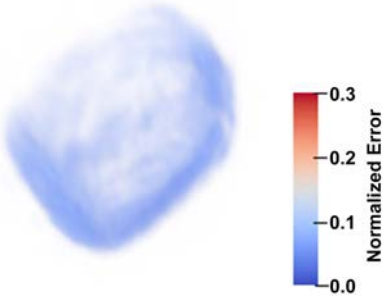

(e) ***Error using the HOF3D method***

Figure 5.22: Interpolation Errors for the left ventricle at 60%.

Figure 5.23 contains the results of the normalized interpolation error with the Sun et al. [20] method. In Figure 5.23(a) we present a set of volumes from 30% to 70% of the cardiac cycle, in Figure 5.23(b), the interpolated volumes corresponding to each stage of the cardiac cycle are shown. Figure 5.23(c) graphically displays the normalized interpolation error for the volumes of sections a and b respectively.

Figure 5.24 contains the results of the normalized interpolation error with the HOF3D method. Figure 5.24(a) presents a set of volumes from 30% to 70% of the cardiac cycle, Figure 5.24(b) shows the interpolated volumes corresponding to each stage of the cardiac cycle. Figure 5.24(c) graphically displays the normalized interpolation error for the volumes of sections a and b respectively.

(a) ***Original Volumes***

(b) ***Interpolated Volumes***

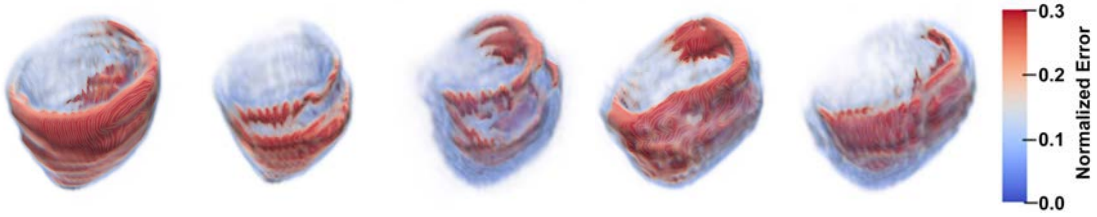

(c) ***Normalized Interpolation Error***

Figure 5.23: Left Ventricle from 30% to 70% of the cardiac cycle and the results with 3D method of Sun et al. [20].

(a) ***Original Volumes***

(b) ***Interpolated Volumes***

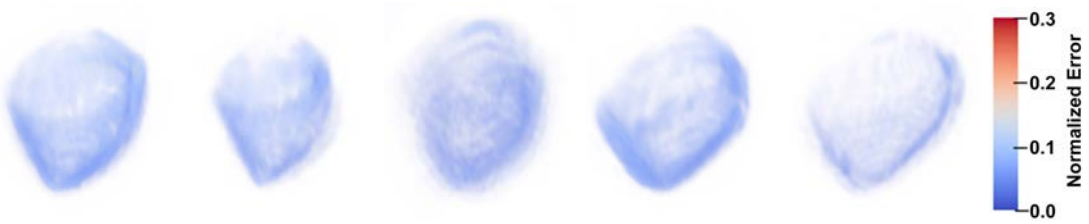

(c) ***Normalized Interpolation Error (HOF3D method)***

Figure 5.24: Left Ventricle from 30% to 70% of the cardiac cycle and the results with HOF3D method.

Figures 5.25 and 5.26 present the results of a 3D Optical flow of two segmented cardiac CT volumes, showing a contraction and relaxation movement respectively using the HOF3D method. Figure 5.25(a,c) are two phases of the segmented cardiac cycle of volume computed at phases 20–30%, the same way as Figure 5.26(a,c) but in phases 40–50%. Figure 5.25(b,d), Figure 5.26(b,d) show only their respective optical flows.

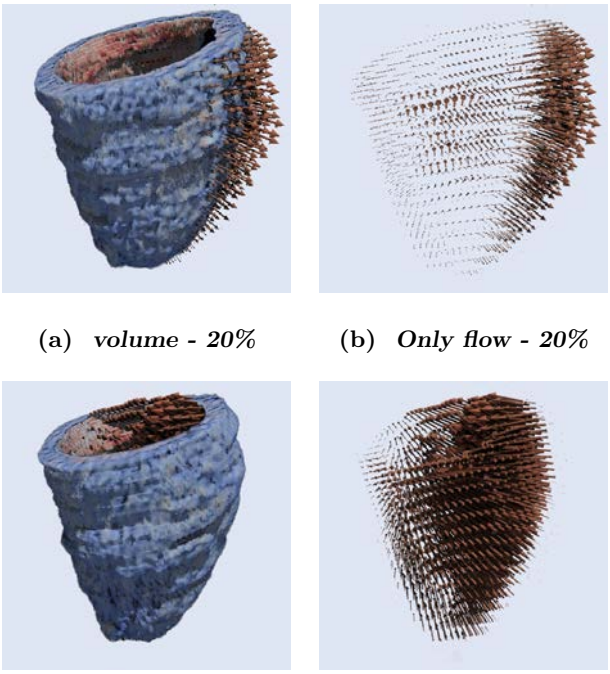

(a) ***volume - 20%*** **(b)** ***Only flow - 20%***

(c) ***volume - 30%*** **(d)** ***Only flow - 30%***

Figure 5.25: Results of 3D Optical Flow of a segmented cardiac CT volume (left ventricle) computed at phases 20–30% (contraction movement).

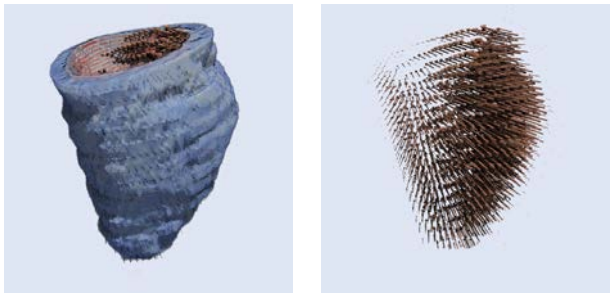

(a) ***volume - 40%*** **(b)** ***Only flow - 40%***

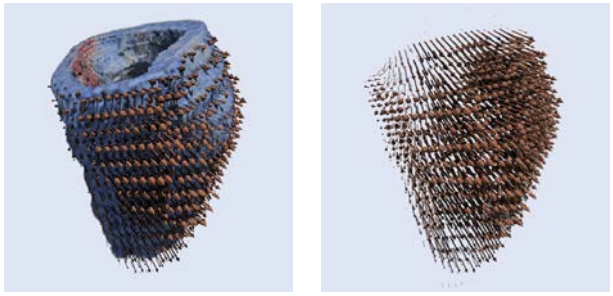

(c) ***volume - 50%*** **(d)** ***Only flow - 50%***

Figure 5.26: Results of 3D Optical Flow of a segmented cardiac CT volume (left ventricle) computed at phases 40–50% (relaxation movement).

Figure 5.27 contains the results corresponding to the optical flow calculated with the HOF3D method. We can observe a set of left ventricle volumes from 10% to 100% of the cardiac cycle.

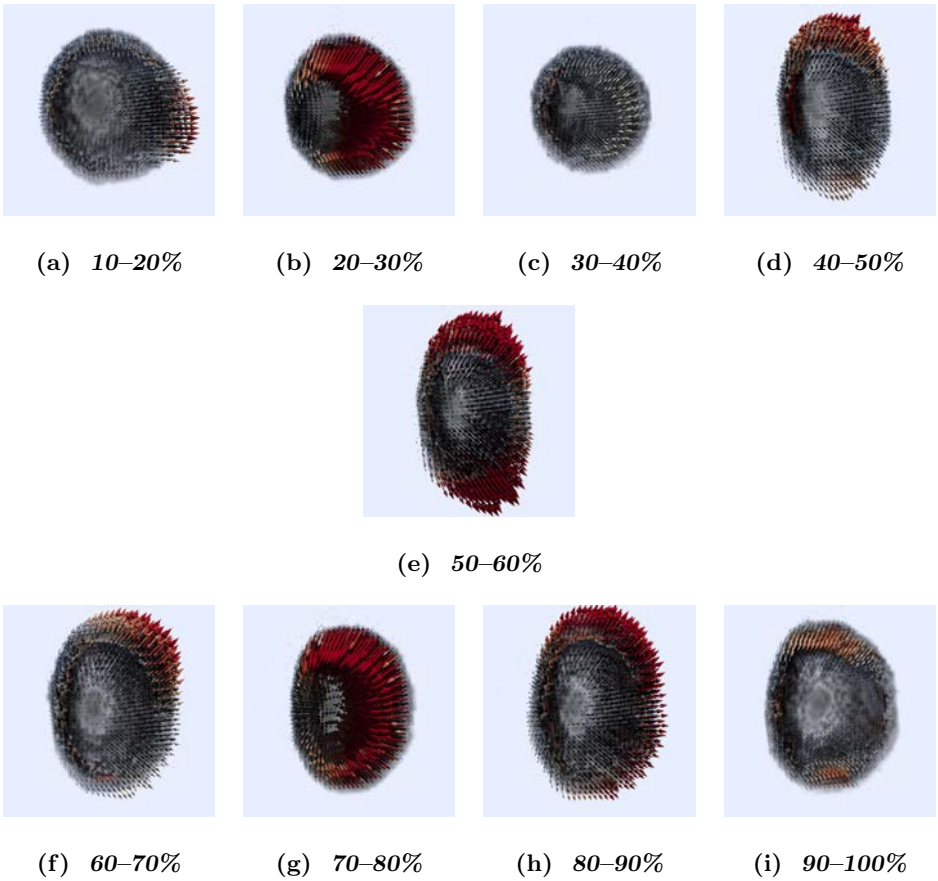

(a) ***10–20%*** **(b)** ***20–30%*** **(c)** ***30–40%*** **(d)** ***40–50%***

(e) ***50–60%***

(f) ***60–70%*** **(g)** ***70–80%*** **(h)** ***80–90%*** **(i)** ***90–100%***

Figure 5.27: Results of 3D Optical Flow of a segmented cardiac CT volume (left ventricle–short axis).

In Appendix B, some additional figures to the outcomes presented in this section are shown along with alternate representations of the results that can be obtained through the 3D optical flow.

5.9 Discussion

In the first group of results (Figures 5.18 and 5.19), the entire cardiac volume and its respective calculated optical flows can be observed in context. The best way to display this 3D flow has been attempted. Despite a large number of 3D arrows of different sizes, it is possible to observe either the contraction pattern (Figure 5.18) or the expansion pattern (Figure 5.19). The optical flow is shown using of Paraview [106, 107] whose style of repre-

senting the vectors of the optical flow is similar to the previous works in [108] and recently in [109].

We focused on estimating the movement in one of the most important structural parts of the heart, the left ventricle. To achieve this goal we have segmented that heart region, which is shown in Figure 5.20. We can see examples in [110, 111] of the deployment of the three-dimensional vectors of the obtained optical flow. However, in all the remaining figures within the set of results obtained, rather than deploying the obtained optical flow vectors, we decided to show graphically, a measure of the performance achieved in the estimation of cardiac movement, specifically in the left ventricle. The relevance of the figures thus represented is that the errors obtained can be observed graphically, first in the interpolated volumes (Figures 5.21 and 5.22, items b and c), where we can compare a similar and known method with the proposed one. In the same figures mentioned, the interpolation error is observed through a three-dimensional representation that matches the analyzed volumes (Figures 5.21 and 5.22, items d and e). In those figures, the biggest errors are the ones represented in red, and the smallest tend to blue.

We observe a more extensive sequence of the cardiac cycle (five phases) in order to provide greater clarity. In this selection of phases of the cardiac cycle we can observe the movement of contraction and dilatation in the left ventricle. In Figures 5.23 and 5.24 in part a, we observe the original volumes. In Figures 5.23 and 5.24 part b, we see the interpolated volumes with a comparison between the two methods. In Figures 5.23 and 5.24 item c, we see a graphical representation of the normalized interpolation error.

Finally, Figures 5.25 and 5.26 present more explicitly the segmented left ventricle and their respective optical flows during the contraction and relaxation movements. Figure 5.27 shows the segmented volumes from the short view concerning all phases of the cardiac cycle (from 10% to 100%). Motion vectors were exaggerated for clarity. In the field of medical images, and in addition to the cardiac movement, this approach can be used with benefit in pulmonary movement. In general, in applications where we have three-dimensional data, such as cardiac and pulmonary medical images, stereoscopic images and video, 3D meteorological data, volumes formed by point clouds in general. Where we want to characterize how they evolve over time. For future work, there is a great margin of opportunity to improve the times in the calculations of the Hermite transform, for which a faster version was not used. For the energy functional used, some other local and global characteristics can be incorporated that allow us to further reduce the uncertainties obtained.

Chapter 6

Conclusions

In this project, we have proposed a method to estimate the optical flow completely in $3D + t$, that is, in a three-dimensional space (x, y, z) plus time, because the analysis of two-dimensional motion restricts all possible deformations in the different directions of reference (i.e., radial, circumferential and longitudinal).Therefore, three-dimensional motion analysis can overcome such limitations by better describing, in all directions, the deformations.

Our approximation of motion estimation has included the well-known differential method of Horn and Schunck with the additional information provided by the coefficients of the Steered Hermite transform used within the restriction terms of the function to be minimized. The Steered Hermite transform is a model that incorporates some important properties of the first stages of the human visual system, such as the overlapping Gaussian receptive fields, the Gaussian derivative model of early vision [70], and a multiresolution analysis [112, 113]. This proposed algorithm is more robust to noise due to the advantage represented by the analysis of the spatial scale provided by the Hermite transform itself that can be determined for objects at different spatial dimensions. Additionally, and due to the calculation of high order Gaussian derivatives, the estimation of the movement can be improved by including structures related to them.

Although representative results were shown for a particular volume, the method was tested with 3 different full cardiac volumes and 45 partial cardiac volumes, with similar results for the estimation of the optical flow. These volumes were not previously tested with any other 3D optical flow method. We evaluated the results obtained using two measurements on the interpolation errors, with these errors we also adjusted the most appropriate parameters in the different cardiac sets considered. We observed that interpolation errors increased around the phases where movements occur most rapidly (the contraction phase). We were able to verify that the proposed method (HOF3D) has lower interpolation errors compared to the modified 3D method of Sun et al. [20].

For the algorithm, one of the main contributions in this research is to have obtained an estimate of the optical flow with improved precision, together with the use of the Hermite transform in 3D images that made it possible to increase said precision.

We isolated the three-dimensional flow vectors corresponding to the left ventricle, over the entire cardiac cycle. We calculated the interpolation errors obtained with our method, comparing the results with the other method already mentioned.

Our proposal also aims to contribute to a better understanding of cardiac movements and, with this, to make feasible the detection of some possible diseases. We consider that because the cardiac organ is immersed in a three-dimensional space, the best way to represent its movements should be in the same three-dimensional space. Future work may focus on recognizing the cardiac movement patterns related to the vectors obtained in our three-dimensional optical flow approximation.

Appendix A

Cardiac CT Images

Computed tomography (CT) is a modality of the acquisition of medical images routinely used in medical practice. In this modality, a set of two-dimensional images are generated that are sliced with information about the internal anatomy of a patient, the three-dimensional images are obtained through projections at different angles and measurements of the degree of absorption of the beam that crosses the body. The application of this technology and its advances in cardiology are presented in [114].

CT is the oldest of all modalities for the acquisition of three-dimensional medical images. In the 70s, it had a great impact because of its ability to examine internal structures of the human body in a non-invasive way very accurately. Additionally, the problems associated with the loss of details that involve the superimposition of a two-dimensional detector to form 3D images are eliminated.

The objective of CT is to represent in two dimensions, the attenuation coefficient of X-rays along a thin transverse region in the human body. Each tissue in the different structures of the body, having a different composition, exhibits different responses concerning X-rays. Thus, it can describe the structures of the body and their respective anatomical relationships. When a monochromatic X-ray beam passes through the body, said beam is absorbed or scattered throughout the structures through which the beam passes. The absorption will depend on both the physical density and the composition of the structures, in addition to the energy that the beam has. The interactions represent the molecular ionization generated by scattering and photoelectric spreading [115].

The X-ray source and the detector are collimated for a good definition of the beam that passes through the transverse plane and that when rotated around the body, records the absorption patterns of X-rays from different directions on the plane cross. The detectors can detect different intensities with 0.1% error and the attenuation coefficients of the individual structures can be determined with 0.5% discrepancy. The distribution of the attenuation coefficients is determined by the Lambert-Beer Law, which indicates that when a monoenergetic X-ray beam passes through an object of variable density, the beam is attenuated according to a type of relationship exponential.

A.1 CT Acquisition Techniques

A.1.1 Conventional Computed Tomography

This technique produces a simple two-dimensional image of a cross-section of the body from the X-rays provided, which are registered from an angle around the body. To obtain three-dimensional images, the procedure is repeated in adjacent sections. This procedure has some drawbacks, such as the occasional movement of the patient and the width of each section that occurs during the scan time in all cuts [116].

Respecto to images of the heart in this type of technique, they are not useful because the acquisition time is 1 to 3 seconds and normal contractions of the heart occur in a time slightly longer than a second. Due to this, blurred representations of the cardiac cavities are generated in this technique. To improve this technique, synchronization with the electrocardiogram (ECG) is used. The ECG is obtained simultaneously to order the CT projection data in a time window that corresponds to the phases of the cardiac cycle.

A.1.2 High-Resolution Temporary Computed Tomography

Ultrafast Computed Tomography systems, allow measuring changes in the shape and dimension of the heart as well as the spatial distribution of blood flow in the myocardium [117]. For this purpose, the volume is explored using a set of multiple cross-sections, parallel and fine in a sufficiently short period such that we have sufficient resolution. The spatial resolution is 1 mm in the heart. The observation speed is based on the speed of the endocardial surface movement in the transverse plane during the maximum systolic ejection phase. This facilitates the assessment of the exact location, magnitude, and nature of cardiovascular abnormalities and pathologies, such as coronary artery damage and myocardial ischemia [118].

A.1.3 Electron Beam Computed Tomography

Here the magnetic deflection of an electron beam is used instead of the mechanical movement of the X-ray tubes (see Fig. A.1). This is known as Electron Beam Computed Tomography (ECBT) [119]. The source of the X-rays consists of semicircular tungsten rings. The electron beams are swept along each of the rings in different instances which generates a fan-shaped rotating beam. On the other side, multiple detectors record the intensity of the incident beam.

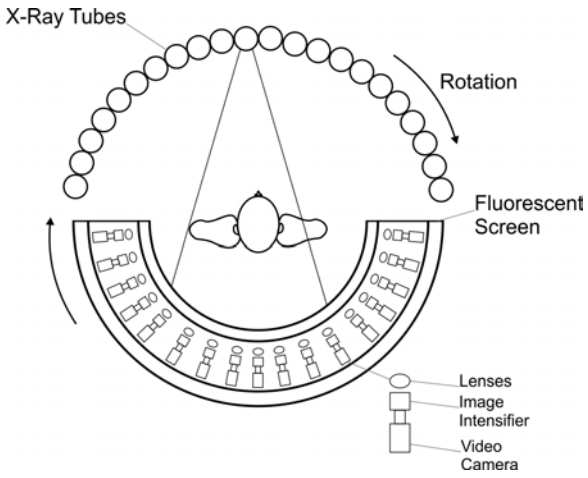

Figure A.1: Electron Beam Computed Tomography system.

The EBCT operates in three modes, in which the acquisition time and spatial resolution vary. In cinema mode, acquire each scan in 50 ms at a frequency of 17 scans per second for each anatomical level. In the flow mode, a single specific phase of the cardiac cycle is used. In volume mode, eight transaxial cuts are scanned by storing the intensity of the X radiation, using approximately 224 ms to complete this operation. With this technique, images can be obtained from the apex to the base of the heart. Although the spatial resolution in the transaxial direction is much lower than in the plane direction. EBCT has been widely used for the assessment of coronary artery damage [120, 121].

A.1.4 Helical Computed Tomography.

Helical CT is an alternative to the detection and quantification of coronary artery damage. It is considered a modality of volumetric acquisition in which the translation of the patient occurs at a constant speed through the equipment during the continuous rotation of the system consisting of the source and the detector as shown in Figure A.2.

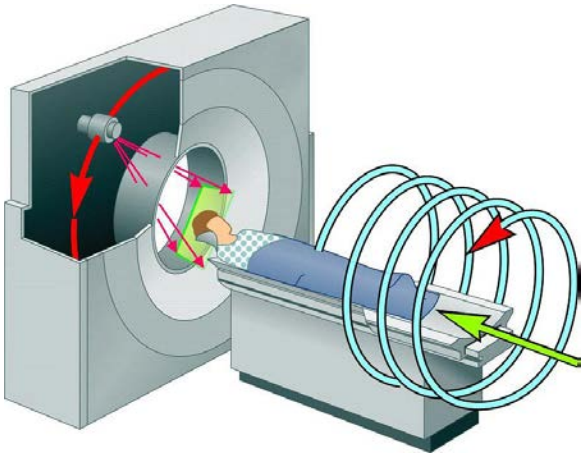

Figure A.2: Helical Detector System [122].

In the scanning process, the X-ray lamp describes a spiral path around the patient [123]. The reconstruction of the sequence of the transaxial sections from the data set gives us the volume that can be visualized as images of conventional transaxial sections or three-dimensional methods. Although this technique is sometimes considered devoid of important characteristics such as sensitivity, accuracy, and reproducibility, there are works in which the calcification of the coronary arteries has been quantified using this technique activated by the ECG [124].

Although there is a wide variety of medical image acquisition, CT acquisition has high quality and can compete widely with the quality shown on magnetic resonance imaging [125].

A.1.5 MultiSlice Computed Tomography (MSCT)

It is part of the most recent developments in helical CT. It is based on the simultaneous acquisition of more than a single tomographic plane and uses acquisition systems with multiple detectors (Fig. A.3).

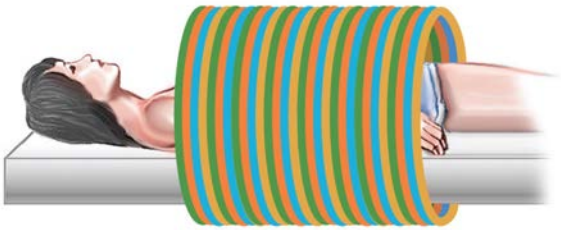

Figure A.3: MSCT Detector System [126]

In this mode, high spatial resolution can be obtained, that is, sub-millimeter, which provides a spatial resolution of 20 phases per cardiac cycle for the representation of $3D + t$ cardiac images. It can be used for the evaluation of the arterial coronary tree and is of interest for cardiac quantification and ventricular mass.

In general, achieving the analysis of cardiac images is a difficult task due to several factors, such as reconstruction artifacts due to rapid movements and the variation in heart rate. The variation of the gray levels of the images during the cardiac cycle, due to the propagation of the contrast product and the reconstruction from several cycles. As well as the same variability that exists among patients. On the other hand, the location and orientation of the heart in the thorax, the variation of the field of view (FOV) as well as the variation of the craniocaudal coverage, can introduce difficulties in the analysis [127].

A.2 CT Image Reconstruction

Conventional reconstruction algorithms require that during exploration, the source of lightning X and the detector are in the same plane of the cut to be rebuilt. The goal of the reconstruction algorithm is determine the path of the ray beam geometrically X that passes through the body. A great variety of mathematical solutions to the reconstruction problem have been developed, which can be classified in [128]: summation methods, series expansion methods, transform-based methods, and analytical methods direct.

The most used method for image reconstruction CT is called convolution method or filtered back projection, which is essentially considered as a method of direct analytical solution of the equation integral derived from the basic projection formula. In this method, the blur produced when the projections overlap, it is corrected by filtering them, applying a convolution process with a function or filter appropriate, before performing back projection or sum of projections [129]. On the other hand, the algebraic reconstruction technique (ART) [130] is the most widely used iterative algebraic algorithm, due to its simplicity and efficiency [131].

A.3 CT Image Display

A convention in CT is to replace the attenuation value calculated for each voxel in the reconstruction matrix with an integer called CT number, which is expressed in Hounsfield units (HU). The Hounsfield unit is a relative scale that allows intensities values are linearly related to the coefficient of water attenuation. In this scale the maximum attenuation it is represented with white and the minimum attenuation with black. Table A.1 shows the Hounsfield values in different organs of the human body.

Table A.1: Hounsfield unit (HU) for various organs of human body (Adults) [132].

Predefined threshold value	Minimum	Maximum
Bone	226	3071
Soft Tissue	-700	225
Enamel	1553	2850
Compact Bone	662	1988
Spongial Bone	148	661
Muscle Tissue	-5	135
Fat Tissue	-205	-51
Skin Tissue	-718	-177

Table 2 shows the various factors that affect the quality of the CT images. The first five problems have been solved with the advances achieved in the design of new based equipment technologies. The last two are basically related to the problem of reconstruction, which is a highly studied problem. The factors indicated, introduce distortion or error in the image. Such distortions are called artifacts [133]. Wolbarst describes artifacts as aberrations that arise at the interface of the structures that are explored with radiological properties significantly different [134].

Table A.2: Factors that affect the quality of the CT image [114]

Factor	Affectation
1) Characteristics of the initial beam.	When the radiation is small, few photons will affect the detectors and consequently, the variance of the CT number between neighboring voxels will be quite large.
2) Energy levels.	The increase in technical factors such as mA or kV reduces image noise, but there is an increase in the dose of radiation applied to the patient.
3) Number of projections used.	Increasing the total number of projections improves the resolution of the projected image in the Radon domain but increases the radiation dose, which should be kept as low as possible.
4) Thickness of the scanned section.	The reduction of the thickness of the cut supposes an increase of the spatial resolution, thus, when the thickness of the cut is thinner, the image has more definition.
5) X-ray beam scattering.	Because the photons emitted by the X-ray tube cover a wide range in the z-direction, the collimators restrict the flow of radiation to a narrow region. Approximately 99% of the photons emitted are blocked by the collimator.
6) Size of the voxel in reconstruction.	Reducing the voxel size (to increase the detail) increases the noise because fewer photons are absorbed in each voxel.
7) Reconstruction algorithm used.	Image reconstruction is the phase in which the set of scanned data is processed to produce an image. The quality of the digital image depends on the algorithm used in the reconstruction process.

Appendix B

3D Optical Flow (Additional Visualizations)

In this work, we mostly use Paraview software [106, 107, 135] to display the results of the optical flow obtained. ParaView is an open-source, multi-platform data analysis and visualization application built on top of VTK with much of the capability of VTK without requiring them to write programs. We were able to build visualizations to analyze their data using qualitative and quantitative techniques.

To extend the results of the optical flow obtained, this appendix complements the way to display them, being able to observe the same result from another perspective. For that purpose, we used CT volumes computed from 0 to 90% in whole cardiac volumes. For descriptive purposes, only some representative parts of the said cardiac cycle are shown. Then, results are displayed for a part of the structure of the cardiac volume, which is the left ventricle.

In Fig. B.1 we can see the results of a 3D optical flow of two segmented cardiac CT volumes computed at phases 0-10% (when a contraction movement occurs) using the HOF3D method. Fig. B.1(a) and Fig. B.1(b) show two phases of the segmented cardiac cycle of the volume, and Fig. B.1(c) shows the volume and the respective optical flow. In Fig. B.1(e) and Fig. B.1(f) we appreciate the difference between different ways of displaying flow vectors, with smaller and larger sampling, respectively. Meanwhile, Fig. B.1(h) only display the vectors and the corresponding streamlines that occur in the contraction movement for the cardiac volume used.

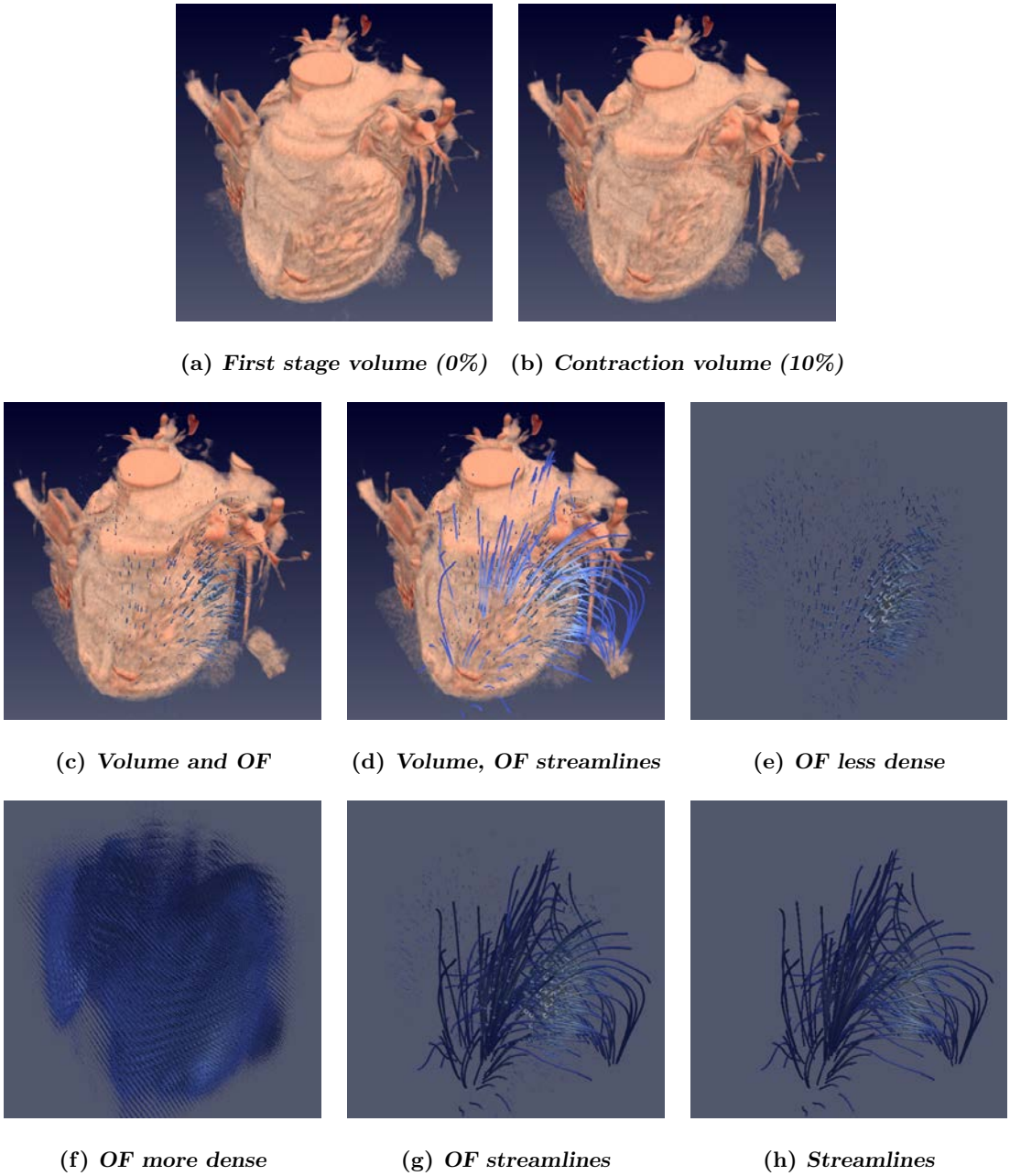

(a) ***First stage volume (0%)*** (b) ***Contraction volume (10%)***

(c) ***Volume and OF*** (d) ***Volume, OF streamlines*** (e) ***OF less dense***

(f) ***OF more dense*** (g) ***OF streamlines*** (h) ***Streamlines***

Figure B.1: A CT volume showing cardiac contraction movement (0-10%), its optical flow, and its streamlines.

On the other hand, Fig. B.2 shows the results of the 3D optical flow of two segmented

cardiac CT volumes computed at phases 40-50% (when a dilation movement occurs) using the HOF3D method. Fig. B.2(a) and Fig.B.2(b) show two phases of the segmented cardiac cycle of the volume, and Fig.B.2(c) shows the respective optical flow. In Fig. B.2(e) and Fig. B.2(f) we appreciate the difference between different ways of displaying flow vectors, with smaller and larger sampling, respectively. Meanwhile, Fig. B.1(h) only display the vectors and the corresponding streamlines that occur in the dilation movement for the cardiac volume used.

Another characteristic that we should not ignore are the different ways in which we can represent the optical flow vectors of the HOF3D method. In all representations the same color map was used (blue for smaller magnitude, red for larger magnitude). Again, in Fig. B.3 and Fig. B.4 we compare, in different ways, the contraction and dilation movement in the segmented LV. First, in Figures B.3(c) and B.4(c) the optical flow result is represented using two-bidimensional arrows. Figures B.3(c) and B.4(c) show the field of velocities using three-dimensional arrows. Meanwhile, the optical flow is shown through boxes in Figures B.3(e) and B.4(e). Also, we can represent the OF using cones (Figures B.3(f) and B.4(f)), cylinders (Figures B.3(g) and B.4(g)) and using spheres as it is shown in Figures B.3(h) and B.4(h).

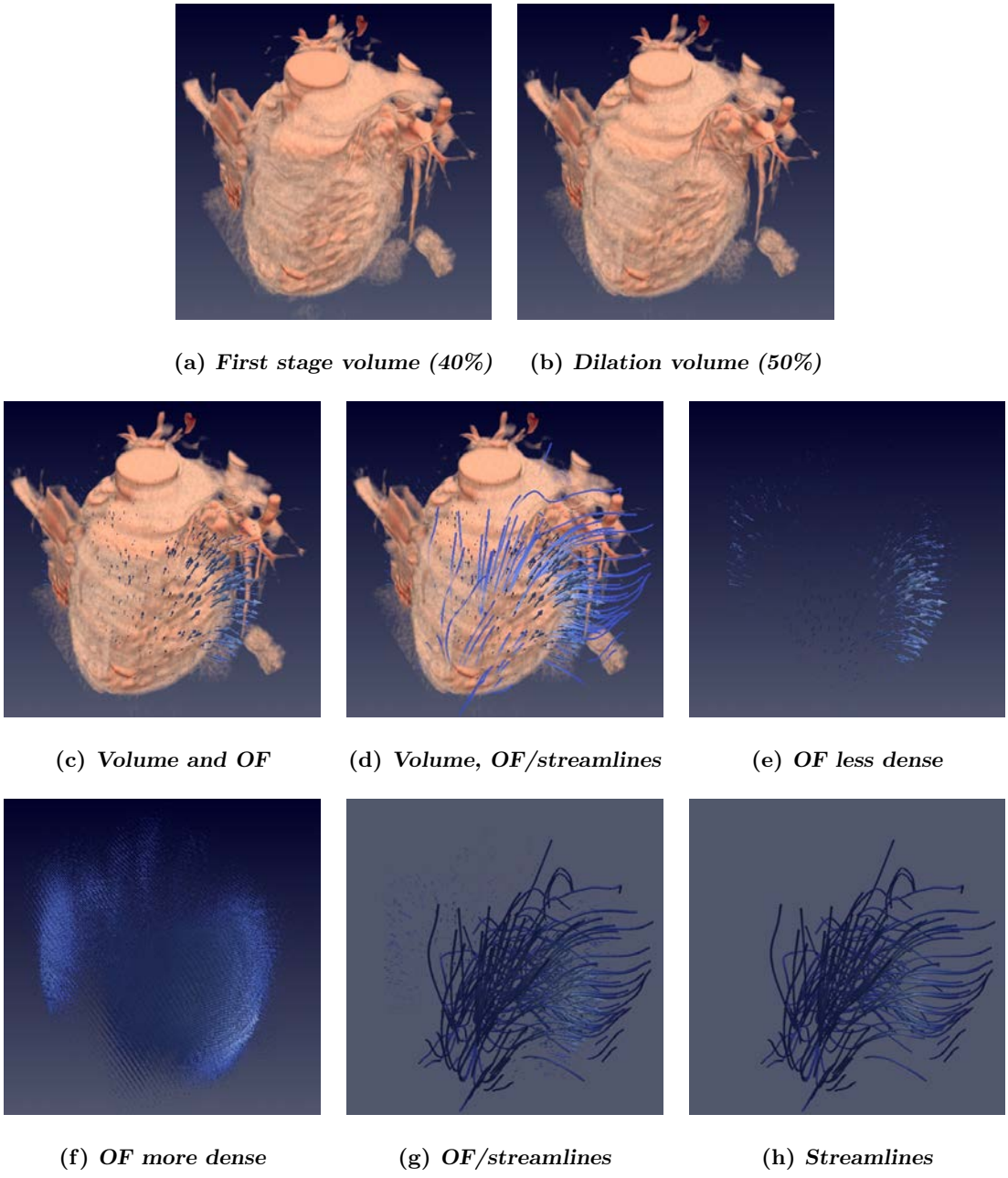

(a) ***First stage volume (40%)*** (b) ***Dilation volume (50%)***

(c) ***Volume and OF*** (d) ***Volume, OF/streamlines*** (e) ***OF less dense***

(f) ***OF more dense*** (g) ***OF/streamlines*** (h) ***Streamlines***

Figure B.2: A CT volume showing cardiac dilatation movement (40-50%), its optical flow, and its streamlines.

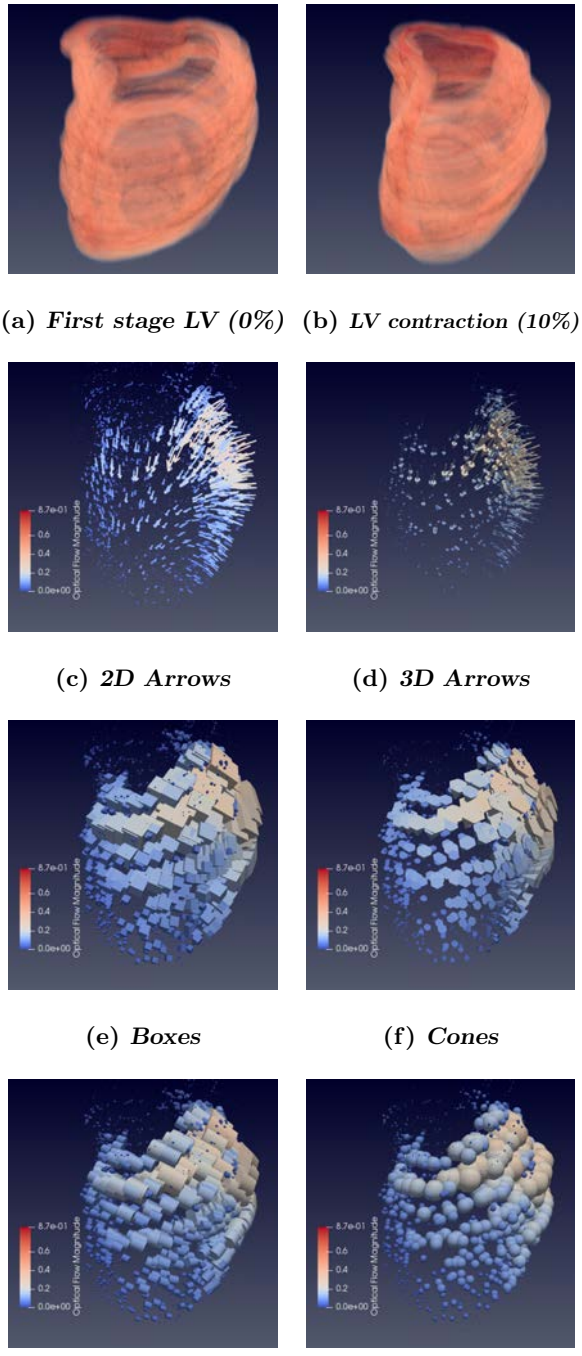

(a) ***First stage LV (0%)*** **(b)** ***LV contraction (10%)***

(c) ***2D Arrows*** **(d)** ***3D Arrows***

(e) ***Boxes*** **(f)** ***Cones***

(g) ***Cylinders*** **(h)** ***Spheres***

Figure B.3: The resulting optical flow estimation, of the cardiac contraction movement in the LV, represented in different ways.

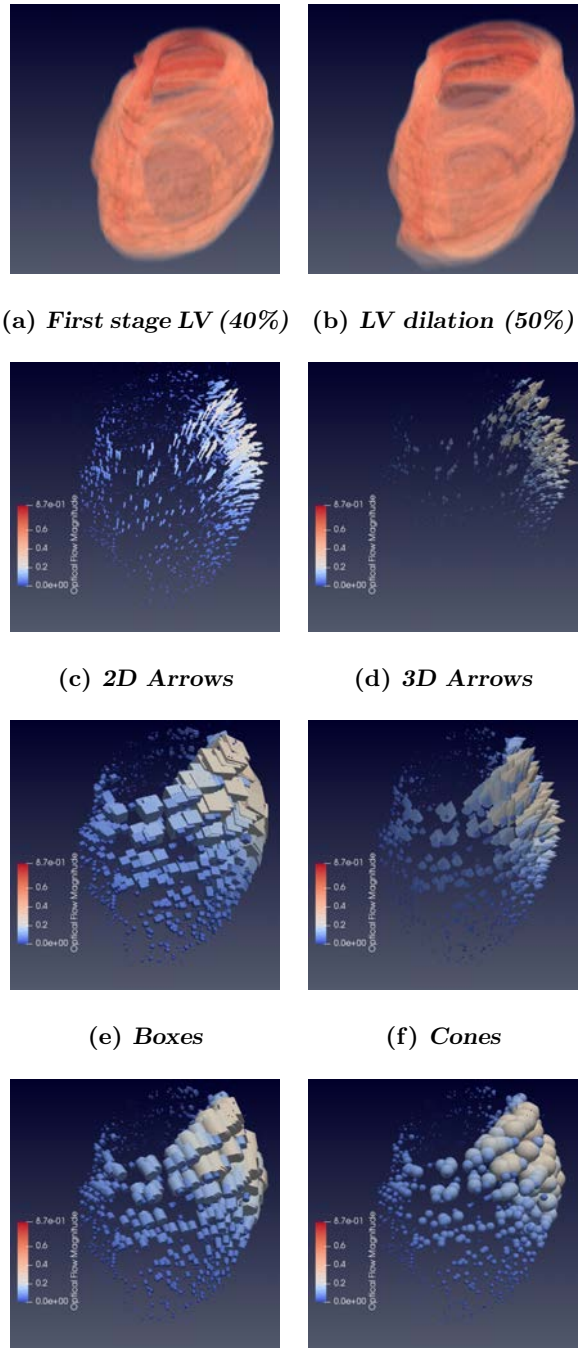

(a) ***First stage LV (40%)*** **(b)** ***LV dilation (50%)***

(c) ***2D Arrows*** **(d)** ***3D Arrows***

(e) ***Boxes*** **(f)** ***Cones***

(g) ***Cylinders*** **(h)** ***Spheres***

Figure B.4: The resulting optical flow estimation, of the cardiac dilation movement in the LV, represented in different ways.

Appendix C

Example of the calculation of Optical Flow using Lucas and Kanade Method

Below we show the step-by-step example of a result obtained using the Lucas & Kanade method.

Consider two synthetic images L^t at time t and L^{t+1} at time $t+1$ to determine the optical flow using the Lucas-Kanade method of a supposed object characterized by the intensity values 180. Let us use a neighborhood $\Omega = 3 \times 3$. Note that the region has moved one horizontal pixel to the right.

$$L^t = \begin{bmatrix} 0 & 0 & 0 & 0 & 0 & 0 & 0 \\ 0 & 0 & 0 & 0 & 0 & 0 & 0 \\ 0 & 0 & 180 & 180 & 180 & 0 & 0 \\ 0 & 0 & 180 & 180 & 180 & 0 & 0 \\ 0 & 0 & 180 & 180 & 180 & 0 & 0 \\ 0 & 0 & 0 & 0 & 0 & 0 & 0 \\ 0 & 0 & 0 & 0 & 0 & 0 & 0 \end{bmatrix} \qquad L^{t+1} = \begin{bmatrix} 0 & 0 & 0 & 0 & 0 & 0 & 0 \\ 0 & 0 & 0 & 0 & 0 & 0 & 0 \\ 0 & 0 & 0 & 180 & 180 & 180 & 0 \\ 0 & 0 & 0 & 180 & 180 & 180 & 0 \\ 0 & 0 & 0 & 180 & 180 & 180 & 0 \\ 0 & 0 & 0 & 0 & 0 & 0 & 0 \\ 0 & 0 & 0 & 0 & 0 & 0 & 0 \end{bmatrix}$$

According to the Eq. 3.29 it is necessary to calculate the directional derivatives L_x, L_y and L_t. Directional derivatives L_x and L_y are obtained by filtering the image L with the following kernel:

$$H_x = \begin{bmatrix} -1 & 0 & 1 \end{bmatrix} \qquad H_y = \begin{bmatrix} -1 & 0 & 1 \end{bmatrix}^T$$

The filtering is carried out proceeding row by row with the kernel H_x and column by column with the kernel H_y. Below is the result of filtering the third row of the image L, for this, we express both this row and the kernel in the form of a polynomial (p_1):

Third row:

$$p_1 = 0\ell^6 + 0\ell^5 + 180\ell^4 + 180\ell^3 + 180\ell^2 + 0\ell + 0$$

Kernel:

$$H_x = \ell^2 + 0\ell - 1$$

Multiplication:

$$p_1 H_s = 0\ell^8 + 0\ell^7 + 180\ell^6 + 180\ell^5 + 0\ell^4 - 180\ell^3 - 180\ell^2 + 0\ell + 0$$

Due to the manipulation of the polynomials, the dimension of the resulting polynomial has been increased by two. If we want to keep the size of the original image we must remove the terms of the extreme powers, that is, $0\ell^8$ and 0. In this way, the result is the one that appears in the third row of the resulting derived image L_x shown then.

$$L_x = \begin{bmatrix} 0 & 0 & 0 & 0 & 0 & 0 & 0 \\ 0 & 0 & 0 & 0 & 0 & 0 & 0 \\ 0 & 180 & 180 & 0 & -180 & -180 & 0 \\ 0 & 180 & 180 & 0 & -180 & -180 & 0 \\ 0 & 180 & 180 & 0 & -180 & -180 & 0 \\ 0 & 0 & 0 & 0 & 0 & 0 & 0 \\ 0 & 0 & 0 & 0 & 0 & 0 & 0 \end{bmatrix}; L_y = \begin{bmatrix} 0 & 0 & 0 & 0 & 0 & 0 & 0 \\ 0 & 0 & 180 & 180 & 180 & 0 & 0 \\ 0 & 0 & 180 & 180 & 180 & 0 & 0 \\ 0 & 0 & 0 & 0 & 0 & 0 & 0 \\ 0 & 0 & -180 & -180 & -180 & 0 & 0 \\ 0 & 0 & -180 & -180 & -180 & 0 & 0 \\ 0 & 0 & 0 & 0 & 0 & 0 & 0 \end{bmatrix}$$

The time derivative L_t, is calculated by the difference between L^{t+1} and L^t, that is, $L_t = L^{t+1} - L^t$

$$L_t = \begin{bmatrix} 0 & 0 & 0 & 0 & 0 & 0 & 0 \\ 0 & 0 & 0 & 0 & 0 & 0 & 0 \\ 0 & 0 & -180 & 0 & 0 & 180 & 0 \\ 0 & 0 & -180 & 0 & 0 & 180 & 0 \\ 0 & 0 & -180 & 0 & 0 & 180 & 0 \\ 0 & 0 & 0 & 0 & 0 & 0 & 0 \\ 0 & 0 & 0 & 0 & 0 & 0 & 0 \end{bmatrix}$$

After calculating the matrices L_x^2, L_y^2, L_xL_y, L_tL_x, L_tL_y, the results are shown below:

$$L_x^2 = 10^4 \begin{bmatrix} 0 & 0 & 0 & 0 & 0 & 0 & 0 \\ 0 & 0 & 0 & 0 & 0 & 0 & 0 \\ 0 & 3.24 & 3.24 & 0 & 3.24 & 3.24 & 0 \\ 0 & 3.24 & 3.24 & 0 & 3.24 & 3.24 & 0 \\ 0 & 3.24 & 3.24 & 0 & 3.24 & 3.24 & 0 \\ 0 & 0 & 0 & 0 & 0 & 0 & 0 \\ 0 & 0 & 0 & 0 & 0 & 0 & 0 \end{bmatrix} L_y^2 = 10^4 \begin{bmatrix} 0 & 0 & 0 & 0 & 0 & 0 & 0 \\ 0 & 0 & 3.24 & 3.24 & 3.24 & 0 & 0 \\ 0 & 0 & 3.24 & 3.24 & 3.24 & 0 & 0 \\ 0 & 0 & 0 & 0 & 0 & 0 & 0 \\ 0 & 0 & 3.24 & 3.24 & 3.24 & 0 & 0 \\ 0 & 0 & 3.24 & 3.24 & 3.24 & 0 & 0 \\ 0 & 0 & 0 & 0 & 0 & 0 & 0 \end{bmatrix}$$

$$L_xL_y = 10^4 \begin{bmatrix} 0 & 0 & 0 & 0 & 0 & 0 & 0 \\ 0 & 0 & 0 & 0 & 0 & 0 & 0 \\ 0 & 0 & 3.24 & 0 & -3.24 & 0 & 0 \\ 0 & 0 & 0 & 0 & 0 & 0 & 0 \\ 0 & 0 & -3.24 & 0 & 3.24 & 0 & 0 \\ 0 & 0 & 0 & 0 & 0 & 0 & 0 \\ 0 & 0 & 0 & 0 & 0 & 0 & 0 \end{bmatrix}$$

$$L_tL_x = 10^4 \begin{bmatrix} 0 & 0 & 0 & 0 & 0 & 0 & 0 \\ 0 & 0 & 0 & 0 & 0 & 0 & 0 \\ 0 & 0 & -3.24 & 0 & 0 & -3.24 & 0 \\ 0 & 0 & -3.24 & 0 & 0 & -3.24 & 0 \\ 0 & 0 & -3.24 & 0 & 0 & -3.24 & 0 \\ 0 & 0 & 0 & 0 & 0 & 0 & 0 \\ 0 & 0 & 0 & 0 & 0 & 0 & 0 \end{bmatrix}; L_tL_y = 10^4 \begin{bmatrix} 0 & 0 & 0 & 0 & 0 & 0 & 0 \\ 0 & 0 & 0 & 0 & 0 & 0 & 0 \\ 0 & 0 & -3.24 & 0 & 0 & 0 & 0 \\ 0 & 0 & 0 & 0 & 0 & 0 & 0 \\ 0 & 0 & 3.24 & 0 & 0 & 0 & 0 \\ 0 & 0 & 0 & 0 & 0 & 0 & 0 \\ 0 & 0 & 0 & 0 & 0 & 0 & 0 \end{bmatrix}$$

Taking each of the previous matrices as a reference and considering the neighborhood environment $\Omega = 3 \times 3$, we will proceed as follows. For each element the eight neighbors that surround it are considered:

$$\begin{bmatrix} 0 & 0 & 0 & 0 & 0 & 0 & 0 \\ 0 & 0 & 0 & 0 & 0 & 0 & 0 \\ 0 & 3.24 & 3.24 & 0 & 3.24 & 3.24 & 0 \\ 0 & 3.24 & 3.24 & 0 & 3.24 & 3.24 & 0 \end{bmatrix}$$

except in the elements of the first and last row and first and last column where only its five neighbors will be considered:

$$\begin{bmatrix} 0 & 0 & 0 & 0 & 0 & 0 & 0 \\ 0 & 0 & 0 & 0 & 0 & 0 & 0 \\ 0 & 3.24 & 3.24 & 0 & 3.24 & 3.24 & 0 \\ 0 & 3.24 & 3.24 & 0 & 3.24 & 3.24 & 0 \end{bmatrix}$$

Now, if the elements are corners, only their three neighbors are considered:

$$\begin{bmatrix} 0 & 0 & 0 & 0 & 0 & 0 & 0 \\ 0 & 0 & 0 & 0 & 0 & 0 & 0 \\ 0 & 3.24 & 3.24 & 0 & 3.24 & 3.24 & 0 \end{bmatrix}$$

Finishing to illustrate the above, and according to the previous figures where we take as reference the matrix L_x^2. So to obtain the sum associated with the element of the third row and second column we would have the following submatrix **a**, whose sum turns out to be 12.96, this value appearing in the same position of the resulting sum matrix. If we want to obtain the sum of the element of the third row first column we will have the submatrix **b**, whose sum turns out to be 6.48. Finally, to obtain the value of the element of the first row first column we would have the submatrix **c** with result of the sum 0.

$$\mathbf{a} = 10^4 \begin{bmatrix} 0 & 0 & 0 \\ 0 & 3.24 & 3.24 \\ 0 & 3.24 & 3.24 \end{bmatrix} \qquad \mathbf{b} = 10^4 \begin{bmatrix} 0 & 0 \\ 0 & 3.24 \\ 0 & 3.24 \end{bmatrix} \qquad \mathbf{c} = 10^4 \begin{bmatrix} 0 & 0 \\ 0 & 0 \end{bmatrix}$$

The resulting sum matrices are as follows:

$$\sum_\Omega L_x^2 = 10^4 \begin{bmatrix} 0 & 0 & 0 & 0 & 0 & 0 & 0 \\ 3.24 & 6.48 & 6.48 & 6.48 & 6.48 & 6.48 & 3.24 \\ 6.48 & 12.96 & 12.96 & 12.96 & 12.96 & 12.96 & 6.48 \\ 9.72 & 19.44 & 19.44 & 19.44 & 19.44 & 19.44 & 9.72 \\ 6.48 & 12.96 & 12.96 & 12.96 & 12.96 & 12.96 & 6.48 \\ 3.24 & 6.48 & 6.48 & 6.48 & 6.48 & 6.48 & 3.24 \\ 0 & 0 & 0 & 0 & 0 & 0 & 0 \end{bmatrix}$$

$$\sum_\Omega L_y^2 = 10^4 \begin{bmatrix} 0 & 3.24 & 6.48 & 9.72 & 6.48 & 3.24 & 0 \\ 0 & 6.48 & 12.96 & 19.44 & 12.96 & 6.48 & 0 \\ 0 & 6.48 & 12.96 & 19.44 & 12.96 & 6.48 & 0 \\ 0 & 6.48 & 12.96 & 19.44 & 12.96 & 6.48 & 0 \\ 0 & 6.48 & 12.96 & 19.44 & 12.96 & 6.48 & 0 \\ 0 & 6.48 & 12.96 & 19.44 & 12.96 & 6.48 & 0 \\ 0 & 3.24 & 6.48 & 9.72 & 6.48 & 3.24 & 0 \end{bmatrix}$$

$$\sum_\Omega L_x L_y = 10^4 \begin{bmatrix} 0 & 0 & 0 & 0 & 0 & 0 & 0 \\ 0 & 3.24 & 3.24 & 0 & -3.24 & -3.24 & 0 \\ 0 & 3.24 & 3.24 & 0 & -3.24 & -3.24 & 0 \\ 0 & 0 & 0 & 0 & 0 & 0 & 0 \\ 0 & -3.24 & -3.24 & 0 & 3.24 & 3.24 & 0 \\ 0 & -3.24 & -3.24 & 0 & 3.24 & 3.24 & 0 \\ 0 & 0 & 0 & 0 & 0 & 0 & 0 \end{bmatrix}$$

$$\sum_\Omega L_t L_x = -10^4 \begin{bmatrix} 0 & 0 & 0 & 0 & 0 & 0 & 0 \\ 0 & 3.24 & 3.24 & 3.24 & 3.24 & 3.24 & 3.24 \\ 0 & 6.48 & 6.48 & 6.48 & 6.48 & 6.48 & 6.48 \\ 0 & 9.72 & 9.72 & 9.72 & 9.72 & 9.72 & 9.72 \\ 0 & 6.48 & 6.48 & 6.48 & 6.48 & 6.48 & 6.48 \\ 0 & 3.24 & 3.24 & 3.24 & 3.24 & 3.24 & 3.24 \\ 0 & 0 & 0 & 0 & 0 & 0 & 0 \end{bmatrix}$$

$$\sum_\Omega L_t L_y = 10^4 \begin{bmatrix} 0 & 0 & 0 & 0 & 0 & 0 & 0 \\ 0 & -3.24 & -3.24 & -3.24 & 0 & 0 & 0 \\ 0 & -3.24 & -3.24 & -3.24 & 0 & 0 & 0 \\ 0 & 0 & 0 & 0 & 0 & 0 & 0 \\ 0 & 3.24 & 3.24 & 3.24 & 0 & 0 & 0 \\ 0 & 3.24 & 3.24 & 3.24 & 0 & 0 & 0 \\ 0 & 0 & 0 & 0 & 0 & 0 & 0 \end{bmatrix}$$

With the above matrices, we can solve the Eq. (3.29) for each of the pixels of the original reference image. The matrices corresponding to the horizontal ($\mathbf{U}$) and vertical ($\mathbf{V}$) components of the optical flow turn out to be the following:

$$\mathbf{U} = - \begin{bmatrix} 0 & 0 & 0 & 0 & 0 & 0 & 0 \\ 0 & 0.33 & 0.43 & 0.50 & 0.57 & 0.67 & 1 \\ 0 & 0.43 & 0.47 & 0.50 & 0.53 & 0.57 & 1 \\ 0 & 0.50 & 0.50 & 0.50 & 0.50 & 0.50 & 1 \\ 0 & 0.43 & 0.47 & 0.50 & 0.53 & 0.57 & 1 \\ 0 & 0.33 & 0.43 & 0.50 & 0.57 & 0.67 & 1 \\ 0 & 0 & 0 & 0 & 0 & 0 & 0 \end{bmatrix}$$

$$\mathbf{V} = - \begin{bmatrix} 0 & 0 & 0 & 0 & 0 & 0 & 0 \\ 0 & 0.33 & 0.14 & 0.17 & 0.14 & 0.33 & 0 \\ 0 & 0.29 & 0.13 & 0.17 & 0.13 & 0.29 & 0 \\ 0 & 0 & 0 & 0 & 0 & 0 & 0 \\ 0 & -0.29 & -0.13 & -0.17 & -0.13 & -0.29 & 0 \\ 0 & -0.33 & -0.14 & -0.17 & -0.14 & -0.33 & 0 \\ 0 & 0 & 0 & 0 & 0 & 0 & 0 \end{bmatrix}$$

These last two matrices are shown in figure 3.5 as the resulting optical flow (fig. 3.5(c)) of the synthetic figures 3.5(a) and 3.5(b).

Appendix D

Article: 3D Hermite Transform Optical Flow Estimation in Left Ventricle CT Sequences

On the next page, we attach the accepted and registered article [55] that relates to this research.

sensors

MDPI

Article

3D Hermite Transform Optical Flow Estimation in Left Ventricle CT Sequences

Carlos Mira [1,*], Ernesto Moya-Albor [2], Boris Escalante-Ramírez [1,*], Jimena Olveres [1], Jorge Brieva [2] and Enrique Vallejo [3]

1 Facultad de Ingeniería, Universidad Nacional Autónoma de México, Ciudad de México 04510, Mexico; jolveres@gmail.com
2 Facultad de Ingeniería, Universidad Panamericana, Augusto Rodin 498, Ciudad de Mexico 03920, Mexico; emoya@up.edu.mx (E.M.-A.); jbrieva@up.edu.mx (J.B.)
3 Centro Médico ABC, Ciudad de México 01120, Mexico; vallejo.enrique@gmail.com
* Correspondence: miragnlz@live.com (C.M.); boris@unam.mx (B.E.-R.)

Received: 22 November 2019; Accepted: 10 January 2020; Published: 21 January 2020

Abstract: Heart diseases are the most important causes of death in the world and over the years, the study of cardiac movement has been carried out mainly in two dimensions, however, it is important to consider that the deformations due to the movement of the heart occur in a three-dimensional space. The $3D + t$ analysis allows to describe most of the motions of the heart, for example, the twisting motion that takes place on every beat cycle that allows us identifying abnormalities of the heart walls. Therefore, it is necessary to develop algorithms that help specialists understand the cardiac movement. In this work, we developed a new approach to determine the cardiac movement in three dimensions using a differential optical flow approach in which we use the steered Hermite transform (SHT) which allows us to decompose cardiac volumes taking advantage of it as a model of the human vision system (HVS). Our proposal was tested in complete cardiac computed tomography (CT) volumes ($3D + t$), as well as its respective left ventricular segmentation. The robustness to noise was tested with good results. The evaluation of the results was carried out through errors in forwarding reconstruction, from the volume at time t to time $t + 1$ using the optical flow obtained (interpolation errors). The parameters were tuned extensively. In the case of the 2D algorithm, the interpolation errors and normalized interpolation errors are very close and below the values reported in ground truth flows. In the case of the 3D algorithm, the results were compared with another similar method in 3D and the interpolation errors remained below 0.1. These results of interpolation errors for complete cardiac volumes and the left ventricle are shown graphically for clarity. Finally, a series of graphs are observed where the characteristic of contraction and dilation of the left ventricle is evident through the representation of the 3D optical flow.

Keywords: bio-inspired computing; motion estimation; optical flow; differential method; steered hermite transform; cardiac CT imaging; algorithms

1. Introduction

Cardiovascular diseases (CVDs) take the lives of 17.9 million people every year, 31% of all global deaths, this represents the number one cause of death globally, more people die annually from CVDs than from any other cause [1]. Heart diseases as myocardial infarction, ischemia or hypertrophy can be characterized by analyzing the dynamics of the heart. During the cardiac cycle (contraction "systole" and relaxation "diastole" of the heart), the motion wall estimation can be used to recognize those pathologies. The acquisition of cardiac volumes has allowed quantifying relevant left ventricular (LV) parameters such as its volume, strain, twist, and desynchrony [2]. Nowadays, there are

diagnostic imaging techniques to characterize cardiac anatomy and function, as such echocardiography, cardiac Magnetic Resonance Imaging (MRI), cardiac Computed Tomography (CT), cardiac Positron Emission Tomography (PET), and coronary angiography [3]. Where the cardiac CT technique has certain advantages with respect other: a higher resolution that ultrasound, it is more accessible than MRI and it is a non-invasive a fast imaging option [4]. Cardiac CT allows acquiring three-dimensional morphological images, with motion artifacts minimizes, and showing the heart chambers and the coronary arteries at different planes [5]. It is then possible to acquire good quality cardiac CT data of the heartbeats. Images are acquired overall cardiac cycles to produce the final volume image. Due to the complexity of the heart motion, it is still hard for the physician to estimate the 3D motion during the exam, thus, it is necessary to develop computational analysis tools to aid in the diagnosis process.

The human heart is a complex organ in terms of anatomy and physiology, the estimation of its movement is an important task to understand its mechanism and to assist in the medical diagnosis. Different image processing techniques can be applied to calculate and to observe the motion of the heart, for example, the optical flow estimation is a method used in those situations where the correspondence between the pixels, within an image sequence, is required. The optical flow methods compute an approximation to the 2D motion in an image sequence from spatiotemporal patterns of image intensity [6]. Over the years, state-of-the-art algorithms for optical flow can be summarized in Nagel [7] who identified the common rigorous restrictions [8–10], as well as smoothing restrictions for the optical flow solution [7,11,12]. On the other hand, Barron et al. [6], categorized the optical flow in four groups: differential techniques [7–9,11,13,14], region-based matching [15,16], energy-based methods [17,18] and phase-based techniques [19]. Sun et al. [20] suggested that there have been few changes in the typical formulation given by Horn and Schunck [11]. Most of research work on optical flow has been carried out in $2D + t$. Many of them claim to be 3D, but they really are $2D + t$. Some of them, use 2D projections to obtain a 3D representation, in applications such as tracking traffic [21], in methods used for quantitative motion estimation of biological structures in light microscope [22], estimation of 3D geometry and 3D motion using spatiotemporal gradients [23] or emotion recognition from 3D videos [24]. 2D optical flow estimation has been used in the heart analysis to identify patients with some diseases, recent works using 2D optical flow cover topics such as motion estimation in cardiac fluorescence imaging [25], and as the automatic localization of the heart from cine MRI [26]. Some optical flow methods have used image models inspired by nature, for example Gabor filters [18,19,27–30]. The optical flow is fundamentally different than tracking because a complete set of correspondences between the pixel levels in an image (or volume) is obtained. The optical flow is used to calculate dense trajectories, provides more freedom and information about the data in which the movement is being estimated, a priori models are not needed and even more, it can also be used to develop deformable based-model tracking algorithms.

The Hermite transform (HT) has been an image model used to describe the local constraints of the Horn and Schunck approach. Liu et al. [27] derived a six-parameter non-affine optical flow model, which is solved with high-order Hermite polynomial filtered data. In [28], Silvan et al. showed that through a linear mapping of 3D Hermite coefficients by specific projection functions, we could obtain the Hermite transform coefficients of local projections. Furthermore, Moya et al. [29] used the steered Hermite coefficients like local motion restrictions, found in current methods, to define a differential estimation method.

One disadvantage of the 2D cardiac movement analysis is that it is constrained by geometry-dependent reference directions of deformation (i.e., radial, circumferential, and longitudinal). In this sense, a 3D cardiac movement analysis may overcome such limitations by referencing the intrinsic directions of deformation [31]. Thus, to identify altered ventricular function in patients with CVD, a 3D left ventricular (LV) deformation analysis is more suitable since it represents contributions from counter-directional, helically arranged fibers shortening and thickening throughout the cardiac cycle [32]. Research on the measurement of cardiac motion has been commonly made in $2D + t$ [33] but this analysis should be done in $3D + t$ to enable us to describe the true motions of the heart, for example,

the twisting motion that takes place on every beat cycle. Compared to the 2D analysis, the 3D analysis has not received much attention, although there are currently working groups analyzing optical flow in 3D mainly using ultrasound images.

About the estimation of 3D optical flow in general, some works have similarities with at least one of the aspects of this article, thereby, in [34] they use a 3D model of the human body and motion captured data to synthesize flow fields and train a convolutional neural network (CNN) to estimate human flow fields from pairs of images. In [35] a steerable filter-based algorithm is formulated, in its simplest form, for estimating 3D flow in sequences of volumetric or point-cloud data.

In [36] they present an approach for real-time respiratory motion estimation in image-guided interventions by employing contrast-invariant feature descriptors. Yoon et al. [37] presented a method for motion estimation applied to cone-beam CT, their work uses an energy functional, which includes as terms: a data fidelity, a regularization term, and the optical flow restriction. On the other hand, Jungwon et al. [38] used the optical flow estimation to calculate the local motion, allowing a 3D segmentation extension. Their model includes a shape distortion over time term, allowing segmenting and tracking the lung nodules. In [39], an implementation based on the optical flow algorithm from Farnebäck (2003) is used to create 3D freehand ultrasound but with reconstructions from 2D without external tracking, using deep learning.

Several methods have been used to estimate the optical flow of the endocardial wall motion [40]. In [41], a global anatomically constrained affine optical flow tracking was used to track the end-diastole left ventricle surface throughout the cardiac cycle. For [42], this approach first performs 3D segmentation at the end-diastolic frame and then performs tracking over the cardiac cycle using both global (optical flow) and local (block matching) methods. In [43] they claim to have a method for detecting cardiac flow in echocardiography where the sampling planes representing the mitral inflow tract and the left ventricle outflow tract are traced by fusing information from multiple cues, including optical flow, boundary detection, and motion prior. Duan et al. [44], evaluate a correlation-based optical flow algorithm for tracking endocardial surfaces on three-dimensional ultrasound data, also in [45] they built a truly 3D mathematical phantom of cardiac tissue and blood in order to validate the optical flow for quantification of myocardial deformations. Leung et al. [46] track left ventricular borders in 3D echocardiographic sequences by combining differential optical flow with statistical modeling. Zhiang et al. [47] developed an optical flow algorithm based on Thirion's diffusing model [48], also known as the "demons" algorithm and also described an atlas-based geometry pipeline for constructing three-dimensional cubic Hermite finite element meshes of the human heart.

In Table 1 we summarized some of the most recent optical flow motion methods used to extract the motion estimation, either using a $2D + t$ or $3D + t$ model, and the differences with the proposed method. In some cases, a 2D optical flow is initially estimated to map it onto a 3D optical flow.

The present article is an extension of our previous work published in [49]. In that work, we proposed the three-dimensional optical flow estimation using the 3D steered Hermite transform and we compared our approach with the 3D Horn-Schunck method. In contrast, the current work is compared with a multiresolution Horn and Schunck approach reported by Sun et al. [20], moreover, in this work, we perform a depth analysis about the optimal parameters of the method proposed and we focused the Section 5.2.1 to analyzed the 3D optical flow estimation of the left ventricle, first, showing its 3D segmentation and showing the advantages of our approach compared with the 3D version of the method of Sun et al. [20], and then, showing the 3D motion of the left ventricle in different cardiac cycle and a whole cardiac cycle, highlighting the corresponding contraction and relaxation movements present in each phase of the cardiac cycle. It should be mentioned that similar 2D algorithms using the Hermite transform have already been presented in [29,33] but with the main disadvantage of consuming a lot of computing time.

Table 1. $2D/3D+t$ optical flow estimation approaches.

Paper	OF Model ($2D/3D+t$)	Method	Application	Evaluation Metric
Proposed method	3D	Using the 3D Steered Hermite Transform	Left ventricle CT sequences	Interpolation errors in 3D
Ranjan et al. [34]	3D	A 3D model human body and a CNN	Estimate human flow fields	End point error
Alexiadis et al. [35]	2D	Minimizing a cost functional	3D flow estimation	Mean angular error on synthetic images
Queiros et al. [41]	3D	Anatomically affine optical flow	Left ventricle tracking	Distance and Dice metrics
Patil et al. [24]	2D	Farnebäck	Emotion recognition	Accuracy of 6 emotions
Saleh et al. [26]	2D	Lucas-Kanade	Heart Localization	Accuracy on localizing
Baghaie et al. [30]	2D	Gabor, Schmid and steerable filters	2D flow estimation	Angular and interpolation errors
Rodriguez et al. [25]	2D	Horn & Schunck	Cardiac motion estimation	Mean square error

Revising the algorithm from 2D to 3D is not a trivial problem, on top of the additional and necessary computational complexity, and the importance of describing the 3D cardiac movement. We have to describe (based on [50]) and calculate a second local orientation angle from the 3D cartesian coefficients of Hermite to obtain the 3D steered coefficients of Hermite (SHT3D). The data used in this work require a sensitivity analysis of its parameters and a way to validate the results because there aren't annotated volumes. Robust noise tests and calculation of interpolation errors of the volumes used had been carried out. Left ventricular analysis has been of great importance for this article. In this way, the results of the optical flow and the segmentation of such cardiac structure were evaluated.

Figure 1 shows an overview of the proposed method according to the procedures explained in the next sections.

Our approach uses a three-dimensional ($3D+t$), that is, it uses the data of the cardiac volumes in a three-dimensional space (x, y, z), which change over time during the entire cardiac cycle; a modified version of Sun et al. [20], which, in contradistinction of Horn and Schunck's approach [11], uses an incremental multiresolution technique to estimate large displacements, where the optical flow at a coarse level is extrapolated to warp the second image at a finer level, combined with the optical flow based on the Hermite transform proposed by Moya et al. [29], that uses the several constraints found in the more accurate optical flow methods. The rest of the paper is organized as follows: Section 2 describes the 3D Hermite transform, Section 3 develops the proposal to obtain 3D optical flow, Section 5 presents the experimental results and discussion of this work, Section 6 is about the results obtained, and finally, Section 7 concludes the paper and presents future work.

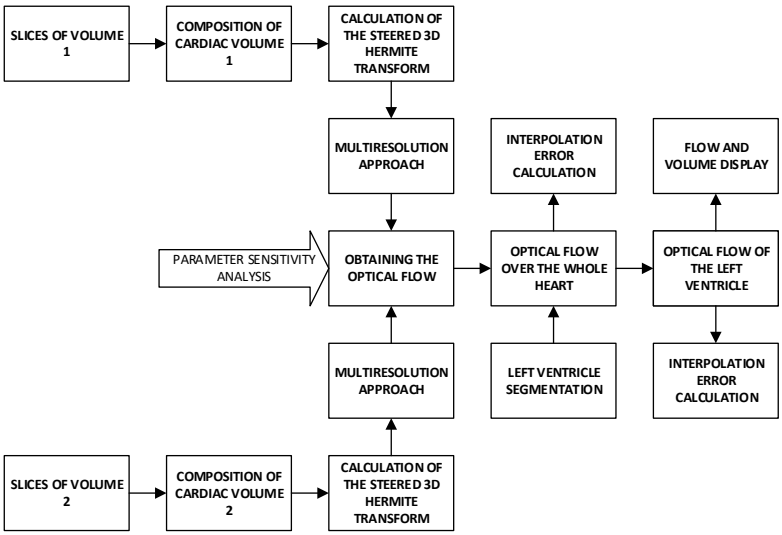

Figure 1. Overview of the proposed method.

2. The 3D Hermite Transform

The Hermite transform is a bio-inspired image model, it simulates some of the more relevant properties of the early vision of the human vision system (HVS): the local processing [51] and the Gaussian derivative model of the receptive fields [50,52,53]. The SHT provides a very efficient representation of oriented patterns which enables an adaptation to local orientation content at each window position over the image, indicating the direction of the two-dimensional pattern. The Hermite transform uses functions that are derivatives of Gaussians, which have wide applications in the field of computer vision and are a bio-inspired model of the human vision system. In this work, the Hermite transform serves as a theoretical framework to carry out the estimation of cardiac movement in our approach.

Gaussian windows in two dimensions have the property of being rotationally symmetric and spatially separable. Gaussian windows separated by twice the standard deviation, are a good model found for the receptive fields of perception found in psychological experiments [51]. According to the psychophysical model of HVS [52,54], through Gaussian windows, we can decompose an image into several orthogonal polynomials.

An interesting special case of 2D polynomial transforms arises when we have a window function which is separable i.e., $v(x,y) = v(x)v(y)$

For a perceptual standpoint and according to the scale-space theory, we will use a Gaussian window (Figure 2)

$$v(x,y) = \frac{1}{\sigma\sqrt{\pi}} \exp\left(-\frac{(x^2+y^2)}{2\sigma^2}\right) \quad (1)$$

The direct Hermite transform in 3D (HT3D), is a particular case of the proposal of Martens [50,53], where a signal is localized by an analysis window and this information is expanded using polynomials orthogonal to the window. Polynomials that are orthogonal with respect to the Gaussian window function are defined by [55], so we would use the window:

$$v(x,y,z) = \frac{1}{\sqrt{\sigma\sqrt{\pi}}} \exp\left(-\frac{(x^2+y^2+z^2)}{2\sigma^2}\right) \quad (2)$$

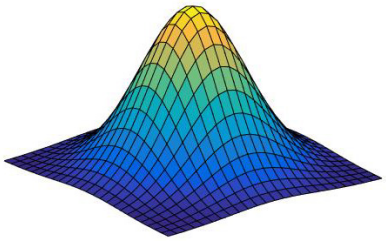

Figure 2. Gaussian window $v(x, y)$.

Physiological experiments consider using overlapping Gaussian windows separated by twice the standard deviation σ which are isotropic and that's why we can establish that $\sigma = \sigma_x = \sigma_y = \sigma_z$ in accordance with the overlapping receptive fields of the human visual system [51].

The Hermite cartesian coefficients, $L_{l,m-l,n-m}$, are obtained by convolution of the original signal $L(x, y, z)$ with the analysis filters $D_{l,m-l,n-m}(x, y, z)$ followed by subsampling on a three-dimensional mesh S using Equation (3):

$$L_{l,m-l,n-m}(x_0, y_0, z_0) = L(x, y, z) \otimes D_{l,m-l,n-m}(x, y, z), \tag{3}$$

where l, $(m - l)$ and $(n - m)$ denote the analysis order in x, y and z directions, respectively; $l = 0, 1, \ldots, m$; $m = 0, 1, \ldots, n$; $n = 0, 1, \ldots, N$; N is the maximum order of the expansion that is related to the size of a cubic window of $\mathcal{M} \times \mathcal{M} \times \mathcal{M}$, where $N \leq 2 * (\mathcal{M} - 1)$. For large values of $\mathcal{M}$ the discrete cubic kernel reduces to the 3D Gaussian window.

The three-dimensional Hermite filters can be represented by:

$$D_{l,m-l,n-m}(x, y, z) = G_{l.m-l,n-m}(-x, -y, -z)\, v^2(-x, -y, -z) \tag{4}$$

wich are separable because the Gaussian window is rotationally symmetric

$$D_{l,m-l,n-m}(x, y, z) = D_l(x) D_{m-l}(y) D_{n-m}(z) \tag{5}$$

and those can be computed by:

$$D_l(x) = \frac{(-1)^l}{\sqrt{2^l l!}} \frac{1}{\sigma\sqrt{\pi}} H_l\left(\frac{x}{\sigma}\right) \exp\left(-\frac{x^2}{\sigma^2}\right) \tag{6}$$

$G_{l,m-l,n-m}(x, y, z)$ are a family of polynomials defined as:

$$G_{l,m-l,n-m}(x, y, z) = \frac{1}{\sqrt{2^n l!(m-l)!(n-m)!}} H_l\left(\frac{x}{\sigma}\right) H_{m-l}\left(\frac{y}{\sigma}\right) H_{n-m}\left(\frac{z}{\sigma}\right) \tag{7}$$

where H_l represents the generalized Hermite polynomials given by Rodrigues' formula [56]

$$H_l(x) = (-1)^l \exp(x^2) \frac{d^l}{dx^l} \exp\left(-x^2\right) \tag{8}$$

The recovery process of the original image (inverse Hermite transform in 3D - IHT3D) consists of interpolating the Hermite coefficients through the proper synthesis filters:

$$\hat{L}(x, y, z) = \sum_{n=0}^{N} \sum_{m=0}^{n} \sum_{l=0}^{m} \sum_{(x_0, y_0, z_0) \in S} L_{l,m-l,n-m}(x_0, y_0, z_0)\, P_{l,m-l,n-m}(x - x_0, y - y_0, z - z_0) \tag{9}$$

where $P_{l,m-l,n-m}(x,y,z)$ can be determined by:

$$P_{l,m-l,n-m}(x,y,z) = \frac{G_{l,m-l,n-m}(x,y,z)v^2(x,y,z)}{\sum\limits_{(x_0,y_0,z_0)\in S} v^2(x-x_0,y-y_0,z-z_0)} \tag{10}$$

for $l = 0,...,m$; $m = 0,...,n$ and $n = 0,...,N$.

From Equation (9), instead of to recover the original volume we obtain an approximation of the original signal $\hat{L}(x,y,z)$, where the quality of this reconstruction improves by increasing the maximum order of the expansion N, i.e., the size of the cubic window $\mathcal{M}$ [50]. In terms of the artifacts in the approximated volume $\hat{L}(x,y,z)$, small values of the cubic windows causes "speckles", while high values result in Gibbs-phenomenon-like artifacts such as ringing and blur [57].

Thus, to determined the maximum order or the expansion N and in consequence the size of the cubic window $\mathcal{M}$, in [57] van Dijk and Martens determined that using an expansion of the Hermite transform equal to 3, the reconstructed 2D image will contain the most quantity of AC energy (84%) according to Parseval's theorem. In general, with $N \geq 3$ we can obtain a good reconstruction and with much greater values we will obtain a perfect reconstruction of the image.

3D Steered Hermite Transform

The Steered Hermite transform (SHT) is a variant of the HT that adapts to the local orientation of the image [57], it uses rotated filters which are represented as a linear combination of basis filters [58]. The orientation property of these steered Hermite filters is due to the symmetric-radial form of the Gaussian window, thus they can saw as the response of directional derivatives of the Gaussian function.

On the other hand, the SHT describes local 1D patterns in images into a smaller number of coefficients that represent the profile of the pattern perpendicular to its orientation [57].

By projecting the 3D Cartesian Hermite coefficients towards the local orientation angles θ and ϕ (Figure 3), we obtain the Steered Hermite transform in 3D (SHT3D) as shown in Equation (11):

$$l_{l,m-l,n-m,\theta,\phi}(x_0,y_0,z_0) = \sum_{m=0}^{n}\sum_{l=0}^{m}\left(L_{l,m-l,n-m}\left(x_0,y_0,z_0\right)\cdot g_{l,m-l}\left(\theta\right)\cdot g_{m,n-m}\left(\phi\right)\right) \tag{11}$$

where $l_{l,m-l,n-m,\theta,\phi}(x_0,y_0,z_0)$ are the 3D steered Hermite coefficients. And

$$g_{j,k-j}(\varphi) = \sqrt{\binom{k}{j}}\left(\cos^j\left(\varphi\right)\sin^{k-j}\left(\varphi\right)\right) \tag{12}$$

is the cartesian angular function that expresses the directional selectivity of the filter.

To calculate the direction of maximum energy we used the coefficients from Equation (3) and the phase of the gradient given by Equations (13) and (14):

$$\theta = \arctan\left(\frac{L_{010}}{L_{100}}\right) \tag{13}$$

$$\phi = \arctan\left(\frac{\sqrt{\left(L_{100}\right)^2+\left(L_{010}\right)^2}}{L_{001}}\right) \tag{14}$$

where $[L_{1,0,0}, L_{0,1,0}, L_{0,0,1}]\,(x,y,z)^\top$ are a good approximation of the 3D gradient through the Cartesian Hermite coefficients.

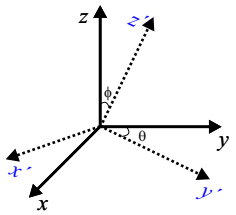

Figure 3. Cartesian coordinates (continuous line), steered coordinates (dotted line) and the angles θ and ϕ.

In order to graphically represent the indexes of the 3D Cartesian Hermite coefficients, Figure 4 shows the distribution of order two ($N = 2$) in each direction, in this case 27 coefficients are obtained for each voxel of a volume.

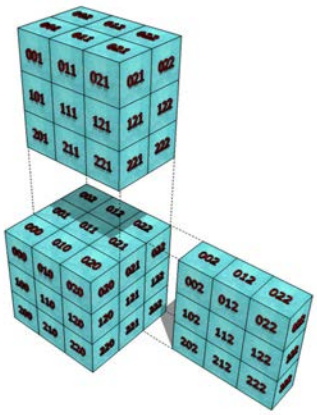

Figure 4. Distribution of the index of Cartesian Hermite coefficients of a second-order voxel.

Figure 5 shows an example of some 3D Steered Hermite coefficients for the left ventricle of a cardiac CT volume, according to Equation (11), where we can see the steered coefficients l_{000}, l_{100}, l_{010} and l_{001}.

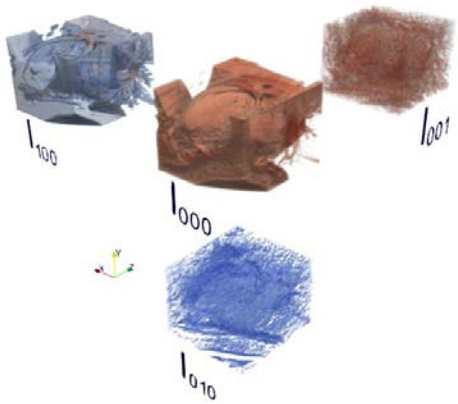

Figure 5. Ensemble of some Steered Hermite coefficients of a cardiac CT volume.

3. Optical Flow using the Hermite Transform

One of the main disadvantages of the classic method of Horn and Schunck [11] is its low accuracy, and because of this, we use a modified version of the method proposed by Sun et al. [20], that solves such obstacle using a multiresolution approach to estimate large displacements. In addition, this modified version is combined using the Hermite Transform with the advantage that it is based on a visual biological model of the images. Consequently, the local constraints of Horn and Schunck are defined using the zero order Hermite coefficient, and the Steered Hermite coefficients are used as high order local descriptors of the visual characteristics of the volumes.

Model

Our approach is based on the multiresolution Horn and Schunck approach reported by Sun et al. [20], it uses the SHT3D to expand the constant intensity constraint and adds the Steered Hermite coefficients constraint as shown in Equation (15):

$$\left[L_0\left(\mathbf{x}+\mathbf{w}\right)-L_0\left(\mathbf{x}\right)\right]+\gamma\left[\sum_{n=1}^{N} l_{n,\theta,\phi}\left(\mathbf{x}+\mathbf{w}\right)-\sum_{n=1}^{N} l_{n,\theta,\phi}\left(\mathbf{x}\right)\right]=0 \tag{15}$$

where $L\left(\mathbf{x}\right)$ is a volume sequence, with $\mathbf{x}=\left(x,y,z,t\right)^T$ representing the voxel location within a domain V; $\mathbf{w}:=\left(u,v,w,1\right)^T$ is a vector that defines the displacement u, v and w of each voxel at position (x,y,z) from time t to time $(t+1)$ in the directions x, y and z respectively; and γ is a weight parameter that controls the contribution of the high order descriptors. Using the HT optical flow restriction of Equation (15) we defined an energy functional that includes a smooth term to overcome the aperture problem [11] as follows:

$$\begin{aligned}\mathrm{E}=\int_V\Bigg(&\left[L_0(\mathbf{x})_0-L_0(\mathbf{x}+\mathbf{w}+d\mathbf{w})_1\right]^2+\\&\gamma\left[\sum_{n=1}^{N}\left\{l_{n,\theta,\phi}(\mathbf{x})_0-l_{n,\theta,\phi}(\mathbf{x}+\mathbf{w}+d\mathbf{w})_1\right\}\right]^2+\\&\alpha\left|\nabla\left(\mathbf{w}+d\mathbf{w}\right)\right|^2\Bigg)d\mathbf{x}\end{aligned} \tag{16}$$

where α is the weight value of the smoothness term that can get information from neighbors in regions where the intensity gradient is zero (uniform regions of flow).

To simplify the notation $L_{000}\left(\mathbf{x}\right)=L_0\left(\mathbf{x}\right)$, $L_*(\mathbf{x})_*$ is the Cartesian Hermite coefficient $*$ at time t and $L_*(\mathbf{x})_1$ is the Cartesian Hermite coefficient $*$ at time $t+1$.

Considering linear displacements, the constant intensity term of Equation (15) can be expanded by a Taylor series as shown:

$$\begin{aligned}L_0(\mathbf{x})_0-L_0(\mathbf{x}+\mathbf{w}+d\mathbf{w})_1\approx&L_0(\mathbf{x})_0-L_0(\mathbf{x}+\mathbf{w})_1-\\&du\frac{\partial L_0(\mathbf{x}+\mathbf{w})_1}{\partial x}-dv\frac{\partial L_0(\mathbf{x}+\mathbf{w})_1}{\partial y}-dw\frac{\partial L_0(\mathbf{x}+\mathbf{w})_1}{\partial z}\end{aligned} \tag{17}$$

A particular 1D cartesian Hermite coefficient can be obtained with the inner product between the signal located by the Gaussian window and the corresponding Hermite polynomial as follows [29]:

$$L_k=\left\langle L(x),H_k\left(\frac{x}{\sigma}\right)\right\rangle \tag{18}$$

Therefore, the spatial derivatives of the Hermite coefficients can be expressed as:

$$L_k=\frac{\partial^k L(x)}{\partial^k x} \tag{19}$$

Sensors **2020**, *20*, 595

for example, we can get the following simplified derivatives for x:

$$L_{100}\left(\mathbf{x}+\mathbf{w}\right)=L_{100}(\mathbf{x})_{\mathbf{w}}=\frac{\partial L_{000}(\mathbf{x}+\mathbf{w})_1}{\partial x} \tag{20}$$

$$l_{n,\theta,\phi,(m+1)}(\mathbf{x})_{\mathbf{w}}=\frac{\partial l_{n,\theta,\phi}(\mathbf{x}+\mathbf{w})_1}{\partial x} \tag{21}$$

also, we can define the temporal differences as:

$$L_0(\mathbf{x})_t=L_0(\mathbf{x}+\mathbf{w})_1-L_0(\mathbf{x})_0 \tag{22}$$

$$l_{n,\theta,\phi}(\mathbf{x})_t=l_{n,\theta,\phi}(\mathbf{x})_1-l_{n,\theta,\phi}(\mathbf{x}+\mathbf{w})_0 \tag{23}$$

then (17) can be written as

$$L_0(\mathbf{x})_0-L_0(\mathbf{x}+\mathbf{w}+d\mathbf{w})_1\approx-\left[L_0(\mathbf{x})_t+du\,L_{100}(\mathbf{x})_{\mathbf{w}}+dv\,L_{010}(\mathbf{x})_{\mathbf{w}}+dw\,L_{001}(\mathbf{x})_{\mathbf{w}}\right] \tag{24}$$

Finally, we can redefine the 3D Horn-Hermite optical flow (HOF3D) functional from Equation (16) as:

$$\begin{aligned}E\left(\mathbf{w}\right) &= \int_V\Bigg(-\left[L_0(\mathbf{x})_t+du\,L_{100}(\mathbf{x})_{\mathbf{w}}+dv\,L_{010}(\mathbf{x})_{\mathbf{w}}+dw\,L_{001}(\mathbf{x})_{\mathbf{w}}\right]^2\\ &-\gamma\sum_{n=1}^{N}\left[l_{n,\theta,\phi}(\mathbf{x})_t+du\;l_{n,\theta,\phi,(m+1)}(\mathbf{x})_{\mathbf{w}}+dv\;l_{n,\theta,\phi,(n+1)}(\mathbf{x})_{\mathbf{w}}+dw\;l_{n,\theta,\phi,(l+1)}(\mathbf{x})_{\mathbf{w}}\right]^2\\ &+\alpha\left|\nabla\left(\mathbf{w}+d\mathbf{w}\right)\right|^2\Bigg)\,d\mathbf{x}\end{aligned} \tag{25}$$

Minimizing $E\left(\mathbf{w}\right)$ with respect to u, v and w we obtain the following equation system:

$$\begin{aligned}&-2\Big(L_0(\mathbf{x})_t+du\,L_{100}(\mathbf{x})_{\mathbf{w}}+dv\,L_{010}(\mathbf{x})_{\mathbf{w}}+dw\,L_{001}(\mathbf{x})_{\mathbf{w}}\Big)L_{100}(\mathbf{x})_{\mathbf{w}}\\ &-2\gamma\sum_{n=1}^{N}\Big(l_{n,\theta,\phi}(\mathbf{x})_t+du\;l_{n,\theta,\phi,(m+1)}(\mathbf{x})_{\mathbf{w}}+dv\;l_{n,\theta,\phi,(n+1)}(\mathbf{x})_{\mathbf{w}}+dw\;l_{n,\theta,\phi,(l+1)}(\mathbf{x})_{\mathbf{w}}\Big)l_{n,\theta,\phi,(m+1)}(\mathbf{x})_{\mathbf{w}}\\ &+2\alpha\left|\nabla\left(u+du\right)\right|=0\end{aligned} \tag{26}$$

$$\begin{aligned}&-2\Big(L_0(\mathbf{x})_t+du\,L_{100}(\mathbf{x})_{\mathbf{w}}+dv\,L_{010}(\mathbf{x})_{\mathbf{w}}+dw\,L_{001}(\mathbf{x})_{\mathbf{w}}\Big)L_{010}(\mathbf{x})_{\mathbf{w}}\\ &-2\gamma\sum_{n=1}^{N}\Big(l_{n,\theta,\phi}(\mathbf{x})_t+du\;l_{n,\theta,\phi,(m+1)}(\mathbf{x})_{\mathbf{w}}+dv\;l_{n,\theta,\phi,(n+1)}(\mathbf{x})_{\mathbf{w}}+dw\;l_{n,\theta,\phi,(l+1)}(\mathbf{x})_{\mathbf{w}}\Big)l_{n,\theta,\phi,(n+1)}(\mathbf{x})_{\mathbf{w}}\\ &+2\alpha\left|\nabla\left(v+dv\right)\right|=0\end{aligned} \tag{27}$$

$$\begin{aligned}&-2\Big(L_0(\mathbf{x})_t+du\,L_{100}(\mathbf{x})_{\mathbf{w}}+dv\,L_{010}(\mathbf{x})_{\mathbf{w}}+dw\,L_{001}(\mathbf{x})_{\mathbf{w}}\Big)L_{001}(\mathbf{x})_{\mathbf{w}}\\ &-2\gamma\sum_{n=1}^{N}\Big(l_{n,\theta,\phi}(\mathbf{x})_t+du\;l_{n,\theta,\phi,(m+1)}(\mathbf{x})_{\mathbf{w}}+dv\;l_{n,\theta,\phi,(n+1)}(\mathbf{x})_{\mathbf{w}}+dw\;l_{n,\theta,\phi,(l+1)}(\mathbf{x})_{\mathbf{w}}\Big)l_{n,\theta,\phi,(l+1)}(\mathbf{x})_{\mathbf{w}}\\ &+2\alpha\left|\nabla\left(w+dw\right)\right|=0\end{aligned} \tag{28}$$

Rewriting the equation system of (26), (27) and (28) in matrix form we get:

$$\begin{bmatrix}A_1 & A_2 & A_3\\ A_4 & A_5 & A_6\\ A_7 & A_8 & A_9\end{bmatrix}\begin{bmatrix}du\\ dv\\ dw\end{bmatrix}=\begin{bmatrix}b_1\\ b_2\\ b_3\end{bmatrix} \tag{29}$$

where

$$A_1=L_{100}^2(\mathbf{x})_{\mathbf{w}}+\gamma\sum_{n=1}^{N}l_{n,\theta,\phi,(m+1)}^2(\mathbf{x})_{\mathbf{w}}$$

$$A_2=L_{100}(\mathbf{x})_{\mathbf{w}}L_{010}(\mathbf{x})_{\mathbf{w}}+\gamma\sum_{n=1}^{N}l_{n,\theta,\phi,(m+1)}(\mathbf{x})_{\mathbf{w}}\cdot l_{n,\theta,\phi,(n+1)}(\mathbf{x})_{\mathbf{w}}$$

$$A_3 = L_{100}(\mathbf{x})_{\mathbf{w}} L_{001}(\mathbf{x})_{\mathbf{w}} + \gamma \sum_{n=1}^{N} l_{n,\theta,\phi,(n+1)}(\mathbf{x})_{\mathbf{w}} \cdot l_{n,\theta,\phi,(l+1)}(\mathbf{x})_{\mathbf{w}}$$

$$b_1 = L_0(\mathbf{x})_t L_{100}(\mathbf{x})_{\mathbf{w}} + \gamma \sum_{n=1}^{N} l_{n,\theta,\phi}(\mathbf{x})_t \cdot l_{n,\theta,\phi,(m+1)}(\mathbf{x})_{\mathbf{w}} - \alpha \left| \nabla (u + du) \right|$$

$$A_4 = L_{010}(\mathbf{x})_{\mathbf{w}} L_{100}(\mathbf{x})_{\mathbf{w}} + \gamma \sum_{n=1}^{N} l_{n,\theta,\phi,(n+1)}(\mathbf{x})_{\mathbf{w}} \cdot l_{n,\theta,\phi,(m+1)}(\mathbf{x})_{\mathbf{w}}$$

$$A_5 = L^2_{010}(\mathbf{x})_{\mathbf{w}} + \gamma \sum_{n=1}^{N} l^2_{n,\theta,\phi,(n+1)}(\mathbf{x})_{\mathbf{w}}$$

$$A_6 = L_{010}(\mathbf{x})_{\mathbf{w}} L_{001}(\mathbf{x})_{\mathbf{w}} + \gamma \sum_{n=1}^{N} l_{n,\theta,\phi,(m+1)}(\mathbf{x})_{\mathbf{w}} \cdot l_{n,\theta,\phi,(l+1)}(\mathbf{x})_{\mathbf{w}}$$

$$b_2 = L_0(\mathbf{x})_t L_{010}(\mathbf{x})_{\mathbf{w}} + \gamma \sum_{n=1}^{N} l_{n,\theta,\phi}(\mathbf{x})_t \cdot l_{n,\theta,\phi,(n+1)}(\mathbf{x})_{\mathbf{w}} - \alpha \left| \nabla (v + dv) \right|$$

$$A_7 = L_{001}(\mathbf{x})_{\mathbf{w}} L_{100}(\mathbf{x})_{\mathbf{w}} + \gamma \sum_{n=1}^{N} l_{n,\theta,\phi,(l+1)}(\mathbf{x})_{\mathbf{w}} \cdot l_{n,\theta,\phi,(m+1)}(\mathbf{x})_{\mathbf{w}}$$

$$A_8 = L_{001}(\mathbf{x})_{\mathbf{w}} L_{010}(\mathbf{x})_{\mathbf{w}} + \gamma \sum_{n=1}^{N} l_{n,\theta,\phi,(l+1)}(\mathbf{x})_{\mathbf{w}} \cdot l_{n,\theta,\phi,(n+1)}(\mathbf{x})_{\mathbf{w}}$$

$$A_9 = L^2_{001}(\mathbf{x})_{\mathbf{w}} + \gamma \sum_{n=1}^{N} l^2_{n,\theta,\phi,(l+1)}(\mathbf{x})_{\mathbf{w}}$$

$$b_3 = L_0(\mathbf{x})_t L_{001}(\mathbf{x})_{\mathbf{w}} + \gamma \sum_{n=1}^{N} l_{n,\theta,\phi}(\mathbf{x})_t \cdot l_{n,\theta,\phi,(l+1)}(\mathbf{x})_{\mathbf{w}} - \alpha \left| \nabla (w + dw) \right|$$

Finally, in each lower-resolution level, the increment $d\mathbf{w}$ is estimated and, $\mathbf{w}$ is updated in the next high-resolution level.

In this work, we take advantage of the characteristics of the Hermite multiresolution transform, which makes it possible to improve spatial frequency locations and facilitate the analysis of local orientations at different scales [59,60]. Likewise, the HOF3D functional of Equation (25) can calculate small displacements du, dv, dw and propagate the solution to higher resolution levels. For each resolution level, an iterative method for solving linear equations was carried out.

4. Materials and Overview of the Method

4.1. Dataset Description

The dataset used in this work consists of two cardiac computed tomography studies ($3D + t$). The CT volumes were obtained in a 16-slice tomograph (at 120 kVp @ 900 mA) built with 128 detectors. The dimensions of each volume are $512 \times 512 \times 10$ at 12 bits per pixel. The clinical protocol starts by injected a contrast agent to the patient and the study is carried out in synchrony with the electrocardiogram (ECG) signal. A cardiac CT volume used is shown in Figure 6.

It should be noted that the acquisition of cardiac images are performed in connection with the electrocardiogram and are acquired with the patient in respiratory apnea to avoid artifice by movement.

4.2. Ethical Approval

The Research Committee of Engineering Faculty of Universidad Nacional Autonóma de México approved this research protocol. This study was conducted in accordance with the Declaration of Helsinki.

Sensors **2020**, *20*, 595

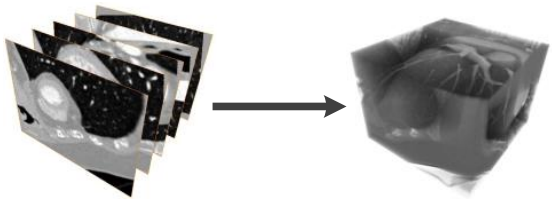

Figure 6. Cardiac CT images, slices and volume.

4.3. Overview of the Method

In Figure 7 we show an overview of our proposal. First, we have the cardiac volume slices, belonging to two consecutive steps of the cardiac cycle considered, which make up volume 1 and volume 2 respectively; for each volume, we obtain a multiresolution expansion related to the coefficients of the steered Hermite transform. Such coefficients are used to carry out the calculation of the optical flow within the mentioned HOF3D approach. Once the vector field belonging to the optical flow over the whole cardiac volume was obtained, we used the portion of the volume related to the segmented left ventricle to finally obtain only the masked vectors with this part of the cardiac volume.

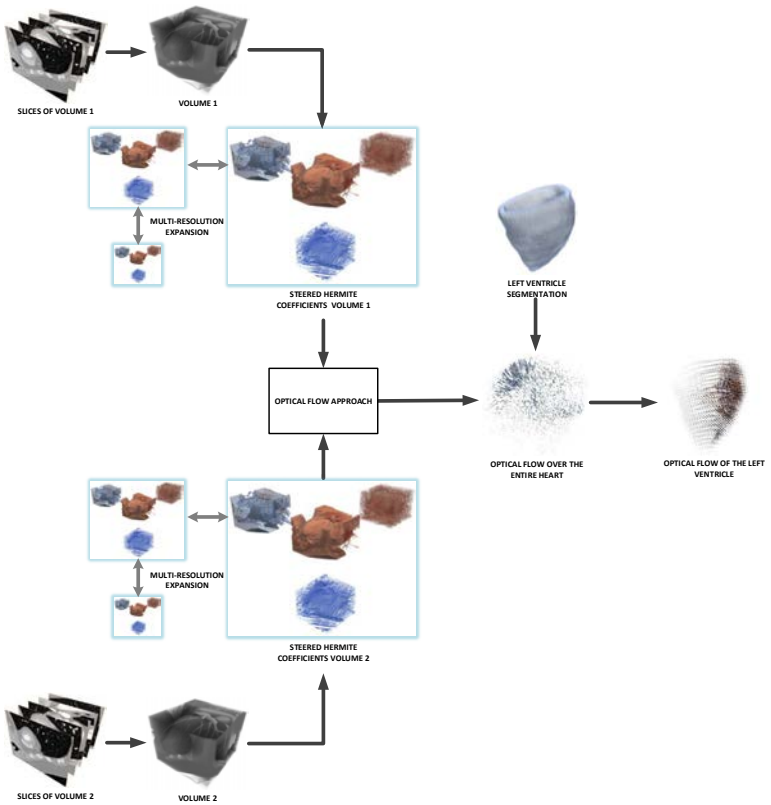

Figure 7. Procedure to implement the HOF3D approach.

5. Experiments and Results

This section presents the results of the estimation of the optical flow with the proposed method. In our previous work [49], we use some synthetic volumes to check the expected results, in this work, dozens of cardiac volumes corresponding to medical CT images, as well as their respective segmentation of the left ventricle, were used.

The section is divided into two stages, a validation stage and a stage of 3D optical flow results of the left ventricle. In the first stage, we performed a validation of our approach, where the optimal parameters both in the Hermite transform and the 3D optical flow proposal were determined. Then, the optical flow results in 2D were compared with a set of images ground-truth and a pair of algorithms of optical flow. The optical flow results in 3D were compared with the modified and multiresolution method of Horn and Schunck [20]. Next, an analysis of robustness to noise was performed. In the second stage, the 3D optical flow results in the left ventricle, which was previously segmented, are shown and the corresponding errors of interpolation are evaluated.

The results obtained on a PC Intel(R) Core(TM) i7-4710HQ CPU running at 2.50 GHz with 16 GB of RAM have an algorithm time-consuming of 4.8 h on 4 cores, nevertheless, this can be reduced to an average of 4.5 min with parallel computing and additional cores. The optical flow in our method has good scalability, close to linear speedup, which allows us to significantly reduce processing time. The results concerning processing time are consistent with those reported in [61]. They tested two differential algorithms, Lucas-Kanade and Horn-Schunck in $3D + t$, as we have also done.

5.1. Validation

In absence of a 3D motion ground-truth in CT images, which is used to evaluate the accuracy of the optical flow estimation, we validate our proposal in two different ways, first, by calculating a forward reconstruction using the volume $L(\mathbf{x}, t)$ at time t and the 3D optical flow obtained and second, comparing our 2D approach with other methods and using a 2D dataset with known ground-truth. In both cases, we used the interpolation error, which is defined as the root mean-square (RMS) difference between the known volume $L(\mathbf{x}, t+1)$ at time $t+1$ and the reconstructed volume $L_{GT}(\mathbf{x}, t+1)$, is calculated [6,19] as we showed in the Equation (30):

$$IE_{3D} = \left[\frac{1}{M} \sum_{\mathbf{x}} \Big(L(\mathbf{x}, t+1) - L_{GT}(\mathbf{x}, t+1) \Big)^2 \right]^{\frac{1}{2}} \tag{30}$$

where M is the number of voxels.

We also computed a second measure of interpolation performance, the normalized interpolation error between an interpolated volume $L(\mathbf{x}, t+1)$ and a ground-truth volume $L_{GT}(\mathbf{x}, t+1)$, which is given as in [62]:

$$NE_{3D} = \left[\frac{1}{M} \sum_{\mathbf{x}} \frac{\Big(L(\mathbf{x}, t+1) - L_{GT}(\mathbf{x}, t+1) \Big)^2}{\Big\| \nabla L_{GT}(\mathbf{x}, t+1) \Big\|^2 + \varepsilon} \right]^{\frac{1}{2}} \tag{31}$$

that represents a gradient-normalized RMS error, where ε is a scaling constant (e.g., $\varepsilon = 1$).

The interpolation errors are useful to know how good the calculation of the optical flow is when there is no available ground truth flow, the normalized interpolation error has the additional advantage of being normalized with respect to the magnitudes of the intensity changes that the volume of the reference.

5.1.1. Hermite Transform Parameter Tuning

Although the constants, values and weight parameters are difficult to select, in Section 2, we present which are the suitable values to the cubic window and in consequence, the maximum

expansion order N of the Hermite transform, thus, experimentally found that we achieved a good estimation of optical flow results ($NE_{3D} < 0.1$) and avoiding blur artifacts for our dataset with: a cubic window of $5 \times 5 \times 5$ pixels, i.e., a maximum expansion order of $N = 4$ for the SHT and 5 levels of multiresolution decomposition for the SHT. Below these values, we would obtain errors 2.5 to 3 times larger than those reported. It should be noted that this strategy allows us to handle large displacements, which occur from one step to another in a cardiac cycle. On the other hand, the number of iterations greater than 50 is the one that gives us the required numerical convergence according to our tests.

5.1.2. Optical Flow Parameter Sensitivity Analysis

As a first experiment, we perform a parameter sensitivity analysis to find the best values. Weight parameter γ of the HOF3D functional Equation (16) is used to weigh the contribution of the high order Hermite coefficients in those regions where the intensity does not remain constant from one volume to another. On the other hand, the softness parameter α can help recover the motion information from their neighbors in those regions where the gradient is zero, e.g., intensity homogeneous regions. It is carried out through averages from structures with high frequencies, e.g., edges and textures. Large values of α give us a smoother flow but this is relatively less important at locations with high image gradients than elsewhere.

For determining the values of the smoothness weight α and the weight parameter γ, first we compute the 3D optical flow over the cardiac CT sequences and then we analyze the behavior of the Interpolation Error (IE) and Normalized Interpolation Error (NE) metrics.

From Figure 8, the curves show that the best results for IE and NE are for $\alpha \geq 10$ and $\gamma \geq 100$ (bottom of the mesh).

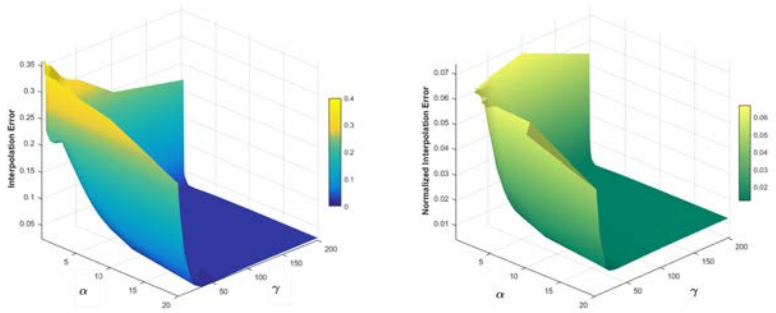

(**a**) (**b**)

Figure 8. Interpolation Error (**a**) and Normalized Interpolation Error (**b**), for parameter sensitivity analysis.

5.1.3. 2D Interpolation Errors

As we mentioned before, because we do not have a set of 3D optical flow to compare our results, as second experiment, we evaluate the performance of our 2D proposal, through a collection of well-known images. These images and their respective ground-truth optical flows can be found through [63], which still have great use and relevance today. They defined sequences with non-rigid movements where the optical flow was determined following a hidden fluorescent texture.

Table 2 shows the calculation of the interpolation error (Equation (30)) but in 2D. We choose a set of five data. HOF2D is the Horn-Hermite optical flow in 2D approach. We compare our HOF2D algorithm, along with another pair of algorithms and the ground-truth flows provided in [63]. The parameters

used for HOF2D are the same as those described in Sections 5.1.1 and 5.1.2, $N = 4$, 5 levels of multiresolution decomposition for the SHT in 2D, $\alpha \geq 10$ and $\gamma \geq 100$, except that the necessary iterations, which can range from 20, to provide the best results. The best results are highlighted in bold and, although our approach is not always the best, it is close to the best results in each case.

Table 2. Interpolation Error Calculation.

Ground Truth Images	Ground Truth Flow	Horn-Schunck [64]	Farnebäck [64]	HOF2D
dimetrodon	2.641	8.589	3.127	**2.865**
groove2	10.439	23.492	8.831	**10.353**
groove3	19.401	32.351	**15.703**	17.460
urban3	9.870	17.727	9.489	**8.122**
venus	8.813	20.659	**5.847**	8.835

With the same set of data and algorithms as Table 2, Table 3 presents the calculation of the normalized interpolation error in 2D based on (Equation (31)). The best performances are highlighted in bold and most of them are in the HOF2D column. We must remember that the normalized interpolation error is is a weighted RMS average of the pixels, wich use the image gradient as a weight factor. The normalized interpolation error compensates for the difference between the interpolation errors and the flow obtained because it gives less weight to the discontinuous regions and more weight to the regions without texture.

Table 3. Normal Interpolation Error Calculation.

Ground Truth Images	Ground Truth Flow	Horn-Schunck [64]	Farnebäck [64]	HOF2D
dimetrodon	0.207	0.546	0.382	**0.270**
groove2	0.418	0.860	0.385	**0.329**
groove3	0.990	1.622	0.626	**0.532**
urban3	2.325	2.452	1.342	**0.700**
venus	0.801	1.376	0.434	**0.348**

5.1.4. 3D Interpolation Errors

To evaluate the accuracy of the HOF3D method, we compared it with the 3D variant of the method of Sun et al. [20] We calculated the corresponding interpolation errors (IE and NE) using both proposals. Figure 9 presents a diagram of the steps to calculate the interpolation errors.

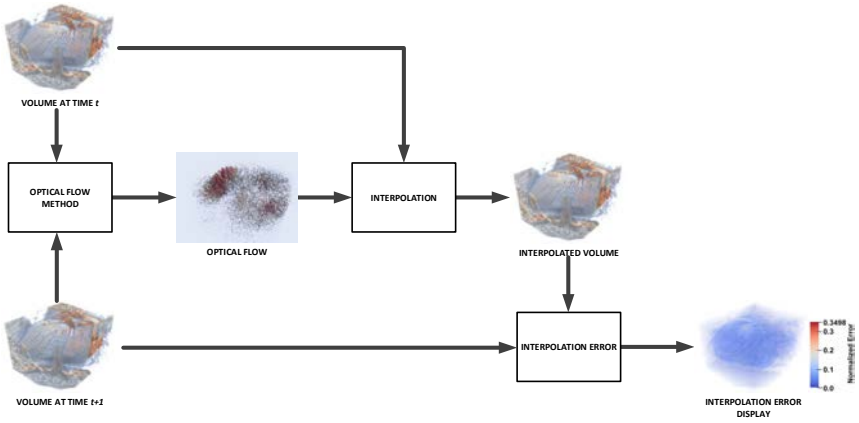

Figure 9. Steps to calculate and visualize the Interpolation Error.

Figure 10 shows a cardiac CT volume where we can observe the original volume (Figure 10a), the interpolated volume (Figure 10b), the difference between the original volume and its interpolated result (Figure 10c) using the 3D variant of the method of Sun et al. [20]. The results were compared with a modified version of the Sun method in 3D and for different noise levels. Both algorithms used were optimized and the evaluation of the results was carried out by means of a forward reconstruction, from the volume at time t to time $t+1$, through the 3D optical flow obtained. The interpolation error display is a visualization of the terms within the summation in Equation (31).

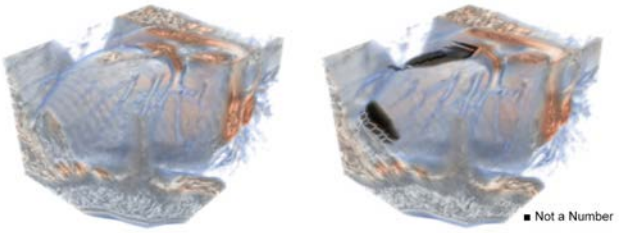

(**a**) Original Volume

(**b**) Volume Interpolated using the Horn and Schunck method

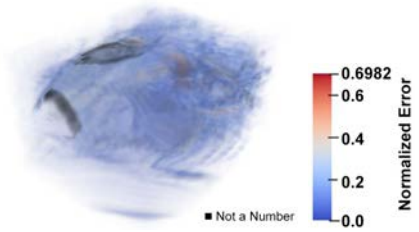

(**c**) Error between Original and Interpolated Volumes using the Horn and Schunck method

Figure 10. A cardiac CT volume showing the original volume, the interpolated volume using the 3D variant of the method of Sun et al. [20] and the error between the original volume and its interpolated result.

On the other hand, in order to compare our method, in Figure 11 we show the same cardiac CT volume as in Figure 10 where, again, we can observe the original volume (Figure 11a), the interpolated volume (Figure 11b), the difference between the original volume and its interpolated result (Figure 11c) using our HOF3D method.

In Figure 12, we show the interpolation errors obtained using the Sun et al. [20] and the HOF3D methods through the whole cardiac cycle (0% to 90%) for two CT sequences. In both sequences, we can observe the beginning of the increase in the interpolation error from 20% to 30%, when the contraction movement occurs and from 50% to 60% of the cardiac cycle, in full dilation movement. This is where we have a couple of cardiac movements of greater magnitude.

We can observe in the plots of Figure 12, both for the interpolation error and the normalized interpolation error, that even in each of the stages of the complete cardiac cycle, the HOF3D method gives better results and lower errors are obtained.

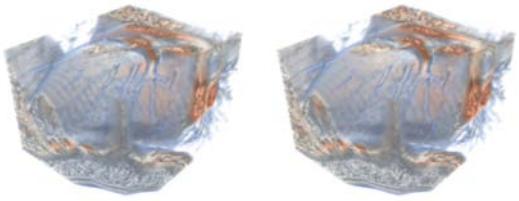

(**a**) Original Volume (**b**) Volume Interpolated using the HOF3D method

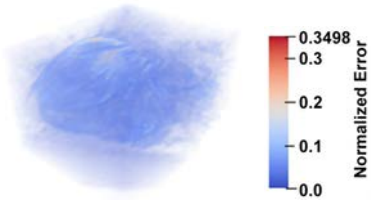

(**c**) Error between Original and Interpolated Volumes using HOF3D method

Figure 11. A cardiac CT volume showing the original volume, the Interpolated Volume using the HOF3D method and the error between the original volume and its interpolated result.

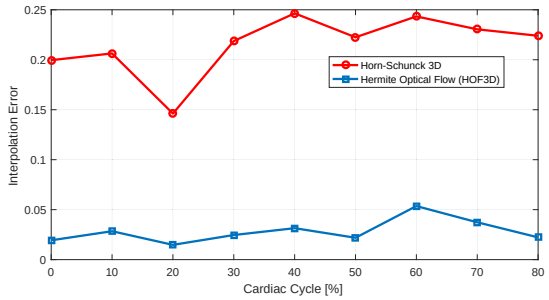

(**a**) Interpolation Error

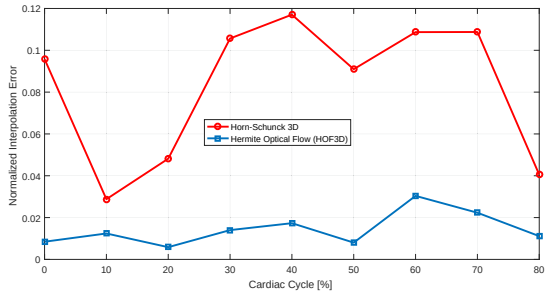

(**b**) Normalized Interpolation Error

Figure 12. Interpolation Error and Normalized Interpolation Error. For the 3D Horn-Schunck (red dashed line) and Hermite Optical Flow in 3D (blue solid line) methods. From sequences of cardiac CT volumes.

5.1.5. Robustness to Noise

As final experiment, we carried out an analysis of robustness to noise of the proposed method. For this, we added Gaussian noise, with different standard deviations ($\sigma_n = 0, 5, 10, 15, 20, 30$) and zero mean, to the cardiac volumes. In Figure 13 we can see one of the volumes used for the test, with three different values of σ_n.

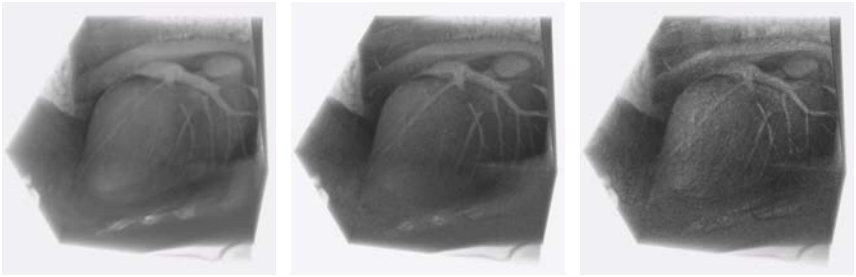

(a) Volume without noise **(b)** Volume with noise, ($\sigma_n = 10$) **(c)** Volume with noise, ($\sigma_n = 30$)

Figure 13. Volume with pseudo-random noise.

Table 4 shows the interpolation error and the normalized interpolation error for the noise levels given for the HOF3D method, using optimized parameters $\alpha = 10$, $\gamma = 100$ and $N = 4$. We can observe that although the standard deviation of the introduced noise grows, the interpolation error and the normalized interpolation error remain small, this is because the coefficient of order 0 of the Hermite transform $L_{000}(\mathbf{x})$ (Equations (3), (11) and (16)), contains a smoothed version of the original volume and this DC coefficient allows to reduce any component of high-frequency noise, additionally, in our approach, the steered Hermite coefficients use Gaussian derivatives, which incorporate information from neighboring voxels in the structure of cardiac volumes, which makes the proposed algorithm more robust to this type of noise [13,65]. By the other hand, it should be noted that although the errors are low, the addition of noise represents an increase in the interpolation error of 71.4% and for the normalized interpolation error of 80%, comparing one test without noise and the other test with noise of $\sigma_n = 30$.

Table 4. Interpolation Error and Normalized Interpolation Error computed for a cardiac volume with several standard deviations σ_n of Gaussian noise.

Gaussian Noise (σ_n)	Interpolation Error	Normalized Interpolation Error
0	0.03190	0.01696
5	0.03499	0.01954
10	0.03778	0.02168
15	0.04295	0.02563
20	0.04597	0.02779
30	0.05468	0.03387

5.2. 3D Optical Flow Results

In this section, we show the 3D optical flow estimation computed on CT volumes for a whole cardiac cycle. For descriptive purposes, only some representative parts of such a cardiac cycle are shown. In most cases, the display of the magnitudes of the optical flows was exaggerated in order to observe the qualitative characteristics of the movements.

Figure 14 shows the results of a 3D Optical flow of two cardiac CT volumes computed at phases 20-30% (when a contraction movement occurs) using the HOF3D method. Figure 14a,b show two phases of the cardiac cycle of volume (for better viewing a cut of that volume was made).

Figure 14c,d show the same phases of volume along with the three-dimensional optical flow field. Finally, Figure 14e,f illustrate only the optical flow.

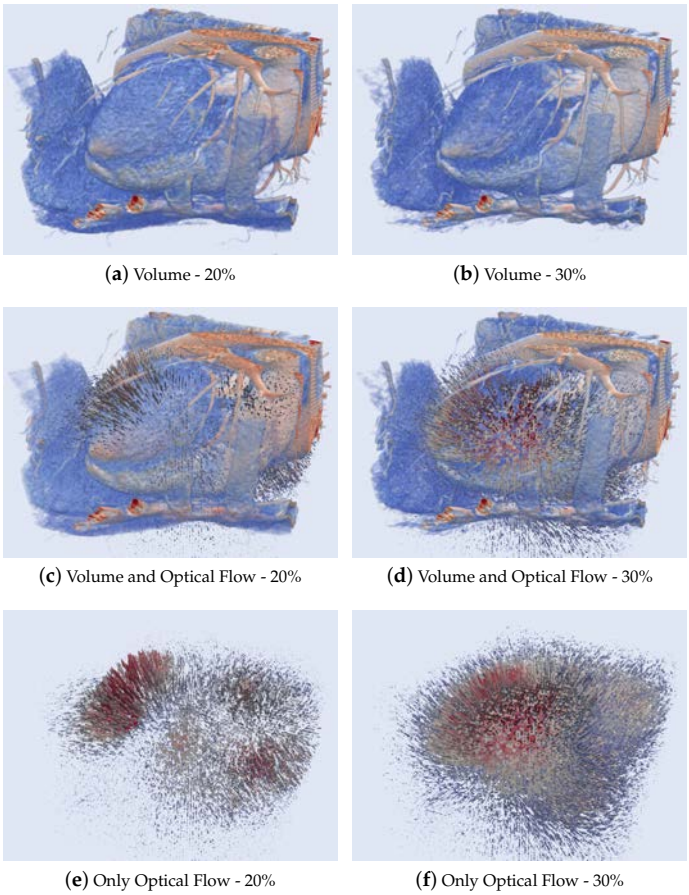

(**a**) Volume - 20%

(**b**) Volume - 30%

(**c**) Volume and Optical Flow - 20%

(**d**) Volume and Optical Flow - 30%

(**e**) Only Optical Flow - 20%

(**f**) Only Optical Flow - 30%

Figure 14. Results of 3D Optical Flow of a segmented cardiac CT volume computed at phases 20–30%.

Figure 15 presents the results of a 3D Optical flow of two cardiac CT volumes computed at phases 50–60% (when a dilation movement occurs) using the HOF3D method. Figure 15a,b show two phases of the cardiac cycle of volume (for better viewing a cut that volume was made). Figure 15c,d show the same phases of volume along with the three-dimensional optical flow field. Also, Figure 15e,f present only the optical flow.

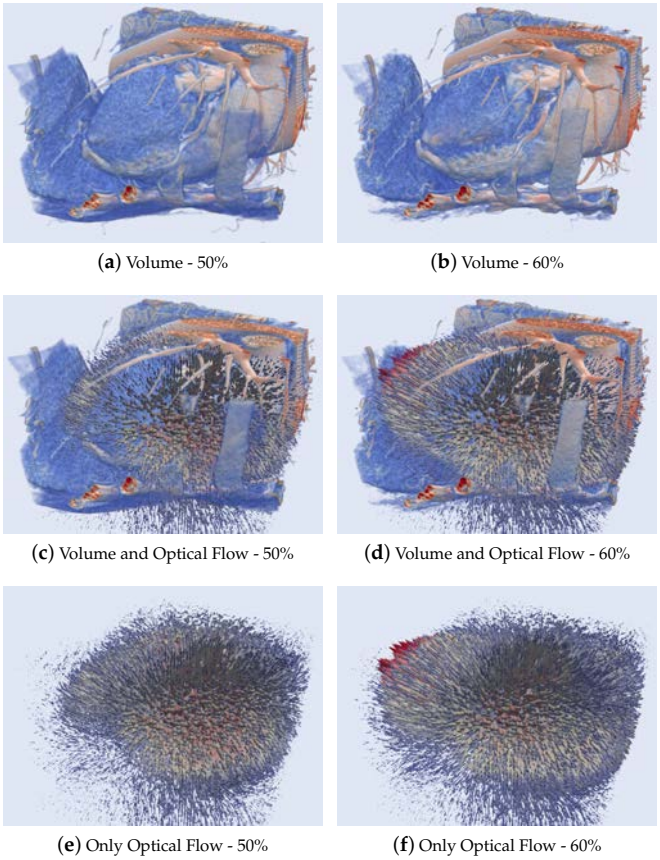

(**a**) Volume - 50% (**b**) Volume - 60%

(**c**) Volume and Optical Flow - 50% (**d**) Volume and Optical Flow - 60%

(**e**) Only Optical Flow - 50% (**f**) Only Optical Flow - 60%

Figure 15. Results of 3D Optical Flow of a segmented cardiac CT volume computed at phases 50–60%.

5.2.1. 3D Optical Flow Estimation of the Left Ventricle

The importance of the study of the left ventricle has been established extensively. The left ventricle adapts, for example, to arterial hypertension and this leads to the development of different geometric patterns [66]. For a better understanding of some diseases, the movement of the left ventricle has been studied during the cardiac cycle in normal subjects and patients with coronary arterial disease, mitral stenosis or atrial septal defect [67]. Works describing the global and local movement have been presented, focusing mainly on the left ventricle [68]. To present the optical flow estimation of the left ventricle, first, a segmentation of it is required. We use the level sets method of Osher and Sethian [69]. This method is a powerful, suitable and flexible approach to segmentation of CT volumes where there aren't well-defined boundaries. The level sets method was applied to the CT volumes using the Seg3D tool [70]. For this tool, a seed volume is used to find similar regions to the original one. Then, the segmented region will be expanded to surrounding pixels that match the statistics of the original seeded area. The spread may also be retracted in some instances if the seeded areas do not match certain criteria (edge weight and threshold range). Until the convergence, the algorithm will be expanded (or contracted) to the segmented region.

Figure 16 shows an example of the segmentations obtained (colored region) in the context of their location within the whole cardiac volume.

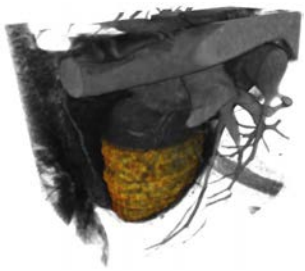

Figure 16. A whole cardiac volume and its left ventricle segmented.

Similarly to the work done in Section 5.1.4, and if we focus on the phase where a contraction movement occurs for the left ventricle, we can observe the interpolation error for a left ventricle segmented showing the original volume in Figure 17a, the interpolated volume using the 3D variant of the method of Sun et al. [20] are in Figure 17b, the error between the original volume and this interpolated result, in Figure 17d. Also, the optical flow is calculated by the HOF3D method. Then, the interpolation of the left ventricle is obtained, which is shown in Figure 17c. The difference between the original volume and that interpolated volume can be observed in Figure 17e.

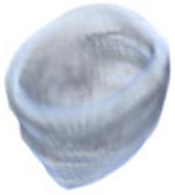

(**a**) Original LV- 30%

(**b**) LV Interpolated using the 3D method of Sun et al. [20]

(**c**) LV Interpolated using the HOF3D method

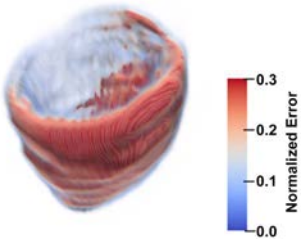

(**d**) Error using the 3D method of Sun et al. [20]

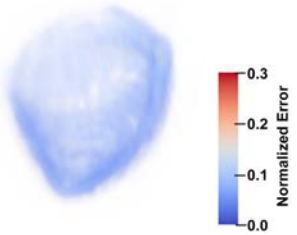

(**e**) Error using the HOF3D method

Figure 17. Interpolation Errors for the left ventricle at 30%.

Sensors **2020**, *20*, 595

Another example of interest, where there is more interpolation error, is the 60% of cardiac phase, it is also when a dilatation movement occurs for the left ventricle. We can observe the interpolation error for a left ventricle segmented for the original volume in Figure 18a, the interpolated volume using the 3D method of Sun et al. [20] in Figure 18b, the error between the original volume and this interpolated result in Figure 18d. Also, the optical flow is calculated by the HOF3D method. Then, the interpolation of the left ventricle is obtained and shown in Figure 18c. The difference between the original volume and that interpolated volume can be observed in Figure 18e.

(**a**) Original LV- 60%

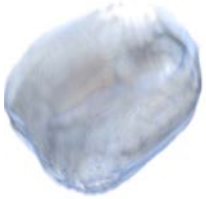

(**b**)LV Interpolated using the 3D method of Sun et al. [20]

(**c**) LV Interpolated using the HOF3D

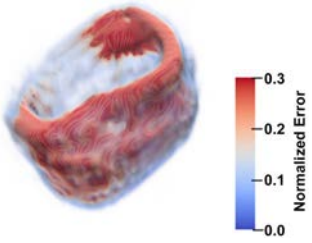

(**d**) Error using the 3D method of Sun et al. [20]

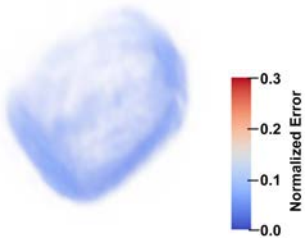

(**e**) Error using the HOF3D method

Figure 18. Interpolation Errors for the left ventricle at 60%.

Figure 19 contains the results of the normalized interpolation error with the Sun et al. [20] method. In Figure 19a we present a set of volumes from 30% to 70% of the cardiac cycle, in Figure 19b, the interpolated volumes corresponding to each stage of the cardiac cycle are shown. Figure 19c graphically displays the normalized interpolation error for the volumes of sections a and b respectively.

Figure 20 contains the results of the normalized interpolation error with the HOF3D method. Figure 20a presents a set of volumes from 30% to 70% of the cardiac cycle, Figure 20b shows the interpolated volumes corresponding to each stage of the cardiac cycle. Figure 20c graphically displays the normalized interpolation error for the volumes of sections a and b respectively.

(**a**) Original Volumes

(**b**) Interpolated Volumes

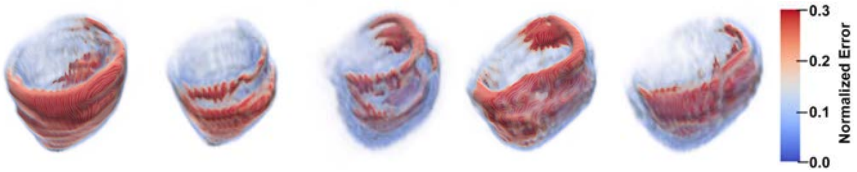

(**c**) Normalized Interpolation Error

Figure 19. Left Ventricle from 30% to 70% of the cardiac cycle and the results with 3D method of Sun et al. [20].

(**a**) Original Volumes

(**b**) Interpolated Volumes

(**c**) Normalized Interpolation Error (HOF3D method)

Figure 20. Left Ventricle from 30% to 70% of the cardiac cycle and the results with HOF3D method.

Sensors **2020**, *20*, 595

Figures 21 and 22 present the results of a 3D Optical flow of two segmented cardiac CT volumes, showing a contraction and relaxation movement respectively using the HOF3D method. Figure 21a,c are two phases of the segmented cardiac cycle of volume computed at phases 20–30%, the same way as Figure 22a,c but in phases 40–50%. Figure 21b,d, Figure 22b,d show only their respective optical flows.

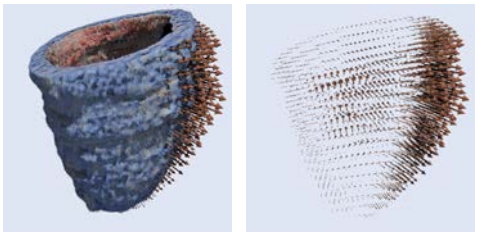

(**a**) volume - 20% (**b**) Only flow - 20%

(**c**) volume - 30% (**d**) Only flow - 30%

Figure 21. Results of 3D Optical Flow of a segmented cardiac CT volume (left ventricle) computed at phases 20–30% (contraction movement).

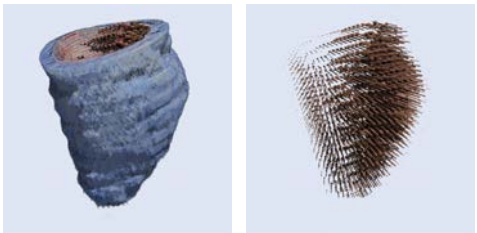

(**a**) volume - 40% (**b**) Only flow - 40%

(**c**) volume - 50% (**d**) Only flow - 50%

Figure 22. Results of 3D Optical Flow of a segmented cardiac CT volume (left ventricle) computed at phases 40–50% (relaxation movement).

Figure 23 contains the results corresponding to the optical flow calculated with the HOF3D method. We can observe a set of left ventricle volumes from 10% to 100% of the cardiac cycle.

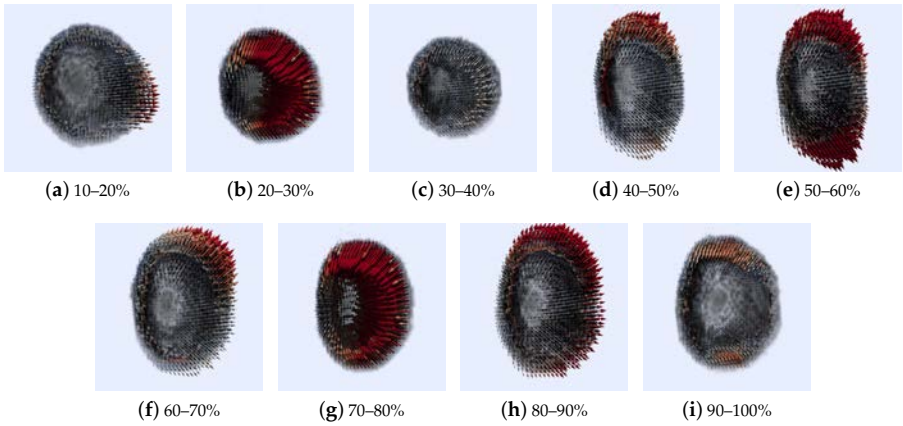

(**a**) 10–20% (**b**) 20–30% (**c**) 30–40% (**d**) 40–50% (**e**) 50–60%

(**f**) 60–70% (**g**) 70–80% (**h**) 80–90% (**i**) 90–100%

Figure 23. Results of 3D Optical Flow of a segmented cardiac CT volume (left ventricle–short axis).

6. Discussion

In this section we will talk about the results obtained, their interpretation and the level of relevance reached.

In the first group of results (Figures 14 and 15), the entire cardiac volume and its respective calculated optical flows can be observed in context. The best way to display this 3D flow has been attempted. Despite a large number of 3D arrows of different sizes, it is possible to observe either the contraction pattern (Figure 14) or the expansion pattern (Figure 15). The optical flow is shown using of Paraview [71,72] whose style of representing the vectors of the optical flow is similar to the previous works in [73] and recently in [74].

We focused on estimating the movement in one of the most important structural parts of the heart, the left ventricle. To achieve this goal we have segmented that heart region, which is shown in Figure 16. We can see examples in [75,76] of the deployment of the three-dimensional vectors of the obtained optical flow. However, in all the remaining figures within the set of results obtained, rather than deploying the obtained optical flow vectors, we decided to show graphically, a measure of the performance achieved in the estimation of cardiac movement, specifically in the left ventricle. The relevance of the figures thus represented is that the errors obtained can be observed graphically, first in the interpolated volumes (Figures 17 and 18, items b and c), where we can compare a similar and known method with the proposed one. In the same figures mentioned, the interpolation error is observed through of a three-dimensional representation that matches the analyzed volumes (Figures 17 and 18, items d and e). In those figures, the biggest errors are the ones represented in red and the smallest tend to blue.

We observe a more extensive sequence of of the cardiac cycle (five phases) in order to provide greater clarity. In this selection of phases of the cardiac cycle we can observe the movement of contraction and dilatation in the left ventricle. In Figures 19 and 20 in part a, we observe the original volumes. In Figures 19 and 20 part b, we see the interpolated volumes with a comparison between the two methods. In Figures 19 and 20 item c, we see a graphical representation of the normalized interpolation error.

Finally, Figures 21 and 22 present more explicitly the segmented left ventricle and their respective optical flows during the contraction and relaxation movements. Figure 23 shows the segmented volumes from the short view concerning all phases of the cardiac cycle (from 10% to 100%).

Motion vectors were exaggerated for clarity. In the field of medical images, and in addition to the cardiac movement, this approach can be used with benefit in pulmonary movement. In general, in applications where we have three-dimensional data, such as cardiac and pulmonary medical images, stereoscopic images and video, 3D meteorological data, volumes formed by point clouds in general. Where we want to characterize how they evolve over time. For future work, there is a great margin of opportunity to improve the times in the calculations of the Hermite transform, for which a faster version was not used. For the energy functional used, some other local and global characteristics can be incorporated that allow us to further reduce the uncertainties obtained.

7. Conclusions

In this paper, we have proposed a method to estimate the optical flow completely in $3D + t$, that is, in a three-dimensional space (x, y, z) plus time, because the analysis of two-dimensional motion restricts all possible deformations in the different directions of reference (i.e., radial, circumferential and longitudinal). Therefore, the three-dimensional motion analysis can overcome such limitations by describing better all directions of deformations.

Our approximation of motion estimation has included the well-known differential method of Horn and Schunck with the additional information provided by the coefficients of the Steered Hermite transform used within the restriction terms of the function to be minimized. The Steered Hermite transform is a model that incorporates some important properties of the first stages of the human visual system, such as the overlapping Gaussian receptive fields, the Gaussian derivative model of early vision [52], and a multiresolution analysis [60,77]. This proposed algorithm is more robust to noise due to the advantage represented by the analysis of the spatial scale provided by the Hermite transform itself that can be determined for objects at different spatial dimensions. Additionally, and due to the calculation of high order Gaussian derivatives, the estimation of the movement can be improved by including structures related to them.

We evaluated the results obtained using two measurements on the interpolation errors, with these errors we also adjusted the most appropriate parameters in the different cardiac sets considered. We observed that interpolation errors increased around the phases where movements occur most rapidly (the contraction phase). We were able to verify that the proposed method (HOF3D) has lower interpolation errors compared to the modified 3D method of Sun et al. [20].

We isolated the three-dimensional flow vectors corresponding to the left ventricle, over the entire cardiac cycle. We calculated the interpolation errors obtained with our method, comparing the results with the other method already mentioned. The results were plotted graphically, showing that the largest errors were colored in red, as shown in the figures. Again, our method has minor interpolation errors.

Our proposal also aims to contribute to a better understanding of cardiac movements and, with this, to make feasible the detection of some possible diseases. We consider that because the cardiac organ is immersed in a three-dimensional space, the best way to represent its movements should be in the same three-dimensional space. Future work may focus on recognizing the cardiac movement patterns related to the vectors obtained in our three-dimensional optical flow approximation.

Author Contributions: Conceptualization, B.E.-R., C.M., E.V. and E.M.-A.; methodology, C.M., E.M.-A.; software, C.M. and E.M.-A.; validation, C.M., E.V., E.M.-A., J.O., J.B.; formal analysis, C.M. and E.M.-A.; investigation, C.M. and E.M.-A.; resources, B.E.-R., E.V., and J.O.; data curation, E.V. and J.O.; writing—original draft preparation, C.M. and E.M.-A.; writing—review and editing, C.M., E.M.-A., B.E.-R. and J.O.; visualization, C.M.; supervision, B.E.-R., E.M.-A., J.O. and J.B.; project administration, B.E.-R. All authors have read and agreed to the published version of the manuscript.

Funding: This research was funded by UNAM-PAPIIT grants numbers IN116917 and IA103119 and SECTEI grant 202/2019.

Acknowledgments: Carlos Mira gratefully acknowledges the scholarship from CONACyT to pursue his doctoral studies. Ernesto Moya-Albor and Jorge Brieva would like to thank the Facultad de Ingeniería of Universidad Panamericana for all support in this work. Boris Escalante-Ramírez and Jimena Olveres are thankful for the funding support through UNAM PAPIIT for all support in this work.

Conflicts of Interest: The authors declare no conflict of interest.

Abbreviations

The following abbreviations are used in this manuscript:

$3D + t$	Three-dimensional space plus time
$2D + t$	Two-dimensional space plus time
HT	Hermite transform
SHT	Steered Hermite transform
HVS	Human vision system
CT	Computed tomography
CVD	Cardiovascular diseases
LV	Left ventricular
MRI	Magnetic resonance imaging
HT3D	Hermite transform in 3D
IHT3D	Inverse Hermite transform in 3D
SHT3D	Steered Hermite transform in 3D
HOF3D	Horn-Hermite optical flow in 3D
ECG	Electrocardiography
IE	Interpolation error
NE	Normalized interpolation error
CNN	Convolutional Neural Network

References

1. World Health Organization. Cardiovascular diseases (CVD). 2019. Available online: http://www.who.int/mediacentre/factsheets/fs317/en/ (accessed on 22 November 2019).
2. Cheung, Y.F. The role of 3D wall motion tracking in heart failure. *Nat. Rev. Cardiol.* **2012**, *9*, 644. [CrossRef] [PubMed]
3. Xiong, G.; Sun, P.P.; Zhou, H.; Ha, S.; o Hartaigh, B.; Truong, Q.A.; Min, J.K. Comprehensive Modeling and Visualization of Cardiac Anatomy and Physiology from CT Imaging and Computer Simulations. *IEEE Trans. Vis. Comput. Graph.* **2017**, *23*, 1014–1028. [CrossRef] [PubMed]
4. Min, J.K.; Shaw, L.; Berman, D. The Present State of Coronary Computed Tomography Angiography A Process in Evolution. *Am. Coll. Cardiol.* **2010**, *55*, 957–965. [CrossRef] [PubMed]
5. Schoenhagen, P.; Stillman, A.; Halliburton, S.; White, R. CT of the heart: Principles, advances, clinical uses. *Clevel. Clin. J. Med.* **2005**, *72*, 127–140. [CrossRef] [PubMed]
6. Barron, J.L.; Fleet, D.J.; Beauchemin, S.S.; Burkitt, T.A. Performance of optical flow techniques. In Proceedings of the 1992 IEEE Computer Society Conference on Computer Vision and Pattern Recognition, Champaign, IL, USA, 15–18 June 1992; pp. 236–242. [CrossRef]
7. Nagel, H.H.; Enkelmann, W. An Investigation of Smoothness Constraints for the Estimation of Displacement Vector Fields from Image Sequences. *IEEE Trans. Pattern Anal. Mach. Intell.* **1986**, *PAMI-8*, 565–593. [CrossRef] [PubMed]
8. Nagel, H.H. Displacement vectors derived from second-order intensity variations in image sequences. *Comput. Vis. Graph. Image Process.* **1983**, *21*, 85–117. [CrossRef]
9. TRETIAK, O. Velocity estimation form image sequences with second order differential operators. In Proceedings of the International Conference on Pattern Recognition, Montreal, QC, Canada, 30 July–2 August 1984.
10. Haralick, R.M.; Lee, J.S. *The Facet Approach to Optic Flow*; Technical Report; Virginia Polytechnic Inst and State Univ Blacksburg Dept of Computer Science: Blacksburg, VA, USA, 1983.
11. Horn, B.K.P.; Schunck, B.G. Determining Optical Flow. *Artif. Intell.* **1981**, *17*, 185–203. [CrossRef]

12. Hildreth, E.C. Computations underlying the measurement of visual motion. *Artif. Intell.* **1984**, *23*, 309–354. [CrossRef]
13. Lucas, B.D.; Kanade, T. An Iterative Image Registration Technique with an Application to Stereo Vision. In Proceedings of the 7th International Joint Conference on Artificial Intelligence, Vancouver, BC, Canada, 24–28 August 1981; Morgan Kaufmann Publishers Inc.: San Francisco, CA, USA; Volume 2, pp. 674–679.
14. Uras, S.; Girosi, F.; Verri, A.; Torre, V. A computational approach to motion perception. *Biol. Cybern.* **1988**, *60*, 79–87. [CrossRef]
15. Anandan, P. A computational framework and an algorithm for the measurement of visual motion. *Int. J. Comput. Vis.* **1989**, *2*, 283–310. [CrossRef]
16. Little, J.; Bulthoff, H.; Poggio, T. *Parallel Optical Flow Using Local Voting*; IEEE: New York, NY, USA, 1988; pp. 454–459.
17. Adelson, E.H.; Bergen, J.R. Spatiotemporal energy models for the perception of motion. *J. Opt. Soc. Am. A* **1985**, *2*, 284–299. [CrossRef]
18. Heeger, D.J. Optical flow using spatiotemporal filters. *Int. J. Comput. Vis.* **1988**, *1*, 279–302. [CrossRef]
19. Fleet, D.J.; Jepson, A.D. Computation of component image velocity from local phase information. *Int. J. Comput. Vis.* **1990**, *5*, 77–104. [CrossRef]
20. Sun, D.; Roth, S.; Black, M.J. Secrets of optical flow estimation and their principles. In Proceedings of the 2010 IEEE Computer Society Conference on Computer Vision and Pattern Recognition, San Francisco, CA, USA, 13–18 June 2010; pp. 2432–2439. [CrossRef]
21. Haag, M.; Nagel, H.H. Combination of Edge Element and Optical Flow Estimates for 3D-Model-Based Vehicle Tracking in Traffic Image Sequences. *Int. J. Comput. Vis.* **1999**, *35*, 295–319.:1008112528134. [CrossRef]
22. Amat, F.; Myers, E.W.; Keller, P.J. Fast and robust optical flow for time-lapse microscopy using super-voxels. *Bioinformatics* **2013**, *29*, 373–380. [CrossRef] [PubMed]
23. Barranco, F.; Fermüller, C.; Aloimonos, Y.; Ros, E. Joint direct estimation of 3D geometry and 3D motion using spatio temporal gradients. *arXiv* **2018**, arXiv:1805.06641.
24. Patil, G.; Suja, P. Emotion recognition from 3D videos using optical flow method. In Proceedings of the 2017 International Conference On Smart Technologies For Smart Nation (SmartTechCon), Bengaluru, India, 17–19 August 2017; pp. 825–829. [CrossRef]
25. Rodriguez, M.P.; Nygren, A. Motion Estimation in Cardiac Fluorescence Imaging With Scale-Space Landmarks and Optical Flow: A Comparative Study. *IEEE Trans. Biomed. Eng.* **2015**, *62*, 774–782. [CrossRef]
26. Saleh, R.H.; Bakr, H.M.A.; Zidan, I.; Hadhoud, M.M.A. An innovate automatic heart localization method in cardiac Cine MRI using optical flow. In Proceedings of the 8th Cairo International Biomedical Engineering Conference (CIBEC), Cairo, Egypt , 15–17 December 2016; pp. 106–109. [CrossRef]
27. Liu, H.; Hong, T.H.; Herman, M.; Chellappa, R. A General Motion Model and Spatio-Temporal Filters for Computing Optical Flow. *Int. J. Comput. Vis.* **1997**, *22*, 141–172.:1007988028861. [CrossRef]
28. Silvan-Cardenas, J.L.; Escalante-Ramirez, B. Optic-flow information extraction with directional Gaussian-derivatives. In Proceedings of the 15th International Conference on Pattern Recognition ICPR-2000, Barcelona, Spain, 3–7 September 2000; Volume 3, pp. 190–193. [CrossRef]
29. Moya-Albor, E.; Escalante-RamíRez, B.; Vallejo, E. Optical Flow Estimation in Cardiac CT Images Using the Steered Hermite Transform. *Image Commun.* **2013**, *28*, 267–291. [CrossRef]
30. Baghaie, A.; DSouza, R.M.; Yu, Z. Dense correspondence and optical flow estimation using gabor, schmid and steerable descriptors. In *International Symposium on Visual Computing*; Springer: Cham, Switzerland, 2015; pp. 406–415.
31. Satriano, A.; Heydari, B.; Narous, M.; Exner, D.V.; Mikami, Y.; Attwood, M.M.; Tyberg, J.V.; Lydell, C.P.; Howarth, A.G.; Fine, N.M.; et al. Clinical feasibility and validation of 3D principal strain analysis from cine MRI: Comparison to 2D strain by MRI and 3D speckle tracking echocardiography. *Int. J. Cardiovasc. Imaging* **2017**, *33*, 1979–1992. [CrossRef]
32. Pedrizzetti, G.; Sengupta, S.; Caracciolo, G.; Park, C.S.; Amaki, M.; Goliasch, G.; Narula, J.; Sengupta, P.P. Three-Dimensional Principal Strain Analysis for Characterizing Subclinical Changes in Left Ventricular Function. *J. Am. Soc. Echocardiogr.* **2014**, *27*, 1041–1050.e1. [CrossRef] [PubMed]
33. Barba, -J.L.; Moya-Albor, E.; Escalante-Ramírez, B.; Brieva, J.; Venegas, E.V. Segmentation and optical flow estimation in cardiac CT sequences based on a spatiotemporal PDM with a correction scheme and the Hermite transform. *Comput. Biol. Med.* **2016**, *69*, 189–202. [CrossRef] [PubMed]

34. Ranjan, A.; Romero, J.; Black, M.J. Learning human optical flow. *arXiv* **2018**, arXiv:1806.05666.
35. Alexiadis, D.S.; Mitianoudis, N.; Stathaki, T. Multidimensional directional steerable filters—Theory and application to 3D flow estimation. *Image Vis. Comput.* **2018**, *71*, 38–67. [CrossRef]
36. Ha, I.Y.; Wilms, M.; Handels, H.; Heinrich, M.P. Model-based sparse-to-dense image registration for realtime respiratory motion estimation in image-guided interventions. *IEEE Trans. Biomed. Eng.* **2018**, *66*, 302–310. [CrossRef]
37. Yoon, S.; Katsevich, A.; Frenkel, M.; Munro, P.; Paysan, P.; Seghers, D.; Strzelecki, A. A motion estimation and compensation algorithm for 4D CBCT of the abdomen. In Proceedings of the 15th International Meeting on Fully Three-Dimensional Image Reconstruction in Radiology and Nuclear Medicine, Philadelphia, PA, USA, 2–6 June 2019; International Society for Optics and Photonics: Bellingham, WA, USA, 2019; Volume 11072, p. 110720E.
38. Cha, J.; Farhangi, M.M.; Dunlap, N.; Amini, A.A. Segmentation and tracking of lung nodules via graph-cuts incorporating shape prior and motion from 4D CT. *Med. Phys.* **2018**, *45*, 297–306. [CrossRef]
39. Prevost, R.; Salehi, M.; Jagoda, S.; Kumar, N.; Sprung, J.; Ladikos, A.; Bauer, R.; Zettinig, O.; Wein, W. 3D freehand ultrasound without external tracking using deep learning. *Med. Image Anal.* **2018**, *48*, 187–202. [CrossRef]
40. Gorce, J.; Friboulet, D.; Magnin, I. Estimation of three-dimensional cardiac velocity fields: Assessment of a differential method and application to 3D CT data. *Med. Image Anal* **1997**, *1*, 127–140. [CrossRef]
41. Queirós, S.; Vilaça, J.L.; Morais, P.; Fonseca, J.C.; D'hooge, J.; Barbosa, D. Fast left ventricle tracking using localized anatomical affine optical flow. *Int. J. Numer. Methods Biomed. Eng.* **2017**, *33*, e2871. [CrossRef]
42. Krishnaswamy, D.; Hareendranathan, A.R.; Suwatanaviroj, T.; Boulanger, P.; Becher, H.; Noga, M.; Punithakumar, K. A Novel 4D Semi-Automated Algorithm for Volumetric Segmentation in Echocardiography. In Proceedings of the 2018 40th Annual International Conference of the IEEE Engineering in Medicine and Biology Society (EMBC), Honolulu, HI, USA, 18–21 July 2018; pp. 1119–1122.
43. Tek, H.; Georgescu, B.; Mansi, T.; Sauer, F.; Comaniciu, D.; Houle, H.C.; Voigt, I. Cardiac Flow Detection Based on Morphological Modeling in Medical Diagnostic Ultrasound Imaging. U.S. Patent Application No. 15/797,161, 2 May 2019.
44. Duan, Q.; Angelini, E.D.; Herz, S.L.; Ingrassia, C.M.; Gerard, O.; Costa, K.D.; Holmes, J.W.; Laine, A.F. Evaluation of optical flow algorithms for tracking endocardial surfaces on three-dimensional ultrasound data. *Proc. SPIE* **2005**, *5750*, 159–169. [CrossRef]
45. Duan, Q.; Angelini, E.D.; Homma, S.; Laine, A. Validation of Optical-Flow for Quantification of Myocardial Deformations on Simulated Rt3d Ultrasound. In Proceedings of the 2007 IEEE International Symposium on Biomedical Imaging: From Nano to Macro, Washington, DC, USA, 12–16 April 2007; pp. 944–947. [CrossRef]
46. Leung, E.; Danilouchkine, M.; van Stralen, M.; de Jong, N.; van der Steen, A.; Bosch, J. Tracking left ventricular borders in 3D echocardiographic sequences using motion-guided optical flow. *SPIE* **2009**. [CrossRef]
47. Zhang, Y.; Liang, X.; Ma, J.; Jing, Y.; Gonzales, M.J.; Villongco, C.; Krishnamurthy, A.; Frank, L.R.; Nigam, V.; Stark, P.; et al. An atlas-based geometry pipeline for cardiac Hermite model construction and diffusion tensor reorientation. *Med. Image Anal.* **2012**, *16*, 1130–1141. [CrossRef] [PubMed]
48. Thirion, J.P. Image matching as a diffusion process: An analogy with Maxwell's demons. *Med. Image Anal.* **2018**, *2*, 243–260. [CrossRef]
49. Moya-Albor, E.; Mira, C.; Brieva, J.; Escalante-Ramirez, B.; Venegas, E.V. 3D optical flow estimation in cardiac CT images using the Hermite transform. *SPIE* **2017**, *10160*. [CrossRef]
50. Martens, J.B. The Hermite Transform-Theory. *IEEE Trans. Acoust. Speech Signal Process.* **1990**, *38*, 1595–1606. [CrossRef]
51. Sakitt, B.; Barlow, H. A Model for the Economical Encoding of the Visual Image in Cerebral Cortex. *Biol. Cybern.* **1982**, *43*, 97–108. [CrossRef]
52. Young, R. *The Gaussian Derivative Theory of Spatial Vision: Analysis of Cortical Cell Receptive Field Line–Weighting Profiles*; Research publication; General Motors Research Laboratories: Warren, MI, USA, 1985.
53. Martens, J.B. The Hermite Transform-Applications. *IEEE Trans. Acoust. Speech Signal Process.* **1990**, *38*, 1607–1618. [CrossRef]
54. Young, R. Gaussian derivative model of spatial vision: I. Retinal mechanisms. *Spat. Vis.* **1987**, *2*, 273–293. [CrossRef]

55. Brackx, F.; De Schepper, N.; Sommen, F. The higher dimensional Hermite transform: A new approach. *Complex Var.* **2003**, *48*, 189–210. [CrossRef]
56. Abramowitz, M. *Handbook of Mathematical Functions, With Formulas, Graphs, and Mathematical Tables*; Dover Publications: Mineola, NY, USA, 1974.
57. Van Dijk, A.M.; Martens, J. Image representation and compression with steered Hermite transforms. *Signal Process.* **1997**, *56*, 1–16. [CrossRef]
58. Freeman, W.T.; Adelson, E.H. The Design and Use of Steerable Filters. *IEEE Trans. Pattern Anal. Mach. Intell.* **1991**, *13*, 891–906. [CrossRef]
59. Escalante-Ramírez, B.; Silván-Cárdenas, J.L. Multiresolution directional-oriented image transform based on Gaussian derivatives. *Proc. SPIE* **2001**, *4478*, 4478–4478. [CrossRef]
60. Escalante-Ramírez, B.; Silván-Cárdenas, J.L. Advanced modeling of visual information processing: A multiresolution directional-oriented image transform based on Gaussian derivatives. *Signal Process. Image Commun.* **2005**, *20*, 801–812. [CrossRef]
61. Wu, X.; Ding, G.; Taylor, V. Parallel Optical Flow Processing of 4D Cardiac CT Data on Multicore Clusters. In Proceedings of the 2014 IEEE 17th International Conference on Computational Science and Engineering, Chengdu, China, 19–21 December 2014; pp. 113–120.
62. Otte, M.; Nagel, H.H. Optical flow estimation: Advances and comparisons. In *European Conference on Computer Vision*; Eklundh, J.O., Ed.; Springer: Berlin/Heidelberg, Germany, 1994; Volume I, pp. 49–60._5. [CrossRef]
63. Baker, S.; Scharstein, D.; Lewis, J.P.; Roth, S.; Black, M.J.; Szeliski, R. A Database and Evaluation Methodology for Optical Flow. *Int. J. Comput. Vis.* **2011**, *92*, 1–31. [CrossRef]
64. Mathworks, T. Computer Vision System Toolbox. 2018. Available online: https://mathworks.com/products/computer-vision (accessed on 22 November 2019).
65. Bigun, J.; Granlund, G.H.; Wiklund, J. Multidimensional orientation estimation with applications to texture analysis and optical flow. *IEEE Trans. Pattern Anal. Mach. Intell.* **1991**, *no. 8*. p. 775–790. [CrossRef]
66. Koren, M.J.; Devereux, R.B.; Casale, P.N.; Savage, D.D.; Laragh, J.H. Relation of left ventricular mass and geometry to morbidity and mortality in uncomplicated essential hypertension. *Ann. Intern. Med.* **1991**, *114*, 345–352. [CrossRef]
67. McDonald, I.G. The shape and movements of the human left ventricle during systole: A study by cineangiography and by cineradiography of epicardial markers. *Am. J. Cardiol.* **1970**, *26*, 221–230. [CrossRef]
68. Chen, C.W.; Huang, T.S. Epicardial motion and deformation estimation from coronary artery bifurcation points. In Proceedings Third International Conference on Computer Vision, Osaka, Japan, 4–7 December 1990; pp. 456–459.
69. Osher, S.; Sethian, J.A. Fronts propagating with curvature-dependent speed: Algorithms based on Hamilton-Jacobi formulations. *J. Comput. Phys.* **1988**, *79*, 12–49. [CrossRef]
70. CIBC. Seg3D: Volumetric Image Segmentation and Visualization. Scientific Computing and Imaging Institute (SCI). 2016. Available online: Http://www.seg3d.org (accessed on 22 November 2019).
71. Ahrens, J.; Geveci, B.; Law, C. Paraview: An end-user tool for large data visualization. In *The Visualization Handbook*; Elsevier: Amsterdam, The Netherlands, 2005; Volume 717, ISBN 978-0123875822.
72. Ayachit, U. *The Paraview Guide: A Parallel Visualization Application*; Kitware, Inc.: Clifton Park, NY, USA, 2015.
73. Song, S.M.; Leahy, R.M. Computation of 3-D velocity fields from 3-D cine CT images of a human heart. *IEEE Trans. Med. Imaging* **1991**, *10*, 295–306. [CrossRef]
74. Chan, K.G.; Liebling, M. Estimation of divergence-free 3D cardiac blood flow in a zebrafish larva using multi-view microscopy. In Proceedings of the 2015 IEEE 12th International Symposium on Biomedical Imaging (ISBI), New York, NY, USA, 16–19 April 2015; pp. 385–388.
75. Gutierrez, M.; Moura, L.; Melo, C.; Alens, N. Computing optical flow in cardiac images for 3D motion analysis. In Proceedings of the Computers in Cardiology Conference, London, UK, 5–8 September 1993; pp. 37–40.

76. Condell, J.; Barron, L. 3D Optical Flow Methods in Cardiac Imaging. In Proceedings of the Irish Machine Vision and Image Processing Conference, Belfast, UK, 30–31 August 2005; Volume 30, p. 227.
77. Silván-Cárdenas, J.L.; Escalante-Ramírez, B. The Multiscale Hermite Transform for Local Orientation Analysis. *IEEE Trans. Image Process.* **2006**, *15*, 1236–1253. [CrossRef]

Bibliography

[1] World Health Organization, "Cardiovascular diseases (CVD)." http://www.who.int/mediacentre/factsheets/fs317/en/, Aug. 2019. Accessed: 2020-01-10. 1

[2] Y. f. Cheung, "The role of 3d wall motion tracking in heart failure," *Nature Reviews Cardiology*, vol. 9, p. 644(14), 2012. 1

[3] G. Xiong, P. P. Sun, H. Zhou, S. Ha, B. o Hartaigh, Q. A. Truong, and J. K. Min, "Comprehensive modeling and visualization of cardiac anatomy and physiology from ct imaging and computer simulations," *IEEE Transactions on Visualization and Computer Graphics*, vol. 23, pp. 1014–1028, 2017. 1

[4] J. K Min, L. Shaw, and D. Berman, "The present state of coronary computed tomography angiography a process in evolution," *of the American College of Cardiology*, vol. 55, pp. 957–65, 03 2010. 1

[5] P. Schoenhagen, A. Stillman, S. Halliburton, and R. White, "Ct of the heart: principles, advances, clinical uses," *Cleveland Clinic Journal of Medicine*, vol. 72, no. 3, pp. 127–140, 2005. 1

[6] J. L. Barron, D. J. Fleet, S. S. Beauchemin, and T. A. Burkitt, "Performance of optical flow techniques," in *Computer Vision and Pattern Recognition, 1992. Proceedings CVPR '92., 1992 IEEE Computer Society Conference on*, pp. 236–242, Jun 1992. 1, 2, 30, 37, 47, 54

[7] H. H. Nagel and W. Enkelmann, "An investigation of smoothness constraints for the estimation of displacement vector fields from image sequences," *IEEE Transactions on Pattern Analysis and Machine Intelligence*, vol. PAMI-8, pp. 565–593, Sept 1986. 1, 2, 36

[8] H.-H. Nagel, "Displacement vectors derived from second-order intensity variations in image sequences," *Computer Vision, Graphics, and Image Processing*, vol. 21, no. 1, pp. 85 – 117, 1983. 2

[9] O. Tretiak, "Velocity estimation form image sequences with second order differential operators," *Proc. International Conference on Pattern Recognition*, 1984. 2

[10] R. M. Haralick and J. S. Lee, "The facet approach to optic flow," tech. rep., Virginia Polytechnic Inst. and State Univ. Blacksburg Dept. of Computer Science, 1983. 2

[11] B. K. P. Horn and B. G. Schunck, "Determining optical flow," *Artificial Intelligence*, vol. 17, pp. 185–203, 1981. 2, 4, 5, 35, 39, 41

[12] E. C. Hildreth, "Computations underlying the measurement of visual motion," *Artificial Intelligence*, vol. 23, no. 3, pp. 309 – 354, 1984. 2, 36

[13] B. D. Lucas and T. Kanade, "An iterative image registration technique with an application to stereo vision," in *Proceedings of the 7th International Joint Conference on Artificial Intelligence - Volume 2*, IJCAI'81, (San Francisco, CA, USA), pp. 674–679, Morgan Kaufmann Publishers Inc., 1981. 2, 37, 62

[14] S. Uras, F. Girosi, A. Verri, and V. Torre, "A computational approach to motion perception," *Biological Cybernetics*, vol. 60, pp. 79–87, Dec 1988. 2, 34

[15] P. Anandan, "A computational framework and an algorithm for the measurement of visual motion," *International Journal of Computer Vision*, vol. 2, pp. 283–310, Jan 1989. 2, 5

[16] J. Little, H. Bulthoff, and T. Poggio, "Parallel optical flow using local voting," in *Unknown Host Publication Title*, pp. 454–459, Publ by IEEE, 12 1988. 2

[17] E. H. Adelson and J. R. Bergen, "Spatiotemporal energy models for the perception of motion," *J. Opt. Soc. Am. A*, vol. 2, pp. 284–299, Feb 1985. 2

[18] D. J. Heeger, "Optical flow using spatiotemporal filters," *International Journal of Computer Vision*, vol. 1, pp. 279–302, Jan 1988. 2, 34

[19] D. J. Fleet and A. D. Jepson, "Computation of component image velocity from local phase information," *International Journal of Computer Vision*, vol. 5, no. 1, pp. 77–104, 1990. 2, 54

[20] D. Sun, S. Roth, and M. J. Black, "Secrets of optical flow estimation and their principles," in *2010 IEEE Computer Society Conference on Computer Vision and Pattern Recognition*, pp. 2432–2439, June 2010. 2, 4, 41, 45, 46, 57, 58, 59, 69, 70, 71, 72, 79

[21] M. Haag and H.-H. Nagel, "Combination of edge element and optical flow estimates for 3d-model-based vehicle tracking in traffic image sequences," *International Journal of Computer Vision*, vol. 35, pp. 295–319, Dec 1999. 2

[22] F. Amat, E. W. Myers, and P. J. Keller, "Fast and robust optical flow for time-lapse microscopy using super-voxels," *Bioinformatics*, vol. 29, no. 3, pp. 373–380, 2013. 2

[23] F. Barranco, C. Fermüller, Y. Aloimonos, and E. Ros, "Joint direct estimation of 3d geometry and 3d motion using spatio temporal gradients," *arXiv preprint arXiv:1805.06641*, 2018. 2

[24] G. Patil and P. Suja, "Emotion recognition from 3d videos using optical flow method," in *2017 International Conference On Smart Technologies For Smart Nation (SmartTechCon)*, pp. 825–829, Aug 2017. 2, 4

[25] M. P. Rodriguez and A. Nygren, "Motion estimation in cardiac fluorescence imaging with scale-space landmarks and optical flow: A comparative study," *IEEE Transactions on Biomedical Engineering*, vol. 62, pp. 774–782, Feb 2015. 2, 4

[26] R. H. Saleh, H. M. A. Bakr, I. Zidan, and M. M. A. Hadhoud, "An innovate automatic heart localization method in cardiac cine mri using optical flow," in *2016 8th Cairo International Biomedical Engineering Conference (CIBEC)*, pp. 106–109, Dec 2016. 2, 4

[27] H. Liu, T.-H. Hong, M. Herman, and R. Chellappa, "A general motion model and spatio-temporal filters for computing optical flow," *International Journal of Computer Vision*, vol. 22, pp. 141–172, Mar 1997. 2

[28] J. L. Silvan-Cardenas and B. Escalante-Ramirez, "Optic-flow information extraction with directional gaussian-derivatives," in *Proceedings 15th International Conference on Pattern Recognition. ICPR-2000*, vol. 3, pp. 190–193 vol.3, 2000. 2

[29] E. Moya-Albor, B. Escalante-RamíRez, and E. Vallejo, "Optical flow estimation in cardiac ct images using the steered hermite transform," *Image Commun.*, vol. 28, pp. 267–291, Mar. 2013. 2, 5, 42, 46

[30] A. Baghaie, R. M. DSouza, and Z. Yu, "Dense correspondence and optical flow estimation using gabor, schmid and steerable descriptors," in *International Symposium on Visual Computing*, pp. 406–415, Springer, 2015. 2, 4

[31] A. Satriano, B. Heydari, M. Narous, D. V. Exner, Y. Mikami, M. M. Attwood, J. V. Tyberg, C. P. Lydell, A. G. Howarth, N. M. Fine, *et al.*, "Clinical feasibility and validation of 3d principal strain analysis from cine mri: comparison to 2d strain by mri and 3d speckle tracking echocardiography," *The International Journal of Cardiovascular Imaging*, pp. 1–14, 2017. 2

[32] G. Pedrizzetti, S. Sengupta, G. Caracciolo, C. S. Park, M. Amaki, G. Goliasch, J. Narula, and P. P. Sengupta, "Three-dimensional principal strain analysis for characterizing subclinical changes in left ventricular function," *Journal of the American Society of Echocardiography*, vol. 27, no. 10, pp. 1041 – 1050.e1, 2014. 2

[33] L. Barba-J, E. Moya-Albor, B. Escalante-Ramírez, J. Brieva, and E. V. Venegas, "Segmentation and optical flow estimation in cardiac CT sequences based on a spatiotemporal PDM with a correction scheme and the Hermite transform," *Computers in Biology and Medicine*, vol. 69, pp. 189 – 202, 2016. 2, 46

[34] A. Ranjan, J. Romero, and M. J. Black, "Learning human optical flow," *arXiv preprint arXiv:1806.05666*, 2018. 3, 4

[35] D. S. Alexiadis, N. Mitianoudis, and T. Stathaki, "Multidimensional directional steerable filters theory and application to 3d flow estimation," *Image and Vision Computing*, vol. 71, pp. 38 – 67, 2018. 3, 4

[36] I. Y. Ha, M. Wilms, H. Handels, and M. P. Heinrich, "Model-based sparse-to-dense image registration for realtime respiratory motion estimation in image-guided interventions," *IEEE Transactions on Biomedical Engineering*, vol. 66, no. 2, pp. 302–310, 2018. 3

[37] S. Yoon, A. Katsevich, M. Frenkel, P. Munro, P. Paysan, D. Seghers, and A. Strzelecki, "A motion estimation and compensation algorithm for 4d cbct of the abdomen," in *15th International Meeting on Fully Three-Dimensional Image Reconstruction in Radiology and Nuclear Medicine*, vol. 11072, p. 110720E, International Society for Optics and Photonics, 2019. 3

[38] C. Jungwon, Farhangi, M. Mehdi, Dunlap, Neal, Amini, and A. A., "Segmentation and tracking of lung nodules via graph-cuts incorporating shape prior and motion from 4d ct," *Medical Physics*, vol. 45, no. 1, pp. 297–306, 2018. 3

[39] R. Prevost, M. Salehi, S. Jagoda, N. Kumar, J. Sprung, A. Ladikos, R. Bauer, O. Zettinig, and W. Wein, "3d freehand ultrasound without external tracking using deep learning," *Medical Image Analysis*, vol. 48, pp. 187 – 202, 2018. 3

[40] J. Gorce, D. Friboulet, and I. Magnin, "Estimation of three-dimensional cardiac velocity fields : Assessment of a differential method and application to 3d ct data," *Med Image Anal*, vol. 1, no. 3, pp. 127–140, 1997. 3

[41] S. Queirós, J. L. Vilaça, P. Morais, J. C. Fonseca, J. D'hooge, and D. Barbosa, "Fast left ventricle tracking using localized anatomical affine optical flow," *International journal for numerical methods in biomedical engineering*, vol. 33, no. 11, p. e2871, 2017. 3, 4

[42] D. Krishnaswamy, A. R. Hareendranathan, T. Suwatanaviroj, P. Boulanger, H. Becher, M. Noga, and K. Punithakumar, "A novel 4d semi-automated algorithm for volumetric segmentation in echocardiography," in *2018 40th Annual International Conference of the IEEE Engineering in Medicine and Biology Society (EMBC)*, pp. 1119–1122, IEEE, 2018. 3

[43] H. Tek, B. Georgescu, T. Mansi, F. Sauer, D. Comaniciu, H. C. Houle, and I. Voigt, "Cardiac flow detection based on morphological modeling in medical diagnostic ultrasound imaging," May 2 2019. US Patent App. 15/797,161. 3

[44] Q. Duan, E. D. Angelini, S. L. Herz, C. M. Ingrassia, O. Gerard, K. D. Costa, J. W. Holmes, and A. F. Laine, "Evaluation of optical flow algorithms for tracking endocardial surfaces on three-dimensional ultrasound data," *Proc. SPIE*, vol. 5750, pp. 159–169, 2005. 3

[45] Q. Duan, E. D. Angelini, S. Homma, and A. Laine, "Validation of optical-flow for quantification of myocardial deformations on simulated rt3d ultrasound," in *Proceedings of the 2007 IEEE International Symposium on Biomedical Imaging: From Nano to Macro, Washington, DC, USA, April 12-16, 2007*, pp. 944–947, 2007. 3

[46] E. Leung, M. Danilouchkine, M. van Stralen, N. de Jong, A. van der Steen, and J. Bosch, "Tracking left ventricular borders in 3d echocardiographic sequences using motion-guided optical flow," *Department of Cardio-Thoracic Surgery, Erasmus University Rotterdam*, Dec. 2009. 3

[47] Y. Zhang, X. Liang, J. Ma, Y. Jing, M. J. Gonzales, C. Villongco, A. Krishnamurthy, L. R. Frank, V. Nigam, P. Stark, S. M. Narayan, and A. D. McCulloch, "An atlas-based geometry pipeline for cardiac hermite model construction and diffusion tensor reorientation," *Medical Image Analysis*, vol. 16, pp. 1130–1141, June 2012. 3

[48] J.-P. Thirion, "Image matching as a diffusion process: an analogy with maxwell's demons," *Medical Image Analysis*, vol. 2, pp. 243–260, June 2018. 3

[49] A. Bruhn and J. Weickert, "Towards ultimate motion estimation: Combining highest accuracy with real-time performance," in *Tenth IEEE International Conference on Computer Vision (ICCV'05) Volume 1*, vol. 1, pp. 749–755, IEEE, 2005. 5

[50] A. Bruhn, J. Weickert, C. Feddern, T. Kohlberger, and C. Schnorr, "Variational optical flow computation in real time," *IEEE Transactions on Image Processing*, vol. 14, no. 5, pp. 608–615, 2005. 5

[51] N. Papenberg, A. Bruhn, T. Brox, S. Didas, and J. Weickert, "Highly accurate optic flow computation with theoretically justified warping," *International Journal of Computer Vision*, vol. 67, no. 2, pp. 141–158, 2006. 5

[52] M. J. Black and P. Anandan, "The robust estimation of multiple motions: Parametric and piecewise-smooth flow fields," *Computer vision and image understanding*, vol. 63, no. 1, pp. 75–104, 1996. 5

[53] E. Memin and P. Perez, "A multigrid approach for hierarchical motion estimation," in *Sixth International Conference on Computer Vision (IEEE Cat. No. 98CH36271)*, pp. 933–938, IEEE, 1998. 5

[54] E. Moya-Albor, C. Mira, J. Brieva, B. Escalante-Ramírez, and E. V. Venegas, "3D optical flow estimation in cardiac CT images using the Hermite transform," in *12th International Symposium on Medical Information Processing and Analysis*, vol. 10160, p. 1016010, International Society for Optics and Photonics, 2017. 5, 45

[55] C. Mira, E. Moya-Albor, B. Escalante-Ramirez, J. Olveres, J. Brieva, and E. Vallejo, "3D Hermite transform optical flow estimation in left ventricle CT sequences," *Sensors*, vol. 20, no. 3, p. 595, 2020. 5, 45, 101

[56] J.-B. Martens, "The Hermite Transform-Applications," *IEEE Transactions on Acoustics, Speech and Signal Processing*, vol. 38, no. 9, pp. 1607–1618, 1990. 7, 8, 17

[57] A. Imdad, S. Bres, V. Eglin, C. Rivero-Moreno, and H. Emptoz, "Writer identification using steered hermite features and svm," in *Ninth International Conference on Document Analysis and Recognition (ICDAR 2007)*, vol. 2, pp. 839–843, IEEE, 2007. 7

[58] C. J. Rivero-Moreno and S. Bres, "Texture feature extraction and indexing by hermite filters," in *Proceedings of the 17th International Conference on Pattern Recognition, 2004. ICPR 2004.*, vol. 1, pp. 684–687, IEEE, 2004. 7

[59] S. Bres, V. Eglin, and C. Volpilhac-Auger, "Evaluation of handwriting similarities using hermite transform," 2006. 7

[60] G. Papari, P. Campisi, and N. Petkov, "Closed form of the steered elongated hermite-gauss wavelets," in *2010 IEEE International Conference on Image Processing*, pp. 377–380, IEEE, 2010. 7

[61] A. S. Krylov, A. Kutovoi, and W. K. Leow, "Texture parameterization with hermite functions," *Computer Graphics and Geometry*, vol. 5, no. 1, pp. 79–91, 2003. 7

[62] M. Latha and G. Kavitha, "Hermite transform and support vector machine based analysis of schizophrenia disorder in magnetic resonance brain images," *International Journal of Biomedical Engineering and Technology*, vol. 27, no. 3, pp. 203–220, 2018. 7

[63] L. Capodiferro, E. D. Di Claudio, G. Jacovitti, and A. Laurenti, "Local orientation estimation by tomographic hermite slices," in *Proceedings of the Fourth IASTED International Conference on Signal Processing, Pattern Recognition, and Applications*, pp. 374–379, ACTA Press, 2007. 7

[64] F. Brackx, N. De Schepper, and F. Sommen, "The higher dimensional hermite transform: a new approach," *Complex Variables, Theory and Application: An International Journal*, vol. 48, no. 3, pp. 189–210, 2003. 7

[65] W. Park, G. Leibon, D. N. Rockmore, and G. S. Chirikjian, "Accurate image rotation using hermite expansions," *IEEE Transactions on Image Processing*, vol. 18, no. 9, pp. 1988–2003, 2009. 7

[66] J.-B. Martens, "The Hermite Transform-Theory," *IEEE Transactions on Acoustics, Speech and Signal Processing*, vol. 38, no. 9, pp. 1595–1606, 1990. 8, 17, 21

[67] E. M. Albor, *Estimación de Flujo Óptico por medio de la Transformada de Hermite*. PhD thesis, Programa de Maestría y Doctorado en Ingeniería. Ingeniería Eléctrica - Procesamiento Digital de Señales, 2013. 8

[68] D. Marr and S. Ullman, "Directional selectivity and its use in early visual processing," *Proceedings of the Royal Society of London. Series B. Biological Sciences*, vol. 211, no. 1183, pp. 151–180, 1981. 8, 33

[69] B. Sakitt and H. Barlow, "A Model for the Economical Encoding of the Visual Image in Cerebral Cortex," *Biological Cybernetics*, vol. 43, no. 2, pp. 97–108, 1982. 8, 12, 20

[70] R. Young, *The Gaussian Derivative Theory of Spatial Vision: Analysis of Cortical Cell Receptive Field Line-weighting Profiles*. Research publication, General Motors Research Laboratories, 1985. 8, 79

[71] R. Young, "Gaussian derivative model of spatial vision: I. retinal mechanisms," *Spatial Vision*, vol. 2, pp. 273–293, 01 1987. 8

[72] Gary Heiting, "The Retina: Where Vision Begins." `https://inside-the-brain.com/tag/peripheral-vision/`, Jan. 2019. Accessed: 2020-01-10. 9

[73] M. Douma, "Retinal Ganglion Cells Calculate Color." `http://www.webexhibits.org/colorart/ganglion.html`, Jan. 2019. Accesed: 2020-01-10. 9

[74] M. Abramowitz, "Handbook of mathematical functions, with formulas, graphs, and mathematical tables,," *Dover Publications*, 1974. 12, 20

[75] W. T. Freeman and E. H. Adelson, "The Design and Use of Steerable Filters," *IEEE Transactions on Pattern Analysis and Machine Intelligence*, vol. 13, pp. 891–906, 1991. 16, 21

[76] A. M. Van Dijk and J. Martens, "Image representation and compression with steered Hermite transforms," *Signal Processing*, vol. 56, no. 1, pp. 1–16, 1997. 16, 21

[77] F. Brackx, N. De Schepper, and F. Sommen, "The higher dimensional hermite transform: a new approach," *Complex variables*, vol. 48, no. 3, pp. 189–210, 2003. 17

[78] J. J. Gibson, "The perception of the visual world," *Houghton Mifflin*, 1950. 25

[79] N. Takashi, "Ale finite element computations of fluid-structure interaction problems," *Computer Methods in Applied Mechanics and Engineering*, vol. 112, no. 1, pp. 291 – 308, 1994. 26

[80] R. B. Milan Sonka, Vaclav Hlavac, *Image Processing, Analysis and Machine Vision*. Springer, Boston, MA, 1993. 26, 27

[81] F. Raudies, "Optic flow," *Scholarpedia*, vol. 8, no. 7, p. 30724, 2013. revision #149632. 31

[82] C. Mota, I. Stuke, and E. Barth, "Analytical solutions for multiple motions," in *Proceedings of the International Conference on Image Processing ICIP*, 2001. 33

[83] A. A. Stocker and E. P. Simoncelli, "Noise characteristics and prior expectations in human visual speed perception," *Nature neuroscience*, vol. 9, no. 4, p. 578, 2006. 33

[84] H. Gafni and Y. Zeevi, "A model for processing of movement in the visual system," *Biological Cybernetics*, vol. 32, no. 3, pp. 165–173, 1979. 34

[85] D. Gabor, "Theory of communication. part 1: The analysis of information," *Journal of the Institution of Electrical Engineers-Part III: Radio and Communication Engineering*, vol. 93, no. 26, pp. 429–441, 1946. 34

[86] J. Weickert and C. Schnörr, "A theoretical framework for convex regularizers in pde-based computation of image motion," *International Journal of Computer Vision*, vol. 45, no. 3, pp. 245–264, 2001. 35, 36

[87] A. Bruhn, J. Weickert, T. Kohlberger, and C. Schnörr, "A multigrid platform for real-time motion computation with discontinuity-preserving variational methods," *International Journal of Computer Vision*, vol. 70, no. 3, pp. 257–277, 2006. 35, 36

[88] L. M. Álvarez León, J. Esclarín Monreal, M. Lefébure, and J. Sánchez, "A pde model for computing the optical flow," 1999. 35

[89] I. Cohen, "Nonlinear variational method for optical flow computation," in *Proceedings of the Scandinavian conference on image analysis*, vol. 1, pp. 523–523, Citeseer, 1993. 36

[90] R. Deriche, P. Kornprobst, and G. Aubert, "Optical-flow estimation while preserving its discontinuities: A variational approach," in *Asian Conference on Computer Vision*, pp. 69–80, Springer, 1995. 36

[91] A. Kumar, A. R. Tannenbaum, and G. J. Balas, "Optical flow: a curve evolution approach," *IEEE Transactions on image processing*, vol. 5, no. 4, pp. 598–610, 1996. 36

[92] C. Zach, T. Pock, and H. Bischof, "A duality based approach for realtime tv-l 1 optical flow," in *Joint pattern recognition symposium*, pp. 214–223, Springer, 2007. 36

[93] Barron and Thacker, "Computing 2d and 3d optical flow," *Features and Measurement Series*, 2005. 40

[94] X. Wu, G. Ding, and V. Taylor, "Parallel optical flow processing of 4d cardiac ct data on multicore clusters," in *2014 IEEE 17th International Conference on Computational Science and Engineering*, pp. 113–120, IEEE, 2014. 45

[95] S. Baker, D. Scharstein, J. P. Lewis, S. Roth, M. J. Black, and R. Szeliski, "A database and evaluation methodology for optical flow," *International Journal of Computer Vision*, vol. 92, pp. 1–31, Mar. 2011. 46, 47

[96] T. Mathworks, "Computer vision system toolbox," *URL https://mathworks.com/products/computer-vision*, 2018. 47, 48, 49, 50

[97] M. Otte and H. H. Nagel, *Optical flow estimation: Advances and comparisons*, pp. 49–60. Berlin, Heidelberg: Springer Berlin Heidelberg, 1994. 47, 48, 55

[98] R. Szeliski, "Prediction error as a quality metric for motion and stereo," in *Proceedings of the Seventh IEEE International Conference on Computer Vision*, vol. 2, pp. 781–788 vol.2, Sep. 1999. 49

[99] J. Bigun, G. H. Granlund, and J. Wiklund, "Multidimensional orientation estimation with applications to texture analysis and optical flow," *IEEE Transactions on Pattern Analysis & Machine Intelligence*, no. 8, pp. 775–790, 1991. 62

[100] M. Zöckler, D. Stalling, and H.-C. Hege, "Interactive visualization of 3d-vector fields using illuminated stream lines," in *Proceedings of the 7th Conference on Visualization '96*, VIS '96, (Los Alamitos, CA, USA), pp. 107–ff., IEEE Computer Society Press, 1996. 63

[101] M. J. Koren, R. B. Devereux, P. N. Casale, D. D. Savage, and J. H. Laragh, "Relation of left ventricular mass and geometry to morbidity and mortality in uncomplicated essential hypertension," *Annals of internal medicine*, vol. 114, no. 5, pp. 345–352, 1991. 69

[102] I. G. McDonald, "The shape and movements of the human left ventricle during systole: a study by cineangiography and by cineradiography of epicardial markers," *The American journal of cardiology*, vol. 26, no. 3, pp. 221–230, 1970. 69

[103] C. W. Chen and T. S. Huang, "Epicardial motion and deformation estimation from coronary artery bifurcation points," in *[1990] Proceedings Third International Conference on Computer Vision*, pp. 456–459, IEEE, 1990. 69

[104] S. Osher and J. A. Sethian, "Fronts propagating with curvature-dependent speed: Algorithms based on hamilton-jacobi formulations," *Journal of Computational Physics*, vol. 79, no. 1, pp. 12 – 49, 1988. 69

[105] CIBC, 2016. Seg3D: Volumetric Image Segmentation and Visualization. Scientific Computing and Imaging Institute (SCI), Download from: http://www.seg3d.org. 69

[106] J. Ahrens, B. Geveci, and C. Law, "Paraview: An end-user tool for large data visualization," *The visualization handbook*, vol. 717, 2005. 76, 89

[107] U. Ayachit, *The paraview guide: a parallel visualization application*. Kitware, Inc., 2015. 76, 89

[108] S. M. Song and R. M. Leahy, "Computation of 3-d velocity fields from 3-d cine ct images of a human heart," *IEEE transactions on medical imaging*, vol. 10, no. 3, pp. 295–306, 1991. 77

[109] K. G. Chan and M. Liebling, "Estimation of divergence-free 3d cardiac blood flow in a zebrafish larva using multi-view microscopy," in *2015 IEEE 12th International Symposium on Biomedical Imaging (ISBI)*, pp. 385–388, IEEE, 2015. 77

[110] M. Gutierrez, L. Moura, C. Melo, and N. Alens, "Computing optical flow in cardiac images for 3d motion analysis," in *Proceedings of Computers in Cardiology Conference*, pp. 37–40, IEEE, 1993. 77

[111] J. Condell and L. Barron, "3d optical flow methods in cardiac imaging," in *Irish machine vision and image processing conference*, vol. 30, p. 227, 2005. 77

[112] B. Escalante-Ramírez and J. L. Silván-Cárdenas, "Advanced modeling of visual information processing: A multiresolution directional-oriented image transform based on Gaussian derivatives," *Signal Processing: Image Communication*, vol. 20, no. 9-10, pp. 801–812, 2005. 79

[113] J. L. Silván-Cárdenas and B. Escalante-Ramírez, "The multiscale hermite transform for local orientation analysis," *IEEE Transactions on Image Processing*, vol. 15, no. 5, pp. 1236–1253, 2006. 79

[114] A. J. Bravo, F. Roa, M. Vera, J. Contreras-Velásquez, Y. Huérfano, J. Chacón, S. Wilches-Durán, M. Graterol-Rivas, D. Riaño-Wilches, J. Roja, *et al.*, "Tomografía computarizada por rayos x en cardiología," *Revista Latinoamericana de Hipertensión*, vol. 12, no. 2, pp. 49–61, 2017. 81, 87

[115] D. P. Boyd and M. J. Lipton, "Cardiac computed tomography," *Proceedings of the IEEE*, vol. 71, no. 3, pp. 298–307, 1983. 81

[116] J. V. Hajnal and D. L. Hill, *Medical image registration*. CRC press, 2001. 82

[117] M. J. Budoff, D. Georgiou, A. Brody, A. S. Agatston, J. Kennedy, C. Wolfkiel, W. Stanford, P. Shields, R. J. Lewis, W. R. Janowitz, *et al.*, "Ultrafast computed tomography as a diagnostic modality in the detection of coronary artery disease: a multicenter study," *Circulation*, vol. 93, no. 5, pp. 898–904, 1996. 82

[118] R. Robb and R. Morin, "Principles and instrumentation for dynamic x-ray computed tomography," in *Cardiac Imaging. A companion to Braunwald's Heart Disease*, pp. 634–668, WB Saunders Company, Philadelphia, 1991. 82

[119] H. Cynthia *et al.*, "Recent progress in electron beam tomography," *Medical Imaging Technology*, vol. 11, no. 5, p. 578, 1993. 82

[120] W. Moshage, S. Achenbach, B. Seese, K. Bachmann, and M. Kirchgeorg, "Coronary artery stenoses: three-dimensional imaging with electrocardiographically triggered, contrast agent-enhanced, electron-beam ct.," *Radiology*, vol. 196, no. 3, pp. 707–714, 1995. 83

[121] Y. Arad, L. A. Spadaro, K. Goodman, A. Lledo-Perez, S. Sherman, G. Lerner, and A. D. Guerci, "Predictive value of electron beam computed tomography of the coronary arteries: 19-month follow-up of 1173 asymptomatic subjects," *Circulation*, vol. 93, no. 11, pp. 1951–1953, 1996. 83

[122] "Helical CT scanners market forecast to 2023 explored in latest research." https://www.openpr.com/news/964032/helical-ct-scanners-market-forecast-to-2023-explored-in-latest-research.html. Accessed: 2020-01-24. 84

[123] W. A. Kalender, W. Seissler, E. Klotz, and P. Vock, "Spiral volumetric ct with single-breath-hold technique, continuous transport, and continuous scanner rotation.," *Radiology*, vol. 176, no. 1, pp. 181–183, 1990. 84

[124] C. R. Becker, T. F. Jakobs, S. Aydemir, A. Becker, A. Knez, U. J. Schoepf, R. Bruening, R. Haberl, and M. F. Reiser, "Helical and single-slice conventional ct versus electron beam ct for the quantification of coronary artery calcification," *American Journal of Roentgenology*, vol. 174, no. 2, pp. 543–547, 2000. 84

[125] G. Wang, C. R. Crawford, and W. A. Kalender, "Guest editorial-multirow detector and cone-beam spiral/helical ct," *IEEE Transactions on Medical Imaging*, vol. 19, no. 9, pp. 817–821, 2000. 84

[126] R. Carlton and A. Adler, "Principles of radiographic imaging: An art and a science philadelphia," *PA: Delmar Cengage Learning*, 2013. 84

[127] O. Ecabert, J. Peters, H. Schramm, C. Lorenz, J. von Berg, M. J. Walker, M. Vembar, M. E. Olszewski, K. Subramanyan, G. Lavi, *et al.*, "Automatic model-based segmen-

tation of the heart in ct images," *IEEE transactions on medical imaging*, vol. 27, no. 9, pp. 1189–1201, 2008. 85

[128] R. A. Brooks and G. Di Chiro, "Theory of image reconstruction in computed tomography," *Radiology*, vol. 117, no. 3, pp. 561–572, 1975. 85

[129] J. Gore and J. Orr, "Image formation by back-projection: A reappraisal," *Physics in Medicine & Biology*, vol. 24, no. 4, p. 793, 1979. 85

[130] R. Gordon, R. Bender, and G. T. Herman, "Algebraic reconstruction techniques (art) for three-dimensional electron microscopy and x-ray photography," *Journal of theoretical Biology*, vol. 29, no. 3, pp. 471–481, 1970. 85

[131] M. Jiang and G. Wang, "Convergence studies on iterative algorithms for image reconstruction," *IEEE Transactions on Medical Imaging*, vol. 22, no. 5, pp. 569–579, 2003. 85

[132] V. Chougule, A. Mulay, and B. Ahuja, "Clinical case study: Spine modeling for minimum invasive spine surgeries (miss) using rapid prototyping," 02 2018. 86

[133] C. Morgan, "Physics of radiology," 1983. 86

[134] A. Wolbarst, "Basic principles of computed tomography," *St. Norwalk: Appleton & Lange*, 1993. 86

[135] "Paraview, large data visualization." https://www.paraview.org/overview/. Accessed: 2020-01-25. 89